Contribution to the state of charge estimation and the optimised management of a Li-ion battery : application for the electric vehicles

Gelareh Javid

▶ To cite this version:

Gelareh Javid. Contribution to the state of charge estimation and the optimised management of a Li-ion battery : application for the electric vehicles. Eco-conception. Université de Haute Alsace - Mulhouse, 2021. English. NNT : 2021MULH3784 . tel-03789642

HAL Id: tel-03789642
https://theses.hal.science/tel-03789642

Submitted on 27 Sep 2022

Année 2021 N° d'ordre :

UNIVERSITÉ DE HAUTE-ALSACE
UNIVERSITÉ DE STRASBOURG

THESE

Présentée pour l'obtention du grade de

Docteur de l'Université de Haute-Alsace

ECOLE DOCTORALE : Mathématiques, sciences de l'information et de l'ingénieur (ED 269)

Discipline : Électronique, Électrotechnique et Automatique

Présentée et soutenue publiquement
par

Gelareh JAVID

le 10/11/2021

Contribution à l'estimation de charge et à la gestion optimisée d'une batterie Lithium-ion : Application au véhicule électrique

---

Sous la direction du MCF HDR Djaffar Ould Abdeslam et de Prof. Michel Basset

Jury :

Prof. DUMUR Didier, CentraleSupélec	**Rapporteur**
Prof. SCHMIDT Michael, Hochschule Offenburg (HSO)	**Rapporteur**
Prof. KRATZ Frédéric, INSA Centre Val de Loire	**Examinateur**
Prof. IDOUMGHAR Lhassane, Université de Haute-Alsace	**Examinateur**
Prof. BASSET Michel, Université de Haute-Alsace	**Co-Directeur de thèse**
MCF HDR OULD ABDESLAM Djaffar, Université de Haute-Alsace	**Directeur de thèse**

Acknowledgment

First and foremost I would like to express my sincere gratitude to my supervisors, Djaffar Ould Abdeslam and Michel Basset for their advice and encouragement during my Ph.D. I am grateful for their patience, motivation, and understanding even in non-scientific aspects of doing research.

I would like to extend my sincere thanks to Prof. Olivier HAEBERLE, and Dr. Jonathan Ledy for their knowledge and expertise that was kindly shared with me.

I'm grateful to the members of MIAM and IMTI groups for the friendly and positive environment they offered to me. It was a pleasure to work with them all.

Thanks should also go to jury members for their helpful advice and suggestions.

I'm extremely grateful to Kowsar for her always helpful advice, help in editing, and her continuous motivation during writing time and forever after.

I would like to express my deepest appreciation to my uncle and my aunt Hamid Aleboyeh and Azam Aleboyeh. I could not have undertaken this journey without their support, and guidance.

Many thanks to Ghazaleh, Hamid, and Tara for sending their loves and kindness from far away.

Last but not least, heartfelt thanks go to my parents, Mohammad and Hoory, for their endless love, and infinite encouragement. Their unconditional belief in me has kept my spirits and motivation high, during all ups and downs of my life.

Abstract

The State Of Charge (SOC) estimation is a significant issue for safe performance and the lifespan of Lithium-ion (Li-ion) batteries which is used to power the Electric Vehicles (EVs).

In this thesis, the accuracy of SOC estimation is investigated using Deep Recurrent Neural Network (DRNN) algorithms. To do this, for a one cell Li-ion battery, three new SOC estimator based on different DRNN algorithms are proposed: a Bidirectional LSTM (BiLSTM) method, a Robust Long-Short Term Memory (RoLSTM) algorithm, and a Gated Recurrent Units (GRUs) technique. Using these, one is not dependent on precise battery models and can avoid complicated mathematical methods especially in a battery pack. In addition, these models are able to precisely estimate the SOC at varying temperature. Also, unlike the traditional recursive neural network where content is re-written at each time, these networks can decide on preserving the current memory through the proposed gateways. In such case, it can easily transfer the information over long paths to receive and maintain long-term dependencies.

Comparing the results indicates the BiLSTM network has a better performance than the other two. Moreover, the BiLSTM model can work with longer sequences from two direction, the past and the future, without gradient vanishing problem. This feature helps to select a sequence length as much as a discharge period in one drive cycle, and to have more accuracy in the estimation. Also, this model well behaved against the incorrect initial value of SOC.

Finally, a new BiLSTM method introduced to estimate the SOC of a pack of batteries in an Ev. IPG Carmaker software was used to collect data and test the model in the simulation. The results showed that the suggested algorithm can provide a good SOC estimation without using any filter in the Battery Management System (BMS).

Résumé

L'estimation de l'état de charge (SOC) est un point crucial pour la sécurité des performances et la durée de vie des batteries lithium-ion (Li-ion) utilisées pour alimenter les VE. Dans cette thèse, la précision de l'estimation de l'état de charge est étudiée à l'aide d'algorithmes de réseaux neuronaux récurrents profonds (DRNN). Pour ce faire, pour une cellule d'une batterie Li-ion, trois nouvelles méthodes sont proposées : une mémoire bidirectionnelle à long et court terme (BiLSTM), une mémoire robuste à long et court terme (RoLSTM) et une technique d'unités récurrentes à grille (GRU). En utilisant ces techniques, on ne dépend pas de modèles précis de la batterie et on peut éviter les méthodes mathématiques complexes, en particulier dans un bloc de batterie. En outre, ces modèles sont capables d'estimer précisément le SOC à des températures variables. En outre, contrairement au réseau de neurones récursif traditionnel dont le contenu est réécrit à chaque fois, ces réseaux peuvent décider de préserver la mémoire actuelle grâce aux passerelles proposées. Dans ce cas, il peut facilement transférer l'information sur de longs chemins pour recevoir et maintenir des dépendances à long terme. La comparaison des résultats indique que le réseau BiLSTM a de meilleures performances que les deux autres méthodes. De plus, le modèle BiLSTM peut travailler avec des séquences plus longues provenant de deux directions, le passé et le futur, sans problème de disparition du gradient. Cette caractéristique permet de sélectionner une longueur de séquence équivalente à une période de décharge dans un cycle de conduite, et d'obtenir une plus grande précision dans l'estimation. En outre, ce modèle s'est bien comporté face à une valeur initiale incorrecte du SOC. Enfin, une nouvelle méthode BiLSTM a été introduite pour estimer le SOC d'un pack de batteries dans un EV. Le logiciel IPG Carmaker a été utilisé pour collecter les données et tester le modèle en simulation. Les résultats ont montré que l'algorithme proposé peut fournir une bonne estimation du SOC sans utilisation de filtre dans le système de gestion de la batterie (BMS).

CONTENTS

LIST OF TABLES

LIST OF FIGURES

ABBREVIATIONS

Adam Adaptive Moment Estimation.

AEKF Adaptive Extended Kalman Filter.

AI Artificial Intelligent.

Artemis Assessment and Reliability of Transport Emission Models and Inventory Systems.

BiLSTM Bidirectional LSTM.

BMS Battery Management System.

BPNN Back-Propagation Neural Network.

CADC Common Artemis Driving Cycles.

CC Coulomb Counting estimation.

CO Carbon monoxide.

DNN Deep Neural Network.

DRNN Deep Recurrent Neural Network.

ECM Electrical Circuit Model.

EECM Electrical Equivalent Circuit Models.

EIS Electrochemical Impedance Spectroscopy.

EKF Extended Kalman Filter.

EVs Electric Vehicles.

FL Fuzzy Logic.

FTP Federal Test Procedure.

GPU graphics processing unit.

GRUs Gated Recurrent Units.

H∞ H-infinity.

HWFET Highway Fuel Economy Test.

KF Kalman Filter.

LA92 Los Angeles 92.

Li-ion Lithium-ion.

LSTM Long-Short Term Memory.

MAE Mean Absolute Error.

MAX Maximum Error.

ML Machine Learning.

MLP Multi Layer Perceptron.

MSE Mean Square Error.

NNs Neural Networks.

OCV Open Circuit Voltage.

PV PhotoVoltaic.

RLS Recursive Least Square.

RMSE Root Mean Square Error.

RNNs Recurrent Neural Networks.

RoAdam Robust Adam.

RoLSTM Robust Long-Short Term Memory.

SOA Safe Operating Area.

SOC State Of Charge.

SOF State of Function.

SOH State Of Health.

SVM Support Vector Machine.

UDDS Urban Dynamometer Driving Schedule.

UKF UnscentedKalmanFilter.

US06 Supplemental Federal Test Procedure Driving Schedule.

V2G Vehicle to Grid.

WHO World Health Organization.

1

INTRODUCTION

Contents

1.1 motivation

For over 100 years, automobiles have been used for transportation of humans, and in this way, reformed traveling around the world. Exploring of rural areas and going on a road trip across the country were made possible using wheels. However, the engine vehicles cause many environmental damages as well [7]. According to the World Health Organization (WHO), in 2000, fuel vehicles produce 34% of nitrogen dioxide discharged into the environment. They, additionally, are responsible for 51% of the carbon monoxide, 10% of the particulate, and 33% of the carbon dioxide, in the United States only [8]. Reacting with humidity in the air, nitrogen dioxide makes nitric acid, which causes severe corrosion. It also leads to thick fog and drastically reduces field of view. This molecule has a greenhouse effect and a critical negative footprint on plant growth. Carbon monoxide (CO) is a harmful gas that provokes migraines, dizziness, and respiratory disease. High enough CO levels may induce unconsciousness or death. Lastly, carbon dioxide is a major contributor to worldwide temperature rise. As a result, nowadays, using Electric Vehicles (EVs) as an alternative to diesel- and petrol-powered cars is highly regarded. Subsequently, a high-tech battery is a crucial element for EVs.

Various types of batteries such as nickel-cadmium, lithium, and acid, are used as the dominant power source in EVs [9]. Among them, Lithium-ion (Li-ion) batteries are the most popular due to their specific characteristics, e.g., high energy density, self-discharge, charging speed, low maintenance, and long-life cycle. The correct charging of Li-ion batteries improves their performance and extends their lifespan and it is only possible by using the Battery Management System (BMS), which controls the discharging [10]. To provide an accurate measurement of the residual driving range of the vehicle, as well as the correct battery balance, a trustworthy status estimate is necessary. State Of Charge (SOC) is the remaining battery load and defines the ratio of the battery's remaining capacity to its nominal battery capacity [11]. The battery might be exposed to very dynamic load demands due to the unexpected driving behavior and frequent acceleration and deceleration of a car. Because of these charging demands, SOC estimation is a difficult task. SOC is not a visible factor, thus its precise estimate is crucial to dependable and safe vehicle operation [12].

1.2 SOC estimation as a central measure

To date, various methods have been developed and introduced to SOC estimation, which are separated into two main categories of direct and indirect methods [13, 14]. In the case of direct techniques, the battery's physical characteristics such as current, voltage and battery temperature are utilized to evaluate SOC. A popular direct method is Coulomb Counting estimation (CC) described in detail by Lashway *et al.* [15]. Many published studies also contributed in the development of the Open Circuit Voltage (OCV) method for the SOC estimation (e.g., [7, 16]). Electrochemical Impedance Spectroscopy (EIS) is another direct method to evaluate SOC [17]. Indirect methods, on the other hand, do not use a specific equation, rather they employ a model for the battery or mapping of system specification. One of the model-based methods is Electrical Circuit Model (ECM) [18]. Another type of indirect methods are the adaptive-filter based algorithms such as Kalman Filter (KF, EKF, UKF, and AEKF) [19, 20, 21], Recursive Least Square (RLS), and the H-infinity ($H\infty$) algorithm [14, 22, 23].All these approaches, generally need complex models to accurately identify the non-linear behavior of a battery and involve numerous differential equations that may be complicated. They also frequently need several parameters for a satisfying SOC estimate in different environments. As a result, in recent years, Artificial Intelligent (AI) and data-driven approaches as a category of indirect methods have been utilized for SOC estimation, including Fuzzy Logic (FL) [24, 25, 26], Neural Networks (NNs) [27, 28, 29, 30, 31], and Support Vector Machine (SVM) [32, 33]. Nevertheless, these techniques also have weaknesses, as the variety of and complexity of Li-ion batteries restricts their estimation efficacy. For instance, training is based on manually created characteristics that requires a lot of human work and skill. In addition, their architectures do not have adequate analytical skills to handle high-dimensional measurement data that are used. Deep learning algorithms, as a crucial area of AI, offer an excellent approach to these issues.

Deep learning (also known as deep structured learning or dynastic learning) is a class of Machine Learning (ML) for extracting a higher level of features, and is based on work-specific algorithms. Figure 1.1 is a Venn diagram representing the area of AI, Machine Learning as a subset of AI, and deep learning as a sub-field of ML.

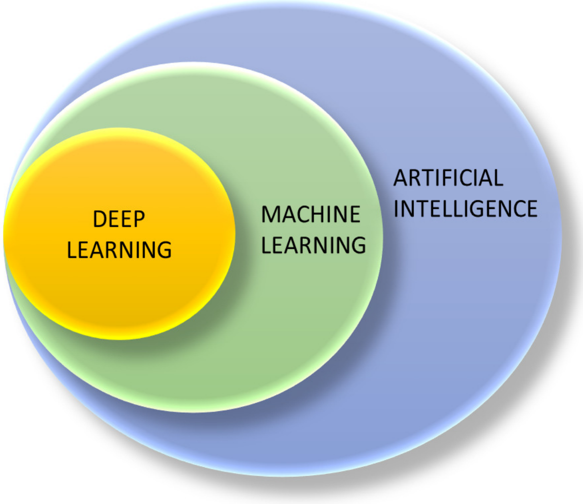

Figure 1.1: Venn diagram clarifying the relationship between Artificial Intelligent, Machine learning, and Deep learning.

Most modern deep learning models are based on artificial neural networks. However, they may include predicate or hidden variables in generating models such as nodes in deep belief networks and deep Boltzmann machines [34, 35]. Nonlinear transformations and multi-layer deep neural networks allow for extracting hierarchical representations from input data. One Deep Neural Network (DNN) layer has the ability to learn new representations of input by itself. As well as, the network's stacking structure is able to extract complex feature information by combining simple input. A few recent DNN-based techniques that use data to determine battery SOC have emerged during the past three years [36, 37]. Chemali *et al.* [38] developed a Multi Layer Perceptron (MLP) network using battery data at different temperatures and generate the first deep learning SOC estimator. In [39] they utilized Long-Short Term Memory (LSTM), since it improves temporal information in time series capture, and found more accuracy in their calculated SOC. The low-complexity estimating model that relies on Gated Recurrent Units (GRUs) proposed in [40, 41]. Since deep learning-based state estimation for batteries is still quite new, the accuracy and model structure of these estimators still need to be improved.

1.3 Objectives and Thesis Structure

The ability to estimate the SOC of Li-ion batteries in real time, which is one of the most essential performance features of a battery, becomes more important with the increasing usage of battery-driven electric vehicles. This research study is focused on the implementation of SOC estimation by means of deep learning methods with the goal of reducing computing complexity while simultaneously increasing accuracy. As such, three new structure for SOC evaluation of one cell of Li-ion are investigated. Following that, the BiLSTM method is presented as the best algorithm for the SOC estimate in a battery-pack that includes both series and parallel wiring of batteries.

In Chapter 2, a short history of EVs and rechargeable batteries is provided. In addition, the specific of the enhanced lithium-based batteries, the existing methods for modeling them, and important definitions related to the Battery Management System are addressed.

Chapter 3 proposes a review on SOC estimation techniques. This chapter discusses the benefits and drawbacks of the methods that have been used before.

Details of three proposed SOC estimation methods, typically BiLSTM, Robust Long-Short Term Memory (RoLSTM) and GRUs, are explained in chapter 4. First estimator is based on BiLSTM algorithm, which is a novel technique for estimating SOC sequences through the bidirectional and sequential Li-ion input data. The improved estimate accuracy of this design will be achieved through learned bidirectional relationships. In RoLSTM method as the second estimator, instead of one LSTM network, three of them are used in parallel for each input, and consequently, the number of LSTM units will be reduced. Also, to optimize the LSTM network, a robust and adaptive online optimization method is used. This optimization is an improvement of Adam method which is called Robust Adam (RoAdam)[42]. RoAdam can be adaptively tuned against a doubtful outlier. The weights and biases could be adapted online with a strategy of adaptive optimization to have a high-performance network. The last estimator presented here is based on Gated Recurrent Units (GRUs) approaches. These networks are an improved version of standard RNNs introduced to overcome the vanishing gradient problem. GRUs are using two gate unites to decide between beneficial and not functioning data.

Chapter 5 shows the results of these three methods implemented for one cell Li-ion battery. Moreover, this chapter discusses the effects of the number of layers and units of DRNN on the accuracy of the SOC estimation. The Panasonic 18650PF Li-ion databases produced by McMaster's University in Ontario are employed to evaluate these techniques. Additionally, Tensorflow, an open-source deep learning framework written in Python, and the Strasbourg University Computing Center's server are applied for the development and the learning step of the algorithms.

Chapter 6 focuses on SOC estimation of a battery pack mounted on EVs. Employing BiLSTM technique to evaluate SOC for EVs battery-pack in the real-time simulation is investigated. Using the IPG CarMaker environment,vehicle models have been created to model various EVs architectures, including battery parameters, transmission, electric motors, vehicle aerodynamics, and most significantly, driver characteristics.

Last, a concluding remark is given in chapter 7, along with possible future directions of this project.

1.4 List of Publications

As a consequence of this Ph.D. project, the relevant academic papers have been published:

1. Gelareh Javid, Djaffar Ould Abdeslam, Michel Basset. "Adaptive Online State Of Charge Estimation of EVs Lithium-ion Batteries with Deep Recurrent Neural Networks", Energies 2021, 14(3), 758.

2. Gelareh Javid, Michel Basset, Djaffar Ould Abdeslam. "Adaptive Online Gated Recurrent Unit for Lithium-Ion Battery SOC Estimation", 46th Annual Conference of the IEEE Industrial Electronics Society (IES) (IECON2020), Singapore.

3. Gelareh Javid, Djaffar Ould Abdeslam, Dirk Benyoucef. "Maximum Power Point Tracking of PhotoVoltaic Power System with Adaptive Fuzzy Terminal Sliding Mode Controller", IEEE 18th International Conference on Environment and Electrical Engineering and 2nd Industrial and Commercial Power Systems Europe (EEEIC2018), Palermo, Italy.

2

CHARGING CHALLENGES FOR ELECTRIC VEHICLES: BASIC DEFINITIONS

Contents

2.1 Introduction

This Chapter provides a brief overview of the history of EVs and rechargeable batteries. There is also a discussion on the details of the lithium-based battery, a review of the battery modeling method, and key terminologies linked to the battery management system.

2.2 Development of Electric Vehicles

The electric vehicle's history started in the middle of the nineteenth century. However, compared to the combustion-engine cars that eventually reached the market, these vehicles were more costly, slower, and had a shorter range, which led to a drop in their use globally. Since the early 20th century, interest in electric automobiles and alternative fuels has been stoked by worries about the escalating problems with hydrocarbon pollutants and vehicle fuels, such as environmental impact and hydrocarbon flow stability.

In 1867, the Austrian inventor Franz Kravgol demonstrated the first electric two-wheeled bikes at the Paris World's Fair. Nonetheless, this effort was just for entertainment purposes and was not appropriate for street driving. Gustave Trouve, a French inventor, exhibited another cycle, this time a tricycle, at the International Electric Exhibition in Paris in November 1881[43].

In London in 1884, Thomas Parker developed the first electric car. Parker's interest in low-emission cars, as well as his concern about the harmful effects of smoking and pollution in London at the time, pushed him to create electric autos. He used high-capacity, rechargeable batteries designed specifically for this vehicle. He was also involved with the electrification of the London Underground, trams in Liverpool and Birmingham, and the Coalite smokeless fuel. [1].

The first American electric car was developed between 1890 and 1891 by William Morrison. The vehicle had a six-seater wagon and reached a speed of 14 miles per hour (23 kilometers per hour) [44].

Motor vehicle enthusiasm grew in the late 1890s and early 1900s. Electric taxis gained

Figure 2.1: The first practical electric car may have been built by the English inventor Thomas Parker in 1884 [1]

popularity in the late 1800s. These taxis were popularized by Walter C. Bersey, and in 1897, electric taxis joined the taxi fleet and the streets of London. As a result, these taxis began to be known as "humming birds" after a time. The electric carriage was utilized as a cab by Samuel's Electric Carriage and Wagon Company in New York City the same year. By 1898, when it was converted into an electric vehicle business by investors, it had manufactured 62 taxis [45].

Several companies, including Henny Coachworks, National Electrical Union Company, and Exide Battery manufacturers, collaborated on the development of an all-electric vehicle in the 1950s. The car's voltage was set between 36 and 72 volts. Powered by 72-volt batteries, the 72-volt variant could reach speeds of up to 96 km / h (60 mph) and travel for up to an hour on a single charge.

Although the popularity of electric cars declined in the 1900s as a result of the widespread availability of low-cost gasoline for transportation and the improved performance of gasoline vehicles, the demand for EVs has increased dramatically in the past few decades. As reported by the International Energy Agency (IEA), yearly EV sales have increased from 1.67 thousand in 2005 to 2.1 million in 2019, and as a result, the worldwide stock of electric vehicles has reached 7.2 million. Figure 2.2 depicts the Histogram of the Electric Vehicles Stock of Passenger Automobiles from the years 2013 to 2019 for the major geographic areas [46]. It is anticipated that the demand for electric cars will grow in the future years. According to the Sustainable Development Scenario, the global electric vehicle stock is expected to increase by 36 percent each year. In the next 10 years, the quantity of EV in stock will have increased by a factor of more than 30. Figure 2.3 illustrates the worldwide electric vehicle fleet through 2030 [47].

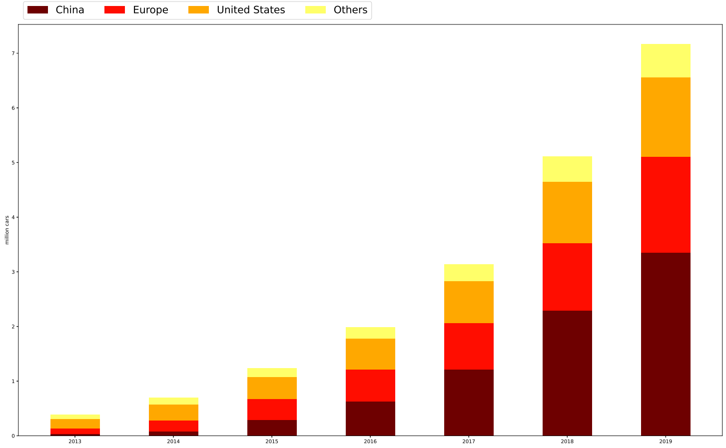

Figure 2.2: Electric car stock by region, 2013-2019

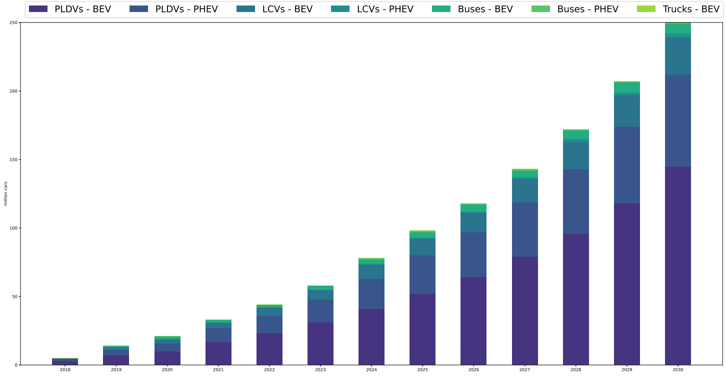

Figure 2.3: Global Electric Vehicle stock by Sustainable Development Scenario , 2018-2030

2.3 A review on rechargeable batteries for Electric Vehicles

Alessandro Volta was the first to define the concept of a voltage cell, often known as a battery, in 1800. Voltage cells are devices that produce electrical energy via chemical processes. Volta's battery is made up of disks of zinc and copper that alternate with each other. The copper cathode performs the reduction process, whereas the zinc anode does the oxidation. Furthermore, to complete the circuit, a salt bridge, which is constructed from a layer of cloth that has been wetted with brine, is placed between the cathode and the anode. In addition, an external circuit is utilized to direct the flow of electrons through the system. The areas where reduction and oxidation occur are called half-cells [48]. There were two major issues with this battery: First and foremost, the high number of disks causes brine to be drawn out of the fabric, resulting in a reduction in current output. The second issue with the Volta cell was that it had a limited lifetime owing to the fast corrosion of metal in the presence of saltwater, which caused it to malfunction [49].

To prevent hydrogen from collecting on a copper cathode, John Frederic Daniell invented a secondary electrolyte that interacted chemically with the hydrogen. He published his findings in 1836. Daniel's dual electrolyte battery, commonly known as Daniel's cell, is a kind of rechargeable battery [50].

Gaston Planté, in 1859, created the first rechargeable lead-acid battery by immersing two sheets of lead in a sulfuric acid solution. When the lead anode reacts with the acid, electrons are liberated, while the lead cathode absorbs the electrons, resulting in the production of a current. By reversing the current flow, it is possible to recharge the battery [51].

As early as 1881, Camille Alphonse Faure made significant improvements to the Planté's design performance by creating a new sheet that contained lead oxide batter squeezed into a lead grid lattice [52]. Until the late 1800s, the electrolyte in batteries was liquid. This made transporting batteries extremely risky, and as a result, most batteries were not designed to be transported after being attached to a circuit. Inventor Georges Leclanche created a battery in 1866 that included three components: a manganese dioxide cathode, a zinc anode, and an ammonium chloride solution electrolyte. Despite the fact that the electrolyte in the Leclanche cell was liquid, the chemical composition of the battery was an important step in the development of the dry battery. Further down the road in 1887, Carl Gessner discovered how to make an electrolyte by gluing together ammonium chloride and Paris plaster. By the late 1950s, these new dry batteries had become very popular [49]. These novel dry batteries were also referred to as carbon batteries since carbon serves an important role as an electrical conductor in them, despite the fact that it is not employed in chemical processes.

Waldemar Jungner was the developer of the nickel-cadmium (NiCd) battery, which was first used in the early 1900s. The negative electrode (anode) of this battery is made of cadmium (Cd), and the positive electrode (cathode) is built of nickel (Ni) (cathode). In 1901, iron was replaced by cadmium in a nickel-cadmium battery by Thomas Edison, and it was renamed Ni-Fe (NiFe) [53]. Low specific energy and rapid self-ignition are among the disadvantages of nickel-iron batteries. They also have poor performance at low temperatures.

In the 1950s, Lewis Urry, Paul Marshall, and Karl Kordesch of Union Carbide replaced the ammonium chloride electrolyte with an alkali material known as alkaline. Since the 1960s, alkaline batteries have been increasingly popular, particularly as a replacement for carbon-zinc batteries. Alkaline solar batteries have a longer service life and are capable of storing far more energy than carbon batteries [54]. Comsat invented the nickel-hydrogen battery in the 1970 for use in communications satellites, which was later adopted by other companies. Nickel-hydrogen batteries can store hydrogen gas in pressured gas molds, which are a type of pressure vessel. A large number of spacecraft and space stations are powered by nickel-hydrogen batteries. In the late 1980s, nickel-metal hydride (NiMH) batteries were created by researchers at many businesses and brought onto the market. NiMH batteries were smaller in size and less expensive than nickel-hydrogen batteries at the time of their introduction [55].

Sony was the first company to commercialize the manufacturing of lithium-ion batteries in 1991. There are three components to this battery: a carbon anode, a lithium cobalt oxide cathode, and a non-liquid electrolyte. It was not until the late 1990s that a soft, flexible container for lithium-ion batteries was developed, resulting in the development of lithium-polymer batteries [56]. In comparison to other rechargeable batteries, Li-ion batteries have a high energy efficiency and power density, making them an excellent choice for portable devices. Because of these desires, they may be built to be lighter and smaller. Furthermore, Li-ion batteries have a wide temperature range of operation, quick charge capabilities, a reasonably long cycle life, a low self-discharge rate, and high energy, voltage, and power efficiency, among other advantages [57].

2.4 Lithium-ion Battery

Each battery is made up of three basic components: a positive electrode, a negative electrode, and an electrolyte (or electrolyte solution). In Li-ion batteries, the positive electrode, also known as the cathode, is formed of a lithium-metal-oxide compound, while the negative electrode, also known as the anode, is built of carbon, with a separating layer between them. The electrolyte in lithium batteries is likewise produced from lithium salt in an organic solvent, as is the electrolyte in lead batteries. Given the flammability of organic solvents in their capacity as electrolytes, additional precautions must be taken while using them as electrolytes. The engineering of the electrolyte structure is made more difficult by safety precautions and other steps used to improve the performance of lithium batteries. A number of different materials make up the electrolyte in these batteries, each of which serves a specific purpose. In the event that any electrolyte component performs below expectations, this will result in the battery's overall performance being compromised [58]. A view of a lithium battery cell is shown in figure 2.4.

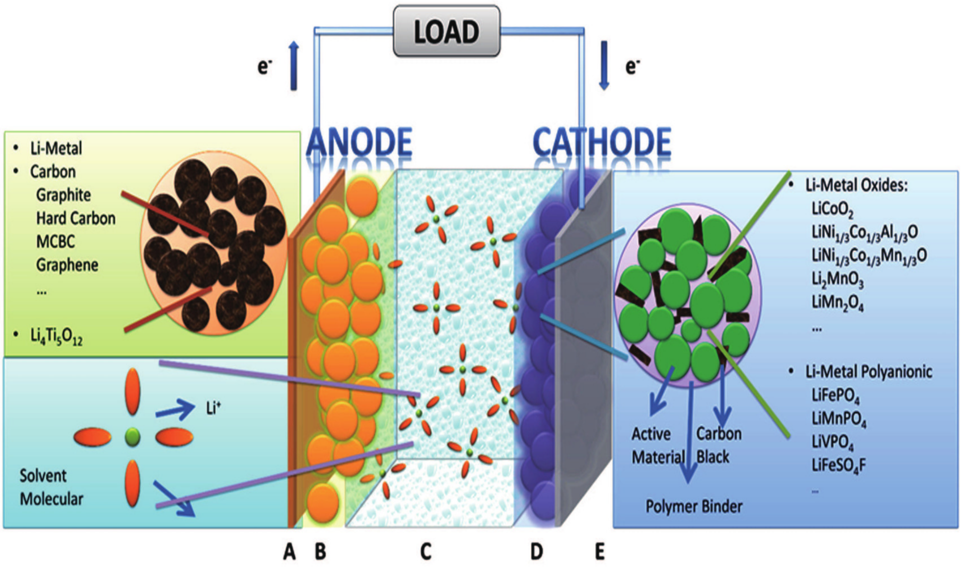

Figure 2.4: The hierarchical structure of lithium ion batteries [2]

The reaction mechanism in Li-ion batteries includes the movement of Li^+ between cathode and anode materials. During battery discharge, the electrolyte allows Li^+ transfers from the anode to the cathode. And simultaneously, for every Li^+ in the transfer, one electron will be released. The chemical reaction for the cathode and the anode can be provided by equations (2.1) and (2.2), respectively [59].

$$LiMO_2 \leftrightharpoons Li_{1-x}MO_2 + xLi^+ + xe^- \tag{2.1}$$

$$xLi^+ + xe^- + 6C \leftrightharpoons Li_xC_6 \tag{2.2}$$

In addition to the aforementioned characteristics, lithium batteries are equipped with electronic protection circuits and fuses to guard against polarization, overvoltage, overheating, and other potential safety hazards.

Different types of Li-ion batteries that function differently are made by using different materials for the cathode electrolyte. In figure 2.5, the major Li-ion properties for six types of Li-ion batteries are compared. Moreover, table 2.1 describes the performance of several Li-ion battery types [60, 61, 62, 63].

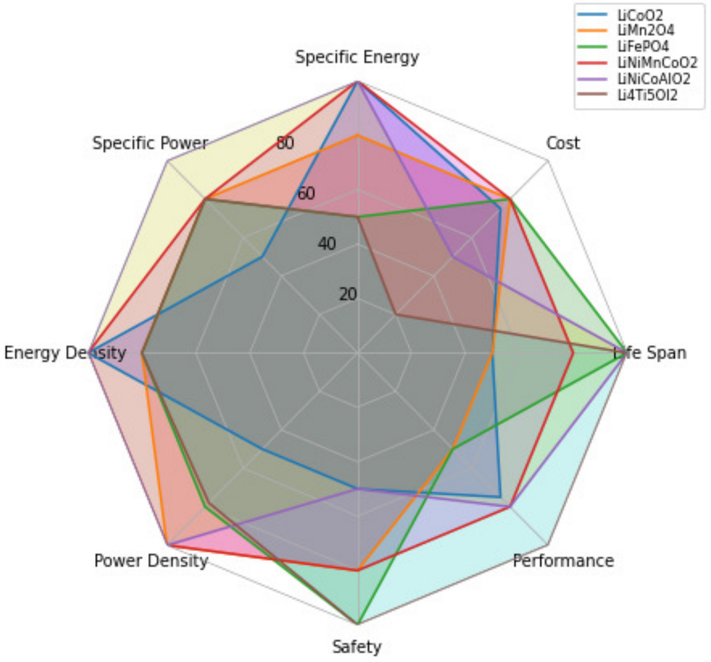

Figure 2.5: Comparison between Characteristics of different Li-ion battery types

Table 2.1: The performance of Li-ion battery types

Li-ion Battery Type	Advantage	Limitation	Applications
$LiCoO_2$	Very high specific energy	Low lifetime, limited specific power, low safety	Mobile phones, laptops, cameras
$LiMn_2O_4$	High power, moderate safety and life span	Less capacity	Electric powertrains, medical device
$LiFePO_4$	Excellent current rate, highly safe, elevated longevity	low specific energy, less voltage than other Li-ion batteries, decreased performance at lower temperature	Power tools, EVs, portable devices
$LiNiMnCoO_2$	Well performance, high capacity and power	High cost	Medical devices, Evs, industrial systems
$LiNiCoAlO_2$	Elevated specific energy, great power densities, well lifetime	High cost, low safety	Industrial systems, electric powertrains, medical devices
$Li_4Ti_5O_{12}$	Excellent safety, good stability,long life, fast charge	Low voltage, low energy density, high cost	Nano-technology applications, UPS, electric powertrains

2.5 Battery Modeling

Li-ion battery models can be classified into three major categories as mathematical, electrochemical and electrical equivalent circuit models [64, 65, 66].

2.5.1 Mathematical Models

Analytical models and stochastic models are both types of mathematical models. In the analytical model, the battery properties are represented by a few equations and different physical concepts. Stochastic battery models, like Markov chain processes, are able to model the entire battery system all at once. The purpose of stochastic models is to explain batteries theoretically, with less time wasted in comparison to electrochemical models, and to obtain better accuracy than other methods [67].

2.5.2 Electrochemical Models

Electrochemical kinetics and the charge transfer process can both be used to explain the reactions that take place inside the battery. The electrochemical models based on physical principles were developed specifically for this purpose [68, 69]. To explain the cell's potential and diffusion gradients, a set of coupled partial differential equations (PDEs) are used. Solid concentrations at positive and negative electrodes and in the electrolyte are achieved by Fick's law of diffusion as Equation(2.3): [70]

$$\frac{\partial C_s}{\partial t} = \frac{D_s}{r^2}\frac{\partial}{\partial r}\left(r^2\frac{\partial C_s}{\partial r}\right),\ \mathit{for}\ r \in (0, R_s) \tag{2.3}$$

Where D_s is the solid phase diffusion coefficient in the electrolyte. The initial conditions and Neumann boundary conditions are defined as (2.4):

$$\begin{gathered} C_{s,0} = C, \quad \mathit{for}\ C > 0\ \mathit{at}\ t = 0\ r \in (0, R_s) \\ \left.\frac{\partial C_s}{\partial r}\right|_{r=0} = 0, \quad \left.\frac{\partial C_s}{\partial r}\right|_{r=R_s} = -\frac{j^{Li} R_s}{3\varepsilon_s F} \end{gathered} \tag{2.4}$$

In (2.4) F is Faraday's number, R_s and j^{Li} denote the radius of the particle and the local volumetric transfer current density, respectively. Also, the potential distribution in the solid phase and electrolyte phase is calculated by Ohm's law as (2.5):

$$\begin{gathered} \frac{\partial}{\partial x}\left(\sigma^{eff}\frac{\partial}{\partial x}\phi_s\right) - j^{Li} = 0, \begin{cases} -\sigma^{eff}\left.\frac{\partial \phi_s}{\partial x}\right|_{x=0} = \sigma^{eff}\left.\frac{\partial \phi_s}{\partial x}\right|_{x=L} = \frac{I(t)}{A} \\ \left.\frac{\partial \phi_s}{\partial x}\right|_{x=\delta_n} = \left.\frac{\partial \phi_s}{\partial x}\right|_{x=\delta_n+\delta_{sep}} = 0 \end{cases} \\ \frac{\partial}{\partial x}\left(k^{eff}\frac{\partial}{\partial x}\phi_e\right) + \frac{\partial}{\partial x}\left(k_d{}^{eff}\frac{\partial}{\partial x}\ln C_e\right) + j^{Li} = 0, \quad \left.\frac{\partial \phi_e}{\partial x}\right|_{x=0} = \left.\frac{\partial \phi_e}{\partial x}\right|_{x=L} = 0 \end{gathered} \tag{2.5}$$

2.5.3 Electrical Equivalent Circuit Models

Electrical equivalent circuit models are based on a circuit network consisting of resistors and capacitors which are connected to a voltage source. The RC model, the Thevenin model, and the PNGV model are the essential equivalent circuit models that are used in EVs [71, 72].

2.5.3.1 RC Model

The RC model was introduced by SAFT Battery Company. The schematic of this model is illustrated in figure 2.6. This model comprises a large capacitor C_b indicates the stored capacity, and a small capacitor C_c represents the polarization. Equation (2.6) describes the electrical behavior of the RC circuit model.

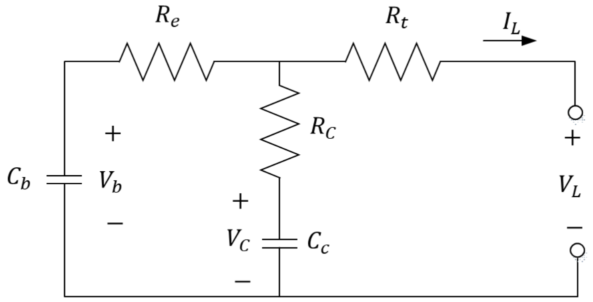

Figure 2.6: Equivalent circuit RC battery model

$$
\begin{bmatrix} \dot{V_b} \\ \dot{V_c} \end{bmatrix} = \begin{bmatrix} \frac{-1}{C_b(R_e+R_c)} & \frac{1}{C_b(R_e+R_c)} \\ \frac{1}{C_c(R_e+R_c)} & \frac{-1}{C_c(R_e+R_c)} \end{bmatrix} \begin{bmatrix} V_b \\ V_c \end{bmatrix} + \begin{bmatrix} \frac{-R_c}{C_b(R_e+R_c)} \\ \frac{R_c}{C_c(R_e+R_c)} \end{bmatrix} I_L
$$

$$
V_L = \begin{bmatrix} \frac{R_c}{(R_e+R_c)} & \frac{R_e}{(R_e+R_c)} \end{bmatrix} \begin{bmatrix} V_b \\ V_c \end{bmatrix} + \begin{bmatrix} -R_c & \frac{R_e Rc}{(R_e+R_c)} \end{bmatrix} I_L \tag{2.6}
$$

Where R_t, R_C , R_e are the terminal resistor, the capacitor resistor and the end resistance, respectively.

2.5.3.2 Thevenin Model

Thevenin theorem is a method for converting a complex circuit model to a simple equivalent circuit composed of a resistor which is placed in series with a source voltage. Figure 2.7 is usually used as a typical Thevenin model of a Li-ion battery. Model elements include a series of DC internal resistance (R_o) resistors, an RC parallel circuit network, and an ideal DC voltage source that indicates the open circuit voltage.

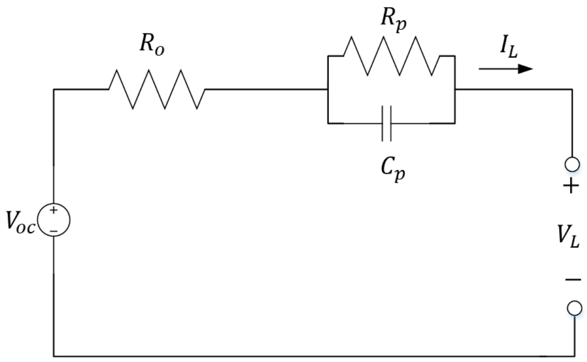

Figure 2.7: Equivalent circuit Thevenin battery model

The equation of state-space for Thevenin model is described in (2.7):

$$\begin{cases} \dot{V_p} = -\frac{V_p}{R_p C_p} + \frac{I_L}{C_p} \\ \\ V_L = V_{oc} - V_p - I_L R_o \end{cases} \tag{2.7}$$

2.5.3.3 PNGV Model

The PNGV model is proposed by The US PNGV under the Freedom CAR hybrid electric vehicles effect. This model can be generated by adding a capacitor C_o to the Thevenin model. Co indicates the changes in V_{oc} generated by the timely integration of load current (I_L).

The PNGV model is represented as (2.8), where V_{C_o} and V_{C_p} are the voltage across

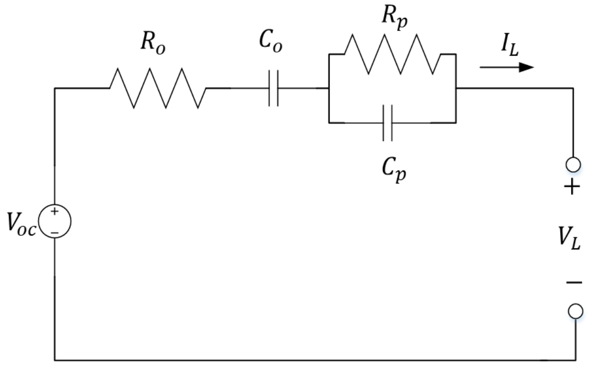

Figure 2.8: Equivalent circuit PNGV battery model

C_o and C_p, respectively :

$$
\begin{bmatrix} \dot{V}_{C_o} \\ \dot{V}_{C_p} \end{bmatrix} = \begin{bmatrix} 0 & 0 \\ 0 & \frac{-1}{R_pC_p)} \end{bmatrix} \begin{bmatrix} V_{C_o} \\ V_{C_p} \end{bmatrix} + \begin{bmatrix} \frac{1}{C_o} \\ \frac{1}{C_p} \end{bmatrix} I_L
$$

$$
V_L = \begin{bmatrix} 1 & 1 \end{bmatrix} \begin{bmatrix} V_{C_o} \\ V_{C_p} \end{bmatrix} + R_oI_L + V_{oc} \tag{2.8}
$$

2.6 Battery Management System

In contrast to public batteries, electric vehicle batteries need special attention in terms of safety since they produce a great deal of heat throughout the charge and discharge cycle, as well as when they are subjected to high power consumption. Many variables contribute to cell death include heat control, cellular equilibrium, and the proper chemical selection amongst others.

Generally, a Battery Management System (BMS) is an electronic system that manages a cell or pack of rechargeable batteries by monitoring the battery, reporting the data and balancing it, charging and discharging control, and protecting the battery from being operated outside of the Safe Operating Area (SOA). The SOA of batteries is limited by the amount of current, voltage, and temperature applied to them [73]. The main operating specifications of the BMS are shown in figure 2.9. Each of its functions is explained in detail below, individually:

Figure 2.9: The operating specifications of the BMS

2.6.1 Battery monitoring

In EVs, a chain of Li-ion battery cells in a pack is utilized. In order to safeguard the battery pack from over/under voltage, over/under current, and charging/discharging outside of a specified temperature range, the BMS can monitor the battery's total voltage, total current, and total temperature during operation of the battery.. Furthermore, because each single cell can exhibit a wide range of behavior over time, battery cell monitoring, such as voltage and temperature for each cell in the battery pack, is one of the most challenging aspects of battery management systems [74].

2.6.2 Cell Balancing and Equalization

An imbalance in the charge levels of the cells is easily detected in the battery and shown via estimates of the SOC. The balancing procedure is done by passing extra charge to an undercharged cell or the other module/pack, or by moving needed charge to an over-charged cell from nearby modules/packs. A battery equalization control may prolong the lifespan of the battery pack, reducing the likelihood of its batteries being damaged. Yet, because of the enormous battery size and expense, it is hard to do things like the monitoring and administration of each battery. For this reason, it is essential to have an improved BMS to implement effective cell monitoring and charge equalization with a basic design and control [75].

2.6.3 Thermal Management

Based on the temperature range of the battery cells, the BMS determines whether to turn on heating or cooling to keep the battery pack above or below the minimum and maximum working temperatures, respectively [76].

2.6.4 Charge and Discharge Control

The BMS regulates the current rate of the charger utilized in the battery charge procedure to maintain the battery in SOA throughout the charge and discharge of the battery [77].

2.6.5 Modelling and State Estimation

Battery state estimation, such as State Of Charge (SOC), State Of Health (SOH) and State of Function (SOF) can be computed by using the measured data. Calculating the accuracy of SOH estimates is done via fault diagnostic data and the service life forecast. The fault states, SOH, and SOC are all important factors that influence SOF. The effects of aging factor, temperature variations, SOC range, and fault conditions are considered in SOF.

2.6.6 Fault Diagnosis and Health management

Fault diagnosis is one of the most important tasks of the BMS, as it allows it to take the necessary steps to minimize disruption to the battery pack's functioning while also protecting the battery. Factors contributing to battery pack failures include overcharging, undercharging, internal short circuit, overheating, and *etc.* [78].

2.7 Renewable Energy For Charging the EVs Battery

Among the main renewable energy technologies being pushed by governments today are solar PhotoVoltaic (PV) panels, which generate electricity from sunlight. The fact that solar energy is provided by nature means that it is free and plentiful, and that it can be made accessible nearly wherever there is sunshine is another advantage. Solar PV panels have a very great future, both in terms of economic viability and in terms of environmental sustainability. Photovoltaic panels generate clean energy and electricity in a direct power production manner, and they are completely quiet in their operation. As a result, they are an excellent choice for metropolitan locations as well as residential applications. PV panels may be a cost-effective option for charging the battery in EVs [79, 80].

2.8 Discussion

This chapter reviewed briefly the history of EVs generations one of the best replacement options for conventional engine cars. The Li-ion battery has several benefits over other rechargeable batteries that may be attributed to the way that these types of batteries are often used as the primary storage device for electric vehicles. The chemical mechanism and theoretical modeling of Li-ion batteries were discussed. Additionally, the battery management and monitoring system's functionality is described in detail to enhance the current Li-ion battery performance in EVs applications. The ability to control charge and discharge, as well as protection, state estimation, energy storage, and measurement are features of BMS that are used to help improve Li-ion battery performance inEVs applications.

3

STATE OF CHARGE ESTIMATION: REVIEW METHODS

Contents

3.1 Introduction

One of the significant issues of BMS is the SOC estimation of battery. The SOC of battery is defined as the rate of the available capacity (Q_t) to its maximum capacity when a battery is completely charged (Q_{nom}) [81].

$$SOC(t) = \frac{Q_t}{Q_{nom}} * 100\% \tag{3.1}$$

$SOC = 100\%$ and $SOC = 0\%$ indicate the battery is fully charge and fully discharge, respectively. To date, various methods have been developed and introduced to SOC estimation. This chapter discusses the existing methods of state of charge estimation for Li-ion batteries.

3.2 State Of Charge estimation Methods

The accurate and reliable SOC estimation can provide a necessary evaluation factor for energy management and the control system's optimal design in EVs. Consequently, several methods have been suggested for SOC estimation. Figure 3.1 summarizes SOC estimation methods that are separated into two main categories: direct methods and indirect methods [13, 14, 82, 83]. Some of the essential SOC estimation methods are described below.

3.2.1 Direct Methods

When considering direct methods, an equation or a relationship is used to estimate SOC, which is determined by the battery's physical properties like current, voltage, and battery temperature.

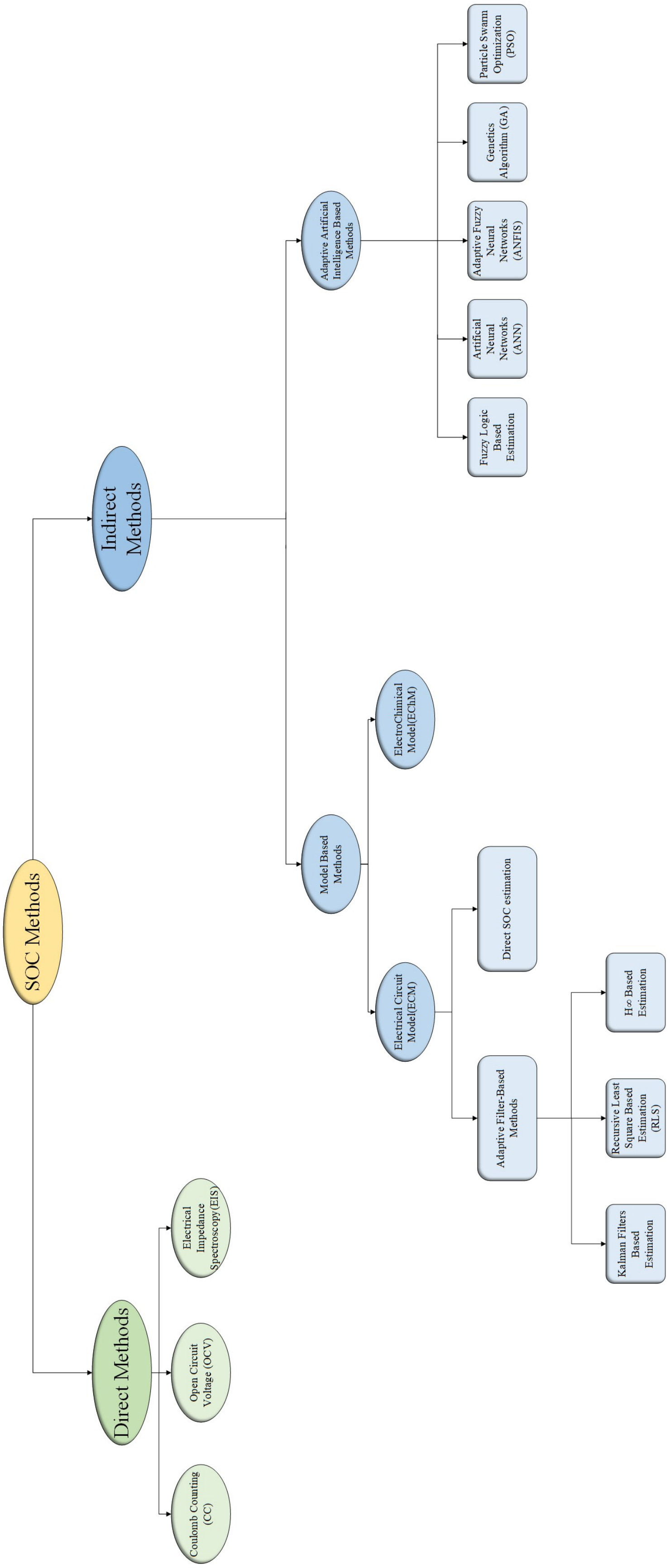

Figure 3.1: The methods of SOC estimation

3.2.1.1 Coulomb Counting estimation (CC)

The Coulomb Counting estimation method or Ampere-hour balancing method is the simplest method for SOC estimation. Due to the fact that this technique is dependent on the integration of battery current with respect to time as the battery charges or discharges, it is critical to understand the initial values of SOC

The equation of the CC method is presented in Eq. (3.2):

$$SOC(t) = (SOC(t_0) + \frac{1}{C_n}\int_{t_0}^{t_0+t} \eta I_b(dt)) * 100\% \tag{3.2}$$

Where $SOC(t_0)$ is the initial values of the SOC and I_b is the battery current. Also, η and C_n represent the discharged efficiently and the nominal capacity of battery, respectively. Although this method is very simple to implement, it has some drawbacks, including :

- The initial value of SOC can not be estimated with CC method.
- This method is an open-loop estimator, then the errors could be increased by uncertainties or disturbance.
- The accuracy of estimation is reduced by aging the battery and destruction of the battery static capacity.

[12, 84, 85].

3.2.1.2 Open Circuit Voltage (OCV)

The Open Circuit Voltage is the battery voltage under the equilibrium condition. OCV based estimation uses a relationship like (3.3) between SOC and OCV. Each type of battery has a specific relationship between its OCV and its SOC. In other words, this relationship is dependent on both the material and the capacity of the battery. Therefore, it is defined as a nonlinear function, similar to the (3.3) in Li-ion batteries [86]. In addition, as can be seen in figure 3.2 the OCV-SOC curve is changed by the temperature and current discharge. Consequently, this function is dependent on temperature and battery aging

[87].

$$SOC = f^{-1}(OCV) \tag{3.3}$$

This method needs a long time resting to estimate SOC, and as a result, it can not be implemented in real time. Additionally, the OCV technique, like the CC method, is an open-loop estimator, and consequently, it is not accurate against uncertainty.

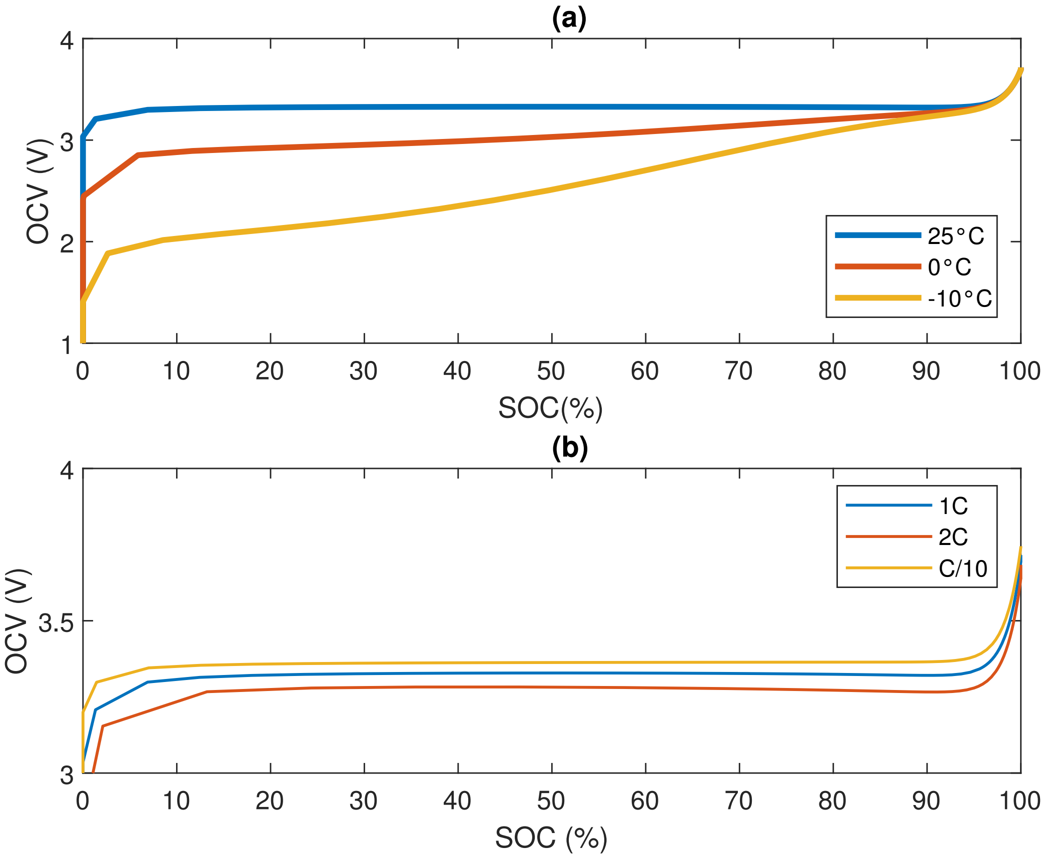

Figure 3.2: OCV *vs* SOC(%) curve discharge profile of $LiFePO_4$ measured (a) under Three temperatures and discharge current rate 1C, (b) at 25°C and three discharge current values.

3.2.1.3 Electrochemical Impedance Spectroscopy (EIS)

Electrochemical Impedance Spectroscopy is a helpful test technique for electrochemical systems. The Electrochemical Impedance Spectroscopy technique perturbs the system by applying a small AC voltage as a function of various frequencies, and the battery impedance is measured across a wide range of frequencies [88, 89]. The measured impedance is a complex number consisting of a real component (Z') and an imaginary part (Z"), which may be expressed as (3.4):

$$Z = Z^{'} + jZ^{''} \tag{3.4}$$

In [3], Wagg *et al.* demonstrated the dependency of the battery impedance on SOC, temperature, short-time prior history, and current rate. The Nyquist diagram of a battery impedance is depicted in figure 3.3, where the x axis and the y axis are the real part and the imaginary part of the battery impedance, respectively. From this figure, it is apparent that the battery impedance is more sensitive to temperature change, especially at low frequencies. As a result, it is difficult to get an accurate SOC estimation [90].

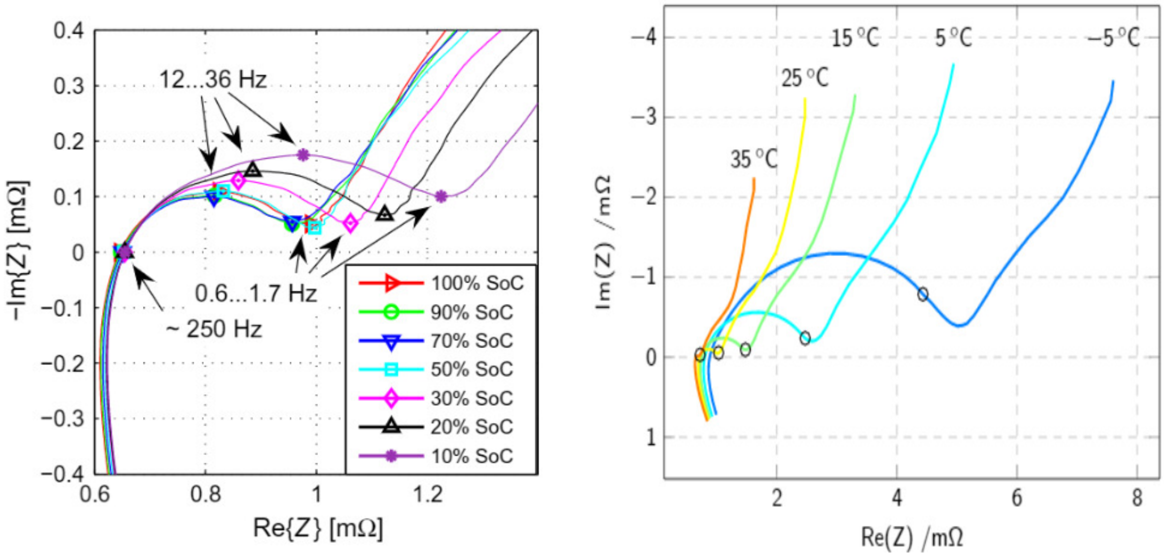

(a) (b)

Figure 3.3: Impedance spectra of a Li-ion cell (a) at different SOC at 25°C [3], (b) at approximate 50% SOC and different temperature, the point in (b) shows the 1Hz frequency [4]

3.2.2 Indirect Methods

Due to direct methods needs enough rest-time to monitor SOC, they cannot be applied while the vehicle is moving. As a result, and in order to overcome the uncertainties associated with open-loop SOC estimate methods, adaptive-based algorithms are widely investigated during the last several decades. Indirect approaches based on operational adaptive techniques propose a method for estimating SOC from battery input signals by using a model of the battery or system specification.

3.2.2.1 Kalman Filter Based Methods

Since early 20^{th} century, several studies are suggested the Kalman Filter (KF) based methods for SOC estimation [91, 92, 93]. In the context of a linear dynamic system, Kalman filtering is an algorithm that generates optimal state estimates from a series of measurements involving error over time [94]. The KF algorithm is represented by the Algorithm 1, in which, $A_k \in \mathbb{R}^{n\times n}$, $B_k \in \mathbb{R}^{n\times m}$, $C_k \in \mathbb{R}^{q\times n}$ and $D_k \in \mathbb{R}^{q\times m}$ are constant matrices, with condition $1 \leq m, q \leq n$. $\mathbf{u}_k \in \mathbb{R}^m$ is a known deterministic input, $\mathbf{w}_k$ and $\mathbf{v}_k$ are the *n-dimensional* unknown system noise vector and *q-dimensional* observation noise vector, respectively , which are associated the white noise process with known covariance. Additionally, $\mathbf{P}_k \in \mathbb{R}^{n\times n}$ is defined as the error covariance matrix.

The KF estimator for SOC based on linear state space battery model are revealed in [95, 96, 97]. Since the Li-ion batteries have a nonlinear model, The EKF is widely used for SOC estimation [91, 98, 99] .

The EKF operates on the principle of linearization of the nonlinear model, where at every time step of the state estimation, the dynamics of the nonlinear system are linearized from the estimated data using the partial derivatives and first-order Taylor series expansion. The algorithm of EKF is shown in Algorithm 2, where, $f(\mathbf{x}_k, \mathbf{u}_k)$ and $g(\mathbf{x}_k, \mathbf{u}_k)$ are the nonlinear state transition functions and nonlinear measurement functions, respectively.

Algorithm 1 Kalman Filter algorithm

```
Linear state-space system model:
        $\mathbf{x}_{k+1} = A_k\mathbf{x}_k + B_k\mathbf{u}_k + \mathbf{w}_k$
        $\mathbf{y}_k = C_k\mathbf{x}_k + D_k\mathbf{u}_k + \mathbf{v}_k$
Covariances of the two noise model:
        $\mathbf{Q}_w = \mathbb{E}[\mathbf{w}_k\mathbf{w}_k^T]$
        $\mathbf{R}_v = \mathbb{E}[\mathbf{v}_k\mathbf{v}_k^T]$
Initialization:
        $\hat{x}_0^+ = \mathbb{E}[x_0]$
        $P_0^+ = \mathbb{E}[(x_0 - \hat{x}_0^+)(x_0 - \hat{x}_0^+)^T]$
Computation:
for k=1,2,... do
        $\hat{x}_k^- = A_{k-1}\hat{x}_{k-1}^+ + B_{k-1}u_{k-1}$ {State estimation time update}
        $P_k^- = A_{k-1}P_k^+A_{k-1}^T + Q_w$ {Error covariance time update}
        $\hat{y} = C_k\hat{x}_k^- + D_k u_k$
        $K_k = P_k^- C_k^T[C_k P_k^- C_k^T + R_v]^T$ {Kalman gain matrix}
        $\hat{x}_k^+ = \hat{x}_k^- + K_k[y_k - \hat{y}_k]$ {State estimate measurement update}
        $P_k^+ = (I - K_k C_k)P_k^-$ {Error covariance measurement update}
end for
```

Algorithm 2 Extended Kalman Filter algorithm

```
Non Linear state-space system model:
        $\mathbf{x}_{k+1} = f(\mathbf{x}_k, \mathbf{u}_k) + \mathbf{w}_k$
        $\mathbf{y}_k = g(\mathbf{x}_k, \mathbf{u}_k) + \mathbf{v}_k$
Co-variances of the two noise model:
        $\mathbf{Q}_w = \mathbb{E}[\mathbf{w}_k \mathbf{w}_k^T]$
        $\mathbf{R}_v = \mathbb{E}[\mathbf{v}_k \mathbf{v}_k^T]$
Definitions:
        $\hat{\mathbf{A}}_k = \frac{\partial f(\mathbf{x}_k, \mathbf{u}_k)}{\partial \mathbf{x}_k} \Big|_{\mathbf{x}_k = \hat{\mathbf{x}}_k^+}$
        $\hat{\mathbf{C}}_k = \frac{\partial g(\mathbf{x}_k, \mathbf{u}_k)}{\partial \mathbf{x}_k} \Big|_{\mathbf{x}_k = \hat{\mathbf{x}}_k^-}$
Initialization:
        $\hat{x}_0^+ = \mathbb{E}[x_0]$
        $P_0^+ = \mathbb{E}[(x_0 - \hat{x}_0^+)(x_0 - \hat{x}_0^+)^T]$
Computation:
for k=1, 2, ... do
        $\hat{x}_k^- = f(\hat{x}_{k-1}^+, u_{k-1})$ {State estimation time update}
        $P_k^- = \hat{A}_{k-1} P_k^+ \hat{A}_{k-1}^T + Q_w$ {Error covariance time update}
        $\hat{y} = g(\hat{x}_k^-, u_k)$
        $K_k = P_k^- \hat{C}_k^T [\hat{C}_k P_k^- \hat{C}_k^T + R_v]^T$ {Kalman gain matrix}
        $\hat{x}_k^+ = \hat{x}_k^- + K_k [y_k - \hat{y}_k]$ {State estimate measurement update}
        $P_k^+ = (I - K_k \hat{C}_k) P_k^-$ {Error covariance measurement update}
end for
```

The schematic of the nRC Electrical Equivalent Circuit Models (EECM) which is generally used in EKF-based methods for SOC estimation, is illustrated in figure 3.4. The equations of these models for $0 \leq n \leq 4$, and PNGV model are listed in table 3.1 [100].

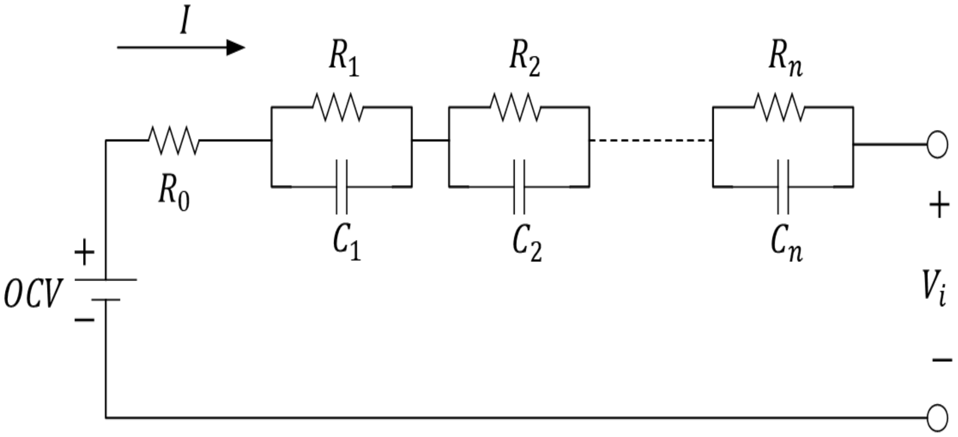

Figure 3.4: Equivalent circuit nRC battery model

Table 3.1: The Li-ion model equation base on OCV and SOC

number of n	Model name	Model equation
0	0RC(Rint model)	$V_k = OCV(Z_k) - I_k R_0$
1	1RC(Thevenin model)	$V_k = OCV(Z_k) - I_k R_0 + u_{1,k}$
2	2RC (DP model)	$V_k = OCV(Z_k) - I_k R_0 + u_{1,k} + u_{2,k}$
3	3RC	$V_k = OCV(Z_k) - I_k R_0 + u_{1,k} + u_{2,k} + u_{3,k}$
4	4RC	$V_k = OCV(Z_k) - I_k R_0 + u_{1,k} + u_{2,k} + u_{3,k} + u_{4,k}$
-	PNGV	$V_k = OCV(Z_k) - I_k R_0 + u_{1,k} + u_{cb,k}$

In table 3.1, Z_k explains the relationship between OCV and SOC. Also, $u_{n,k}$ and $u_{cb,k}$ are described by equation (3.5):

$$\begin{aligned} u_{n,k} &= \exp(-\Delta t/\tau_n) u_{n,k-1} + R_n[1 - \exp(-\Delta t/\tau_n)] I_k \\ u_{cb,k} &= u_{cb,k-1} + \frac{1}{C_b} R_1 [1 - \exp(-\Delta t/\tau_1)] I_k \end{aligned} \tag{3.5}$$

In application of SOC estimation $\mathbf{X}_k$, $\mathbf{y}_k$ and $\mathbf{u}_k$ are defined as (3.6):

$$\begin{aligned} \mathbf{x}_k &= (SOC_k, u_{1,k}, u_{2,k}, ..., u_{n,k}) \\ \mathbf{y}_k &= OCV(Z_k) - \sum_{i=1}^{n} u_{i,k} - R_0 I_k + v_k \\ \mathbf{u}_k &= I_k \end{aligned} \tag{3.6}$$

The positive aspect of the KF-based method is the accurate state estimation versus external disturbances. Despite this, KF-based estimator requires a complicated computation to be applied to the state estimate of a nonlinear system [101].

3.2.2.2 Artificial Intelligence Based Methods

Because of the Li-Ion batteries have a nonlinear and complex model, in recent years, the Artificial Intelligent methods such as Fuzzy Logic, Neural Networks (NN) and Support Vector Machines(SVMs) are considered for SOC estimation [29, 27, 102, 25, 103]. These methods are known as data-based estimators, and they operate similarly to a black-box model using known input data.

3.2.2.2.1 Fuzzy Logic Methods

Fuzzy Logic (FL) is a knowledge-based method introduced by *L.A. Zadeh* that is similar to the way humans reason [104]. The FL approach simulates the human decision-making process by considering all possible intermediate states between the digital values of "yes" and "no". FL is an appropriate data-based algorithm for nonlinear and complex models.

FL system consists of a fuzzifier, a fuzzy rule base, a fuzzy inference engine, and a defuzzifier. The fuzzy rule bases includes a collection of If-then rules, such as following:

$$R^{(l)} : IF\{x_1 \ is \ F_1^l \ and... \ and \ x_n \ is \ F_n^l\} \ THEN \ y \ is \ G^l, \ l = 1, ..., M \tag{3.7}$$

That $X = [x_1, x_2, ..., x_n]^T \in U$ is the input and $y \in V$ is the output of FL system. F_i^l

and G^l are fuzzy sets in U_i and V. The mapping from input sets to output is performed with a inference engine. Moreover, the fuzzifier maps a crisp point from X into fuzzy set in U and defuzzifier maps fuzzy sets in y to a crisp point in V. Figure 3.5 shows the diagram of FL system.

Villanova University worked on the implementation a three-input single-output Sugeno fuzzy model for SOC estimation by impedance parameters [105, 106]. Singh *et al.* developed a FL-based SOC estimator in application of portable defibrillators, which was published in [107]. In this estimator the fuzzy rule based were generated from voltage recovery measurements and ac impedance of the battery as input fuzzy set, and SOC as output fuzzy set. More recent attention has focused on the applied fuzzy logic to estimate SOC by combining other methods. This is covered in more detail in the section Hybrid methods.

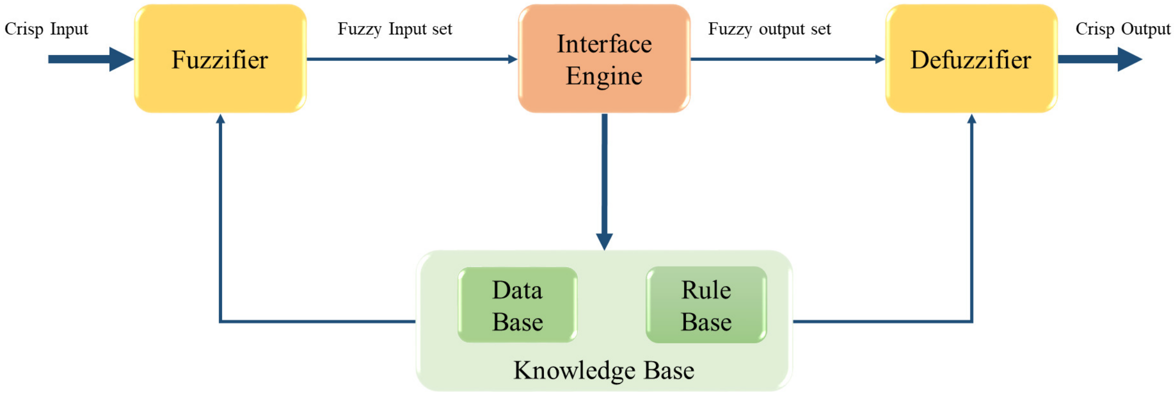

Figure 3.5: Block diagram of Fuzzy Logic System

3.2.2.2.2 Neural Networks-Based Methods

Neural Networks (NNs) are a series of intelligent computational algorithms inspired by the human neurons system. Numerous studies have attempted to estimate SOC by Feed Forward NNs [108, 109, 29, 110]. The common structure of feed forward NNs is illustrated in figure 3.6. Each NN contains at least three layers: one Input layers, the Hidden layers that can more than one layer, and one Output layer. The number of nodes in input layer is equal to input variable.

Jansen *et al.* [111] are proposed a Back-Propagation Neural Network (BPNN) based on measured impedance and frequency measurement for SOC estimation. They were successful in increasing the accuracy of error estimates on batteries that were becoming older. Also, an NNs model with four variables in the input layer (Voltage, current, temperature and the battery's resistance), one hidden layer with 30 node and SOC as an output layer is presented in [112].

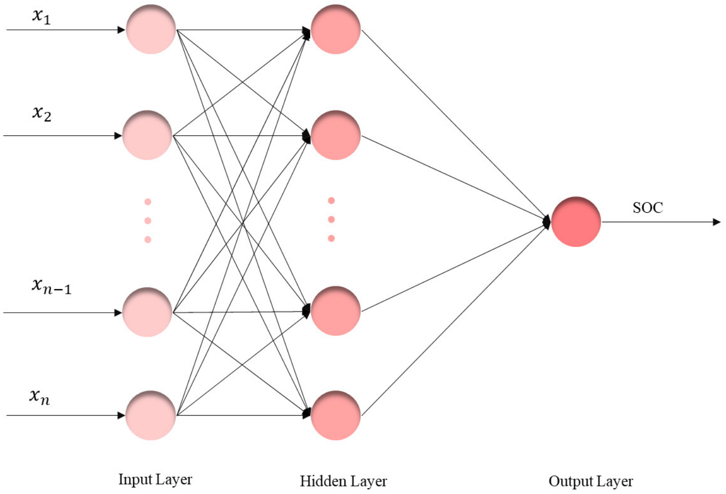

Figure 3.6: Block diagram of Neural Network System

NNs algorithms, despite the fact that they are self-learning and model-independent, are not capable of providing great accuracy. In order to get high accuracy using NNs algorithms, it is necessary to combine this technique with filtering algorithms such as KF. According to [29], the Max SOC estimate error by the NNs method was 2.5%, whereas this value dropped to 0.5% when the NNs was used in conjunction with the UKF algorithm.

3.2.3 Hybrid methods

In recent years, researchers are looking into hybrid algorithms as a means of improving the accuracy and efficiency of estimation approaches. It was tried by the authors of [113] to reduce the chattering of SOC estimations by employing a FL system in conjunction with a sliding mode controller. In [114], estimation of time-varying dynamic systems is accomplished by the use of a mixture of the EKF and CC techniques. According to

[115, 116], a hybrid intelligent algorithm composed of Fuzzy Logic and adaptive Neural Networks, which is known as ANFIS, is proposed.

3.3 Discussion

The various techniques of SOC estimation, as well as the difficulties associated with them, are discussed in this chapter. Table 3.2 contains a comparison of several techniques with an emphasis on their benefits and drawbacks. SOC estimation using deep learning algorithms is a relatively recent subject in the field of machine learning. In this thesis, three deep learning algorithms based on Deep Recurrent Neural Network (DRNN) are suggested as a method for SOC estimation in the EVs, taking into account the advantages and limits of prior work. Following the application of these techniques to a single cell of a Li-ion battery, the Bidirectional LSTM model is utilized for SOC estimate of the battery pack in Tesla's electric vehicle. A battery's nonlinear model requires complicated mathematical computations, especially in a battery pack. As a consequence, using data-driven techniques is becoming more essential. Furthermore, while comparing samples NNs and FL, it is shown that DRNN provides superior results and higher accuracy without the need of filters. Increased depth of networks aids in improving the accuracy of the approximation of the nonlinear model system.

Table 3.2: summary of SOC estimation methods with the advantages and disadvantages

Methods	Advantages	Disadvantages
CC	• Easily implemented • Low Power consumption	• Low accuracy against uncertain disturbances • High dependency to initial values of SOC
OCV	• Sample and easy to implement • high accuracy	• Need long rest time to reach a stable condition • Not suitable for online test
EIS	• Online method • inexpensive	• High dependency to temperature • Not practical for EVs which charging with different current
KF	• High Accuracy state estimation versus external disturbances	• Highly dependent on the model and sensor precision • Has complex mathematical calculations • Not suitable for nonlinear system
EKF	• Predicts a non-linear dynamic state with good precision	• Not proper for system with highly non-linear • Have limitation in linearization accuracy from jacobian matrices
UKF	• Not needed to Jacobian matrix and gaussian noise	• Weak robustness owing to uncertainty and disturbances in modeling
H∞	• Good accuracy • Time efficiency • Satisfactory computational cost	• Non-linear constraints are not well-handled • Deviation from accuracy by aging, hysteresis and temperature
RLS (Recursive Least Square)	• high precision • noise reduction in the measured voltage	• Heavy computation • Unstable operation if the forgetting values factor is not appropriate
NN	• Independence of battery model	• require a large training data set and memory storage
FL	• work well in nonlinear system modeling • good performance against temperature	• computational complexity
Hybrid Methods	• Low cost • improve the efficiency	• Difficulty level of implementation

4

STATE OF CHARGE ESTIMATION WITH DEEP RECURRENT NEURAL NETWORK METHODS

Contents

4.1 Introduction

Recurrent Neural Networks (RNNs) are a type of deep learning methods created in the 1980s [117] yet widely used only in the last few years. These types of neural networks are beneficial for serial or sequencing data.

In RNNs, each neuron or processing unit can manage its internal state or memory to maintain the previous input information. This feature is critical in many applications related to serial data. The main idea behind this type of architecture is the exploitation of this series structure. The name of this neural network is derived from the fact that these types of networks operate recursively. An operation is performed for each element of a sequence (word, sentence, etc.), and its output depends on the current input and previous operations [118]. It means the output at time t is achieved by combining the output network at $t-1$ with the new network input at time t. With these cycles, information can be passed from one step to the next step. In other words, these types of networks have a loop within themselves, which they can pass information through the input of neurons.

The structure of RNNs is shown in figure 4.1, where the black square represents the time delay at each time step.

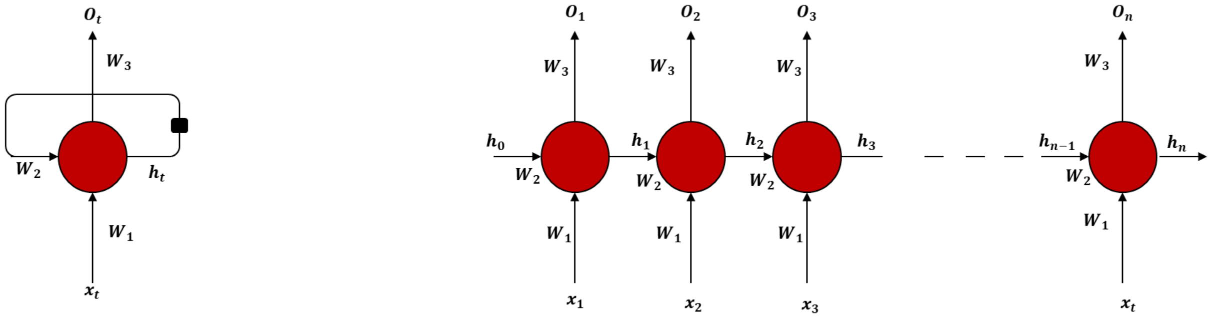

Figure 4.1: The structure of a Recurrent Neural Network for n inputs.

The network's operation is completely understandable when the chain formed after opening this computational graph is viewed. Now, this is an architecture that can receive different inputs x_t and generate o_t outputs at each time step. It also contains a memory state h_t that maintains the information about what happened on the network until the time (t). W_1, W_2, and W_3 in figure 4.1 indicate the weights of input neuron, recurrent neuron, and output layer, respectively.

In this chapter, three Deep Recurrent Neural Network (DRNN) algorithms for estimating SOC are argued. Theoretically, RNNs should have the ability to use previous data for estimation of any future one. In practice, however, this is not the case, and with expanding the sequence, traditional RNNs are unable to learn the information. For this reason, the use of RNNs was stopped for a while until outstanding results were obtained using the long-term and short-term memory unit (Long-Short Term Memory (LSTM)) in the neural network. Unlike traditional RNNs, LSTMs are not in trouble in dealing with long sequences, using a designed mechanism. Additionally, in [119], Chung et al. introduced a new gating mechanism in RNNs. The Gated Recurrent Units (GRUs) is an improved version of standard RNNs. GRUs uses two gate units to decide between beneficial and not functioning data.

4.2 Long-Short Term Memory Algorithm

LSTM, in fact, emerged in 1995 to improve RNNs in dealing with sequential data, and solving the problem of the disappeared gradient phenomenon [120]. Sepp Hochreiter *et al.* [120] explain that “long-term memory” in LSTM refers to acquired weights and “short-term memory” represents internal cellular states. The major change in this network is replacing the hidden layer of the RNNs with a block called the LSTM block and its most incredible feature is the ability to learn long-term dependencies that are not possible using RNNs [121]. To predict the next step, one needs to update the weight values on the network, which requires maintaining the initial step’s information. An RNN can only learn a limited number of short-term relationships, but long-time series such as 1000 steps are not considered by the RNNs, while LSTMs can properly learn these long-term dependencies.

All RNNs are in the form of repetitive sequences of neural network modules (units). In standard RNNs, these repeatable modules have a simple structure: for example, they only contain a hyperbolic tangent (tanh) layer. But in LSTM, instead of only one layer, four layers communicate in a special structure.

In figure 4.2, x_t is the input, h_t is the output of the LSTM unit at time t, and h_{t-1} is the output of the previous LSTM block.

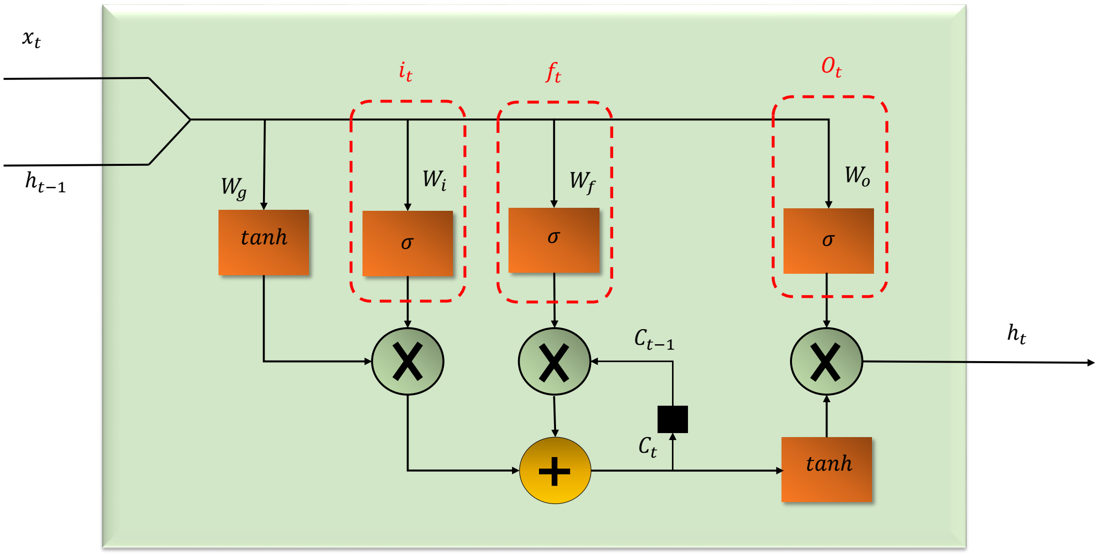

Figure 4.2: Long Short-Term Memory block. x_t is the input, h_t is the output of the LSTM unit at time t, and h_{t-1} is the output of previous LSTM block.

The initial phase in the LSTM is deciding what information should be discarded from the cell state. This decision is made by a sigmoid (σ) layer, shown in Equation (4.1), called the forget gate layer (f_t). The next step is deciding what new information has to be save in the cell state. This decision contains two parts. First, a sigmoid layer called the input gate (i_t) decides which values will be updated with Equation (4.2). The next step, represented in Equation (4.3), is a *tanh* layer that makes the vector of values called "memory cell" (C_t) that could be added to the state cell. By combining these two steps, the state cell (h_t) can be updated within the next step. Finally, it must be determined what information is to be transmitted to the output (O_t). This output will be based on the state cell, however, it will pass via a specified filter. The formula for LSTM are expressed below.

$$f_t = \sigma(W_f[h_{t-1}, x_t] + b_f) \tag{4.1}$$

$$i_t = \sigma(W_i[h_{t-1}, x_t] + b_i) \tag{4.2}$$

$$C_t = f_t * C_{t-1} + i_t * \tanh(W_g[h_{t-1}, x_t] + b_g) \tag{4.3}$$

$$O_t = \sigma(W_o[h_{t-1}, x_t] + b_o) \tag{4.4}$$

$$h_t = O_t * \tanh(C_t) \tag{4.5}$$

Where the initial values of C_t and h_t are $C_0 = 0$ and $h_0 = 0$. W_f, W_i, W_g, W_o are respectively the weights of the forget gate, input gate, memory cell, and output gates, and b_f, b_i, b_g, b_o are the associated biases. The gate activation function and the output activation function are shown by σ and tanh, which are defined in the Equations (4.6) and (4.7), respectively.

$$\sigma(x) = \frac{1}{1 + \exp(-x)} \tag{4.6}$$

$$\tanh(x) = \frac{\exp(x) - \exp(-x)}{\exp(x) + \exp(-x)} \tag{4.7}$$

4.3 Bidirectional LSTM for SOC Estimation

Bidirectional LSTM (BiLSTM) networks include two hidden layers, which are coupled to one output and have opposite orientations. The first hidden layer is in the forward direction of the input sequences from time $t-1$ to time T, and the second is in the opposite direction of the input sequences from time T to time $t-1$. The output layer is generated by the combination of the output of the forward direction, $\overrightarrow{h_t}$, and the backward direction output, $\overleftarrow{h_t}$, as shown in equation (4.8).

$$\hat{y}_t = \sigma(\overrightarrow{h_t}, \overleftarrow{h_t}) \tag{4.8}$$

The unfolded BiLSTM architecture is illustrated in figure 4.3.

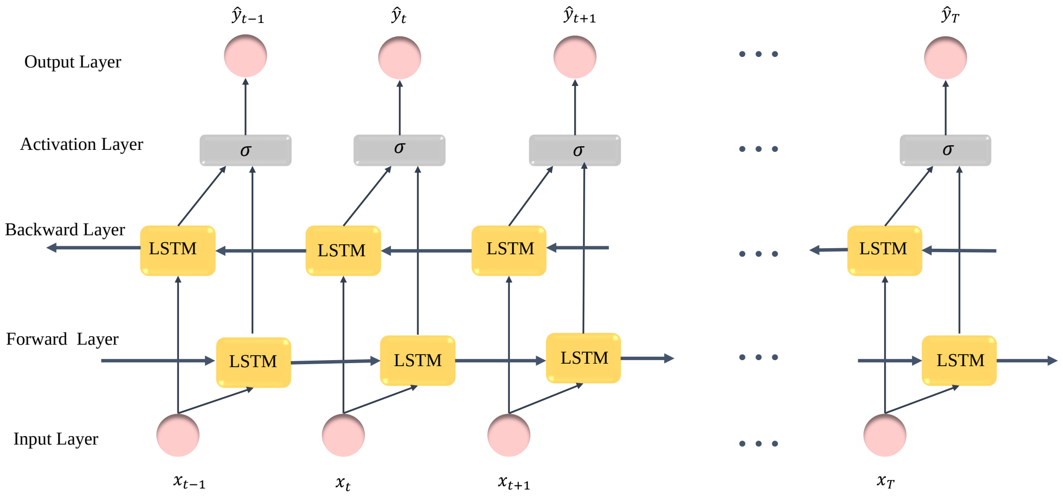

Figure 4.3: Structure of unfolded BiLSTM network. x_t and $\hat{y}_t$ represent the input and output variables at time t, respectively. σ is the activation function for combining the output of forward layer and backward layer.

The BiLSTM network proposed in this thesis for SOC estimation contains one input layer with three variables, a BiLSTM hidden layer with n units, an LSTM hidden layer with m units, and a single variable output layer. The structure of the proposed BiLSTM is depicted in figure 4.4. The input vector and output variable at time t are denoted by

$\mathbf{x}_t = \{V_t, I_t, T_t\}$ and $S\hat{O}C_t$, respectively.

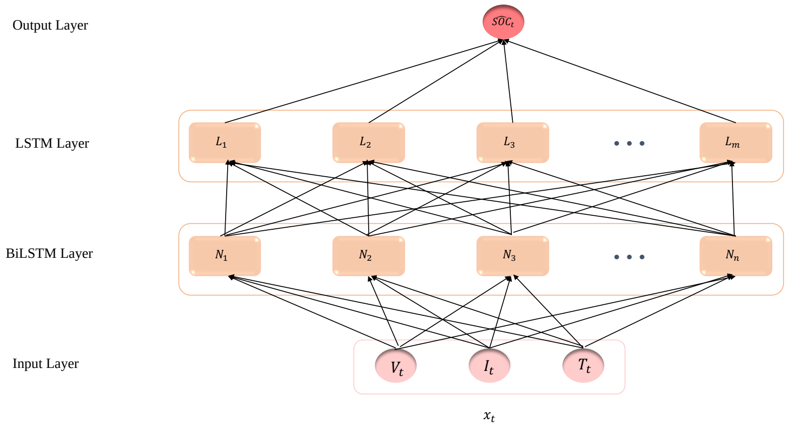

Figure 4.4: BiLSTM architecture for SOC estimation with two hidden layers. The first hidden layer is a BiLSTM layer with n units and the second one is a one directional LSTM with m unit. $x_t = \{V_t, I_t, T_t\}$ and $\hat{y}_t = S\hat{O}C_t$ represent the input and output variables at time t, respectively.

4.4 LSTM Algorithm for SOC Estimation

In this inquiry, an LSTM structure is used for the SOC estimation of a one-cell Li-ion battery with voltage (V), current (I), and temperature (T) as input variables and the SOC of the battery as the output. The whole structure is depicted in figure 4.5 for implementation on multiple GPUs. Three LSTM networks are used for the inputs. In fact, each input variable contains two hidden layers with k and l LSTM units, respectively, which work in parallel on three GPUs. The concatenation of these layers is realized to regularize the output with a dense layer, which is a linear operation that relates every input to every output with the following equation:

$$S\hat{O}C_t = Wh_t + b \tag{4.9}$$

where W and b are defined, respectively, as the weight matrices and biases of full connected layers. To implement this method and the mathematics operations, Tensorflow framework is used.

The flowchart of this program is shown in figure 4.6.

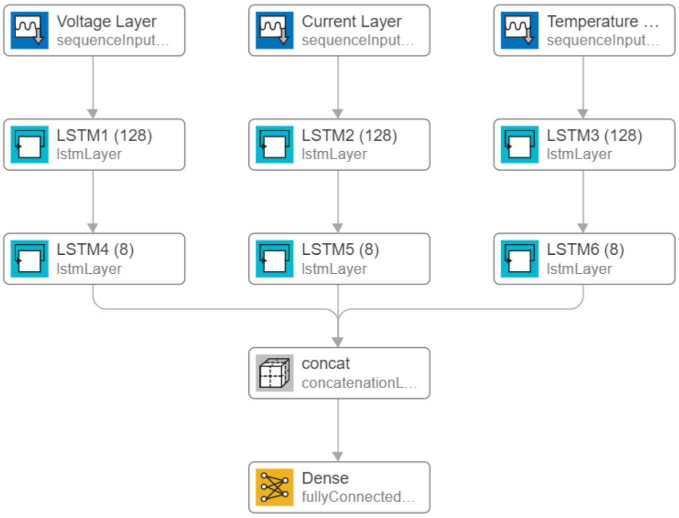

Figure 4.5: The proposed structure of the LSTM model for the SOC estimation.

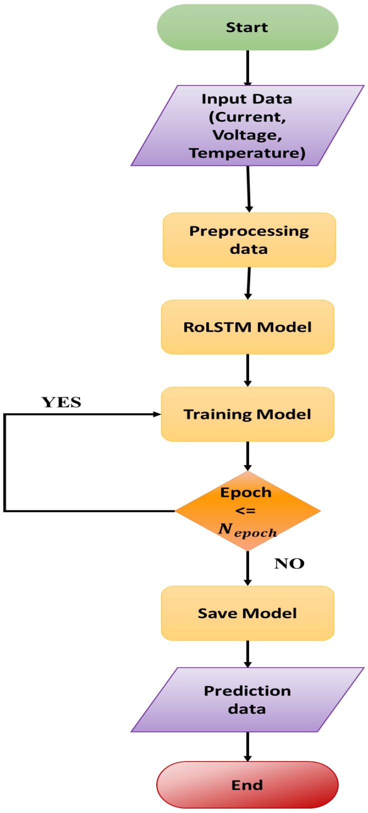

Figure 4.6: The flowchart of RoLSTM algorithm for SOC estimation.

4.5 Gated Recurrent Units for SOC estimation

In comparison with other RNNs, GRUs has a simple structure, and is robust against vanishing gradient. The structure of GRU block is depicted in figure 4.7.

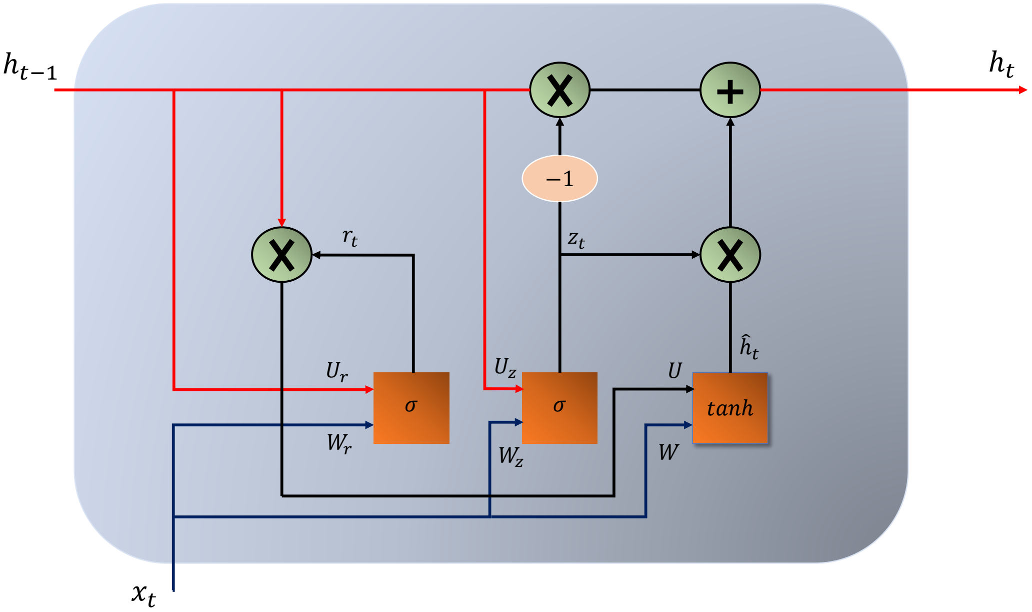

Figure 4.7: Gated Recurrent Unit block. σ is the gate activation function, tanh is the output activation function, and h_{t-1} is the output of hidden layer node at previous time.

The GRU block contains two gates: the update gate and the reset gate. The update gate, z_t, controls how much of the previous information is relayed to the future. r_t is the reset gate, which selects what the past information to forget based on its value. The equations of the GRUs method are presented in equation (4.10).

$$\begin{aligned} z_t &= \sigma(W_z x_t + U_z h_{t-1} + b_z) \\ r_t &= \sigma(W_r x_t + U_r h_{t-1} + b_r) \\ \hat{h_t} &= \tanh(W x_t + r_t \odot U h_{t-1} + b) \\ h_t &= (1 - z_t) \odot h_{t-1} + z_t \odot \hat{h_t} \end{aligned} \tag{4.10}$$

Where, W_z, W_r and W are the three connection weight matrices for inputs. U_z, U_r

and U are the weight matrices for the output of the hidden layer node at the previous time, and b_z, b_r and b are the bias parameters. $\odot$ is used to calculate the Hadamard (element-wise) product. $\hat{h_t}$ expresses the current memory content, and h_{t-1} is the output of the hidden layer node at the previous time. σ and tanh represent the gate activation function and the output activation function, respectively, determined by the following equations:

$$\sigma(x) = \frac{1}{1 + \exp(-x)} \tag{4.11}$$

$$\tanh(x) = \frac{\exp(x) - \exp(-x)}{\exp(x) + \exp(-x)} \tag{4.12}$$

The proposed Adaptive GRUs network in this work for SOC estimation, uses the voltage V_t, current I_t and the temperature T_t of the battery as the input variables, and the SOC of the battery SOC_t as the output of the network at time step t. The structure of the GRUs network for SOC estimation is shown in figure 4.8. This network contains two hidden layers with k and l units. Hence, in figure 4.8, $h_t^1(k)$ represents the k^{th} unit of the first hidden layer, and $h_t^2(l)$ is the l^{th} unit of the second hidden layer at time t. For the regression output, a Dense layer is used.

Here are the steps for implementing the GRUs technique of estimating SOC:

1. Normalize the dataset after dividing it into training and validation datasets. The dataset consists of input and output variables.
2. Set the input layer parameters, hidden layers units, and output layer parameters.
3. Define the activation functions, loss functions and optimization methods.
4. Configure the evaluation function and train the GRUs. The network parameters will be self-learned because GRUs is a self-learning approach.
5. Validate the GRUs network with the validation dataset for SOC estimation.

This method is implemented with Tensorflow framework in Keras library.

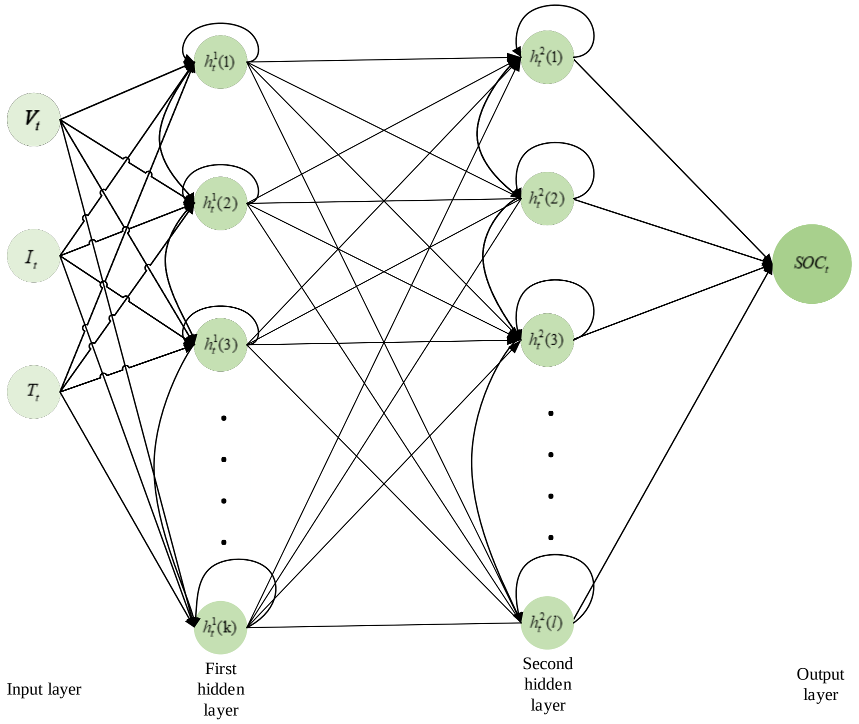

Figure 4.8: Structure of the developed Adaptive GRU network for SOC estimation. V_t, I_t and T_t represent the Voltage , Current and the Temperature at time t, $h_t^1(k)$ is the k^{th} unit of first hidden layer and $h_t^2(l)$ shows the l^{th} unit of second hidden layer at time t

4.6 Optimization Algorithms

The deep learning algorithm's primary goal is to develop a model that achieves high performance and makes accurate predictions. The weights and biases of the network must be updated on a regular basis in order to keep the system losses as low as possible.

Following the transfer of training data to the network, random values are used to determine the initial values of system weight and bias, which are then used to start the training procedure. By activating the units in each layer, the result is passed to the next layer to generate the SOC estimation in the output layer. The system loss function is determined after comparing the estimated value to the true value. Utilizing this value, as well as an appropriate optimizer to minimize the loss function, the new weights and biases are computed. In order to prepare for the next training session, these values are returned to the units inside the network layers. Two optimization algorithms are used in this work, which are described in further detail below.

4.6.1 Adaptive Moment Estimation (Adam) Algorithm

Adaptive Moment Estimation (Adam) is an adaptive learning rate optimization method that works with first-order gradients and is based on the concept of learning rate optimization. More specifically, estimations of the first and second moments of gradients are utilized to compute adaptive learning rates for each weight parameter.

Algorithm 3 Adam algorithm. Default setting for parameters are $\alpha = 10^{-4}$, $\beta_1 = 0.9$, $\beta_2 = 0.999$ and $\epsilon = 10^{-8}$.

```
Require: $\alpha$: Learning rate
Require: $\beta_1, \beta_2 \in [0, 1)$: Exponential decay rates for the moment estimates
Require: $L(W)$: Loss function
Require: $W_0$: Initial parameter vector
  $m_0 = 0$ (Initialize first moment vector)
  $v_0 = 0$ (Initialize second moment vector)
  $t = 0$ (Initialize timestep)
  while stopping condition is not achieved do
          $t = t + 1$
          $g_t = \nabla L_W(W_{t-1})$
          $m_t = \beta_1 m_{t-1} + (1 - \beta_1) g_t$
          $v_t = \beta_2 v_{t-1} + (1 - \beta_2) {g_t}^2$
          $\hat{m}_t = \frac{m_t}{1 - {\beta_1}^t}$
          $\hat{v}_t = \frac{v_t}{1 - {\beta_2}^t}$
          $W_t = W_{t-1} - \hat{m}_t \frac{\alpha}{\sqrt{\hat{v}_t} + \epsilon}$
  end while
  return $W_t$
```

In Algorithm 3, L is the loss function that is evaluated under Mean Square Error with (4.13):

$$L = \sum_{t=0}^{n} \frac{1}{n}(SOC_t - S\hat{O}C_t)^2 \tag{4.13}$$

where n is the number of data points, SOC_t and $S\hat{O}C_t$ are measured and predicted capacity of battery at time step t, respectively.

4.6.2 Robust and Adaptive Online Optimization method

A Robust and Adaptive Online Optimization Algorithm (RoAdam) is proposed in [42] to train the system and adjust the network's weights and biases. RoAdam is depending on gradient and the squared gradient. The algorithm of RoAdam is described in (4.14). $\eta = 0.0005$ is the training step size, $\beta_1 = 0.9$, $\beta_2 = 0.999$ and $\beta_3 = 0.999$ are exponential decay rates, W_t is the weights vector of the model in time step t and $\epsilon = 10^{-8}$ is a constant. The initial values of the first moment of the gradients, m_t, and the second moment of the gradients, v_t, are zero. r_t is defined as a relative prediction error term of the loss function.

$$\begin{aligned}
g_t &= \nabla L_W(W_{t-1}) \\
m_t &= \beta_1 m_{t-1} + (1-\beta_1)g_t \\
v_t &= \beta_2 v_{t-1} + (1-\beta_2){g_t}^2 \\
\hat{m}_t &= \frac{m_t}{1-{\beta_1}^t} \\
\hat{v}_t &= \frac{v_t}{1-{\beta_2}^t} \\
r_t &= \|L(W_{t-1})/L(W_{t-2})\| \\
d_t &= \beta_3 d_{t-1} + (1-\beta_3)(r_t) \\
W_t &= W_{t-1} - \hat{m}_t \frac{\eta}{d_t\sqrt{\hat{v}_t} + \epsilon}
\end{aligned} \tag{4.14}$$

L is the loss function that is calculated considering (4.15):

$$L = \frac{1}{n}\sum_{t=0}^{n} |SOC_t - S\hat{O}C_t| \tag{4.15}$$

where n is the number of data point, SOC_t and $S\hat{O}C_t$ are respectively actual and predicted values of state of charge at time step t.

To guarantee the stability of the relative prediction error, a threshold is intended for r_t. Then r_t will be changed as (4.16).

$$r_t = \begin{cases} min\{max\{k, \|L(W_{t-1})/L(W_{t-2})\|\}, K\}, & \text{if} \|L(W_{t-1})\| \geq \|L(W_{t-2})\| \\ \\ min\{max\{1/K, \|L(W_{t-1})/L(W_{t-2})\|\}, 1/k\}, & Otherwise \end{cases} \tag{4.16}$$

Where, k=0.1 and K=10 are the lower and upper thresholds, respectively.

4.7 Data Preprocessing

Since deep learning methods are defined as data-base techniques, data is just as important as the model algorithm in terms of performance. In reality, when deep learning models are trained with relevant, accurate, and adequate data, they may perform exceptionally well. As a result, data preparation is an extremely crucial step before constructing a model.

Normalization is essential due to the differences in the ranges of voltage, current, and temperature, all of which are included in the input data for the SOC estimation. Data is normalized in the range[-1,1] using the following formulas for the input:

$$x = [((x_{raw} - x_{min})/(x_{max} - x_{min})) * (max - min)] + min \tag{4.17}$$

In (4.17), the minimum and maximum values of input vector x_{raw} are shown by x_{min} and x_{max}, respectively. In addition, max equals 1 and min is -1. To scale the testing dataset, the maximum and minimum values of training inputs must be used.

Moreover, the input datasets for the LSTM and GRUs should be three-dimensional (3D), as stated by the definition (Samples, Time steps, Features).

Samples indicate the number of sequences, Time steps symbolize the number of observations in each sample, and Features represent the number of features for each element in the samples. The input datasets must be normalized and converted to a 3D array for utilization as a network input during the preprocessing step. Another parameter that must be properly adjusted in time series data preprocessing is the sample frequency. The sampling rate of raw data is set to 1Hz in this case.

4.8 Hyperparameters Tuning

Hyperparameters are defined as parameters that control the training process. They are comprising two parts:

- Model-specific hyperparameters: including network structure variables, like number of layers and number of units in each layer.
- Optimization hyperparameters: the associated variables with the optimization and training process, such as learning rate and batch size.

In general, there is no clear method for determining the right number of layers and units inside them. A trial-and-error approach is usually employed to determine the ideal model structure in these cases. The deeper learning capacity is required for more complicated functions. In this case, we start with one hidden layer and 64 units in it. Training loss data from varying the number of layers and units are given in the following chapter.

4.9 Discussion

Since battery discharge is a time series and sequential process, RNNs are more suited to estimating SOC than other data-driven algorithms. This chapter was presented new DRNN-based algorithms for SOC estimation in Li-ion batteries. The structures of BiLSTM, LSTM, and GRUs estimators have been explained. More gates in the hidden units of these algorithms allow them to overcome the issue of the vanishing gradient in the simple DRNN. Moreover, The BiLSTM is able to manage long-term relationships from both the previous and the future directions. This feature allows it to learn more sequential data and improves estimate accuracy. The results provided in the next chapter depict the performances of these methods for one cell Li-ion.

5

EXPERIMENTAL RESULTS FOR STATE OF CHARGE ESTIMATION OF ONE CELL LI-ION BATTERY

Contents

5.1 Introduction

In this Chapter, the experimental results to evaluate the SOC of single cell Li-ion battery by the BiLSTM, the RoLSTM, and the GRUs algorithms are presented and examined in detail. All programs are developed in Python by using Tensorflow and Keras libraries. Three Nvidia Tesla 100 GPUs from the Strasbourg University Computing Centre are employed for the learning process. GPU is a great tool to speed up a deep neural network data pipeline. The large number of cores in GPU improve processing power. Also, In contrast to CPUs, which have limited memory bandwidth, GPUs are capable of moving much greater amounts of information over the same time frame (as much as 750GB/s compared to only 50GB/s for CPUs). One of the greatest advantages of GPUs is their potential for parallelism, and this capability means you can use them in a variety of ways, including combining them in clusters and distributing jobs throughout the cluster. As a consequence, the Strasbourg University Computing Center helps us in using more data for system training and defining bigger sequences in each batch to improve system accuracy.

For the BiLSTM estimator, the impact of the number of hidden layers and units is discussed in detail. Furthermore, all of these algorithms are implemented at changing temperatures, which is an essential aspect of them.

5.2 Battery Specification and Experimental Conditions

To apply our methods, the database related to the Panasonic 18650PF Li-ion battery is used. The Panasonic 18650PF Li-ion battery is employed in some Tesla EVs. This database was created by McMaster University in Ontario (Canada) [122]. The battery parameter specifications are listed in Table 5.1.

Panasonic NCR18650PF cell discharge datasets are generated from various standard drive cycles in the United States, including the Los Angeles 92 (LA92), Supplemental Federal Test Procedure Driving Schedule (US06), Highway Fuel Economy Test (HWFET), and Urban Dynamometer Driving Schedule (UDDS), with a variety of current steps and temperatures. Figure 5.1 presents the drive cycle power profiles of the Panasonic

NCR18650PF cell for different drive cycles. The negative power represents the discharge power, whereas the positive power represents the charge power. The current, voltage, and capacity of battery for a sample drive cycle utilized in the training process are illustrated in figure 5.2.

Table 5.1: The specification of the Panasonic 18650PF battery parameters

Item	Specification
Capacity	Min.2750mAh Typ.2900mAh
Nominal voltage	3.6V
Min/Max Voltage	2.5V /4.2V
Charging	CC-CV, Std. 1375mA, 4.20V, 4.0 hrs
Temperature	Charge and Discharge: 0°C to 45°C Discharge: $-20°C$ to 60°C Storage: $-20°C$ to 50°C
Energy density	Volumetric:577 Wh/l Gravimeteric: 207 Wh/kg

In this study, the Mean Absolute Error (MAE), Root Mean Square Error (RMSE), and Maximum Error (MAX) are used to evaluate the performance of the suggested network for SOC estimation. The MAE, RMSE, and MAX are calculated using equations (5.1) - (5.3), respectively.

$$MAE = \frac{1}{n}\sum_{t=0}^{n}|SOC_t - \hat{SOC}_t| \tag{5.1}$$

$$RMSE = \sum_{t=0}^{n}\sqrt{\frac{1}{n}(SOC_t - \hat{SOC}_t)^2} \tag{5.2}$$

$$MAX = \max|SOC_t - \hat{SOC}_t| \tag{5.3}$$

where SOC_t and $\hat{SOC}_t$ are shown the measured value and the estimated value at timestep t, respectively. As well as, n is the number of data point in the sequence.

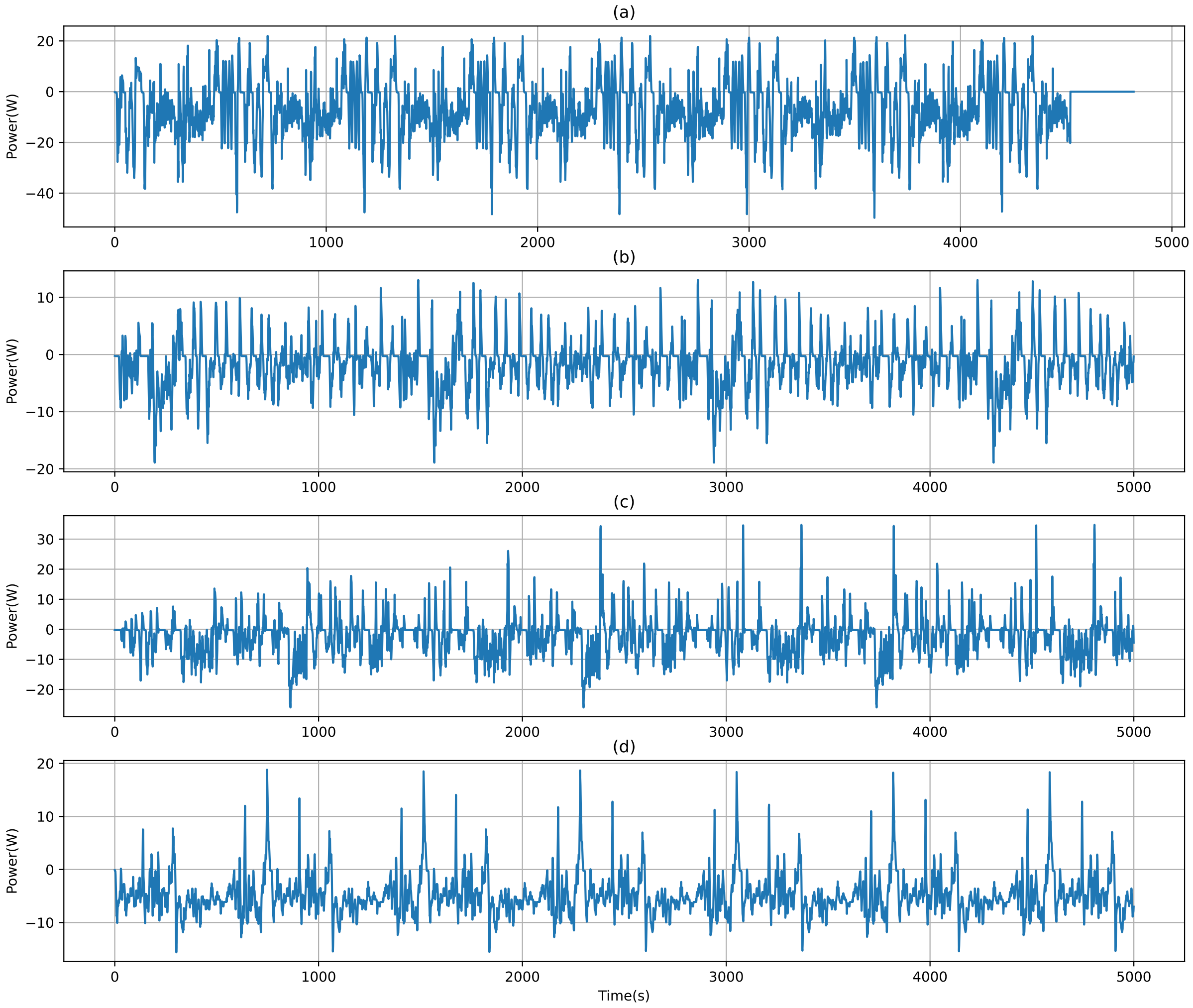

Figure 5.1: The drive cycle powers for a one cell of battery pack of Ford F150 for (a) US06, (b) UDDS,(c) LA92, (d) HWFT profiles used for the training and testing phases at $25°C$

Figure 5.2: The (a) Current, (b) Voltage, (c) Capacity of battery for train drive cycle at $25°C$, $10°C$ and $0°C$ ambient temperature

5.3 State Of Charge Estimation By BiLSTM method

For train datesets of Panasonic NCR18650PF cells, up to eight drive cycle sequences in three distinct ambient temperatures ($25°C$, $10°C$, $0°C$) are combined. For the validation dataset, a drive cycle created by a random mix of US06, HWFET, USDDE, and LA92 drive cycles is utilized. Since the sampling frequency was set to 1Hz, the length of each sequences was approximately among 4000 and 10,000 time-steps, resulting in a training dataset with more than 100,000 time-steps. It is not feasible to implement a network with a time-steps equal to this length sequence. Hence, the dataset is split to shorter sequences. In this work, the different time-steps between 500 to 10,000 were tested.

The results of SOC estimation by BiLSTM models are described in this section. As mentioned in the previous chapter, The input vector is identified as $\mathbf{x}_t = \{V(t), I(t), T(t)\}$, where $V(t), I(t), T(t)$ are the voltage, current and temperature of the battery at time t, respectively. Furthermore, the proposed model structure is explained in Section 4.3, and the Adam optimization method is used for learning the system. To evaluate the effect of the number of hidden units (N_n), and number of hidden layers (L) on the estimated performance, BiLSTM was developed with different hidden layers and hidden units. The times-step is set to $10,000$, and the learning rate is chosen at 10^{-4}. Additionally, to overcome the over-fitting, Early stopping method is used. With Early stopping, the training process stops while the validation loss begins to increase after several iterations. To achieve accurate estimation, each suggested network is learned 10 times. The MAE, MAX, and RMSE performances reported here is obtained from the average results of ten training. Figure 5.3 compares the estimation accuracy for $N_n = \{128, 256, 512, 1024\}$ at $25°C$ ambient temperature. When N_n increases to 512, the MAE and RMSE decrease to 0.60 and 1.02 at $25°C$, respectively. However, an overgrowth of N_n can cause overfitting and reduce the accuracy of SOC estimation. This effect is visible in the MAE and RMSE values reached by $N_n = 1024$. These results are presented in more detail in the Table 5.2 at $25°C$ and $0°C$. As can be seen, the best performance is reached by $N_n = 512$. Also, the validation loss function for $N_n = \{128, 512\}$ at $25°C$ ambient temperature are shown in figure 5.4. It is clear that larger number of N_n makes system converge faster to good performance.

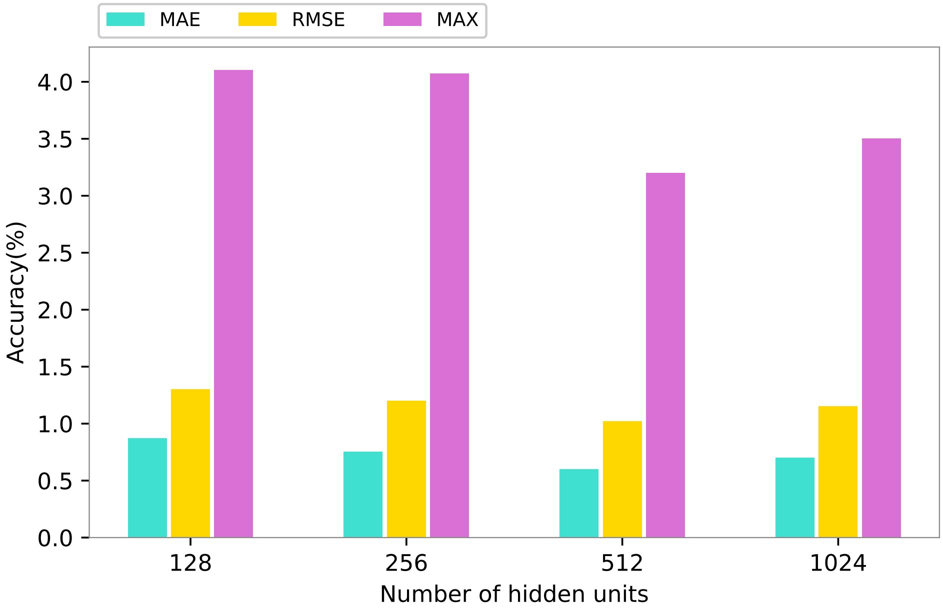

Figure 5.3: Comparison of SOC estimation performances regarding to number of hidden units at 25°C ambient temperature.

Table 5.2: SOC estimation accuracy by BiLSTM methods with different number of hidden units.

Number of hidden units	Test case evaluation	Temperature (°C)	
		25	**0**
128	MAE(%)	0.87	1.31
	MAX(%)	4.1	4.9
	RMSE(%)	1.3	1.54
256	MAE(%)	0.75	1.10
	MAX(%)	4.07	4.3
	RMSE(%)	1.20	1.23
512	**MAE(%)**	**0.60**	**0.81**
	MAX(%)	**3.2**	**4.01**
	RMSE(%)	**1.02**	**1.08**
1024	MAE(%)	0.7	0.94
	MAX(%)	3.5	5.02
	RMSE(%)	1.15	1.35

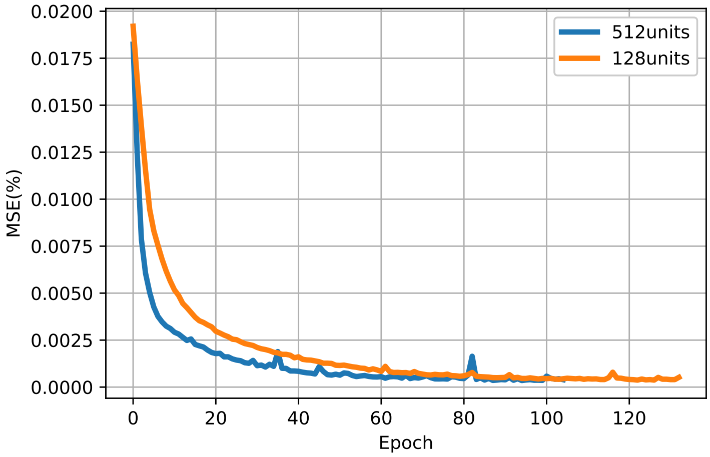

Figure 5.4: Validation loss function for network with 512 hidden units and 128 hidden units.

Figure 5.5 and figure 5.6 depict the SOC estimation and the SOC error, which is defined as the difference between the SOC measurement and the SOC estimation, for network with $N_n = 512$ at $0°C$ and $25°C$ ambient temperature, respectively.

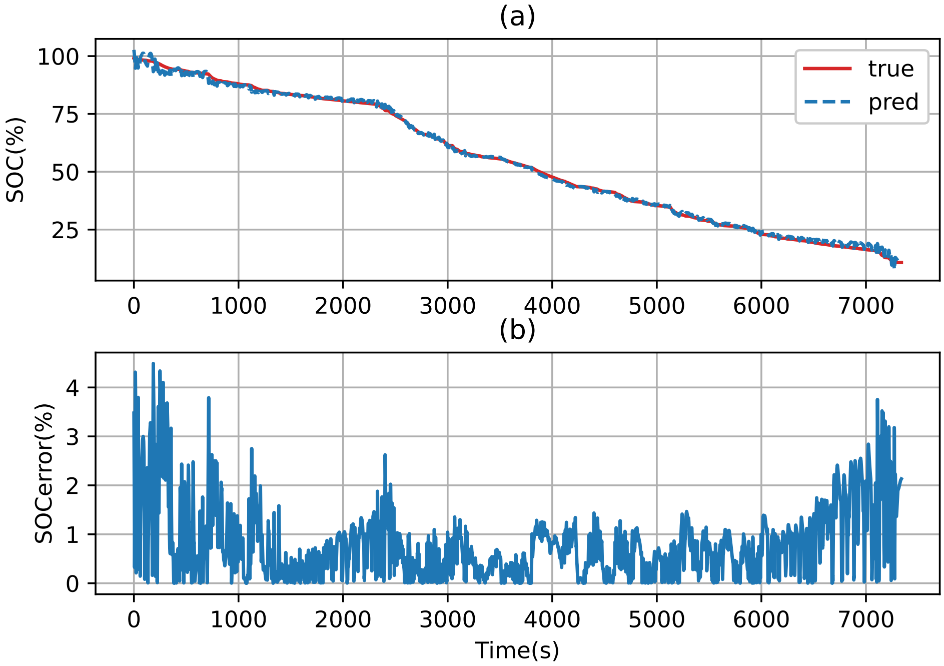

Figure 5.5: (a) SOC estimation and (b) error estimation by BiLSTM network with 512 hidden units for a drive cycle mix of US06, HWFET, USDDE and LA92 at $0°C$.

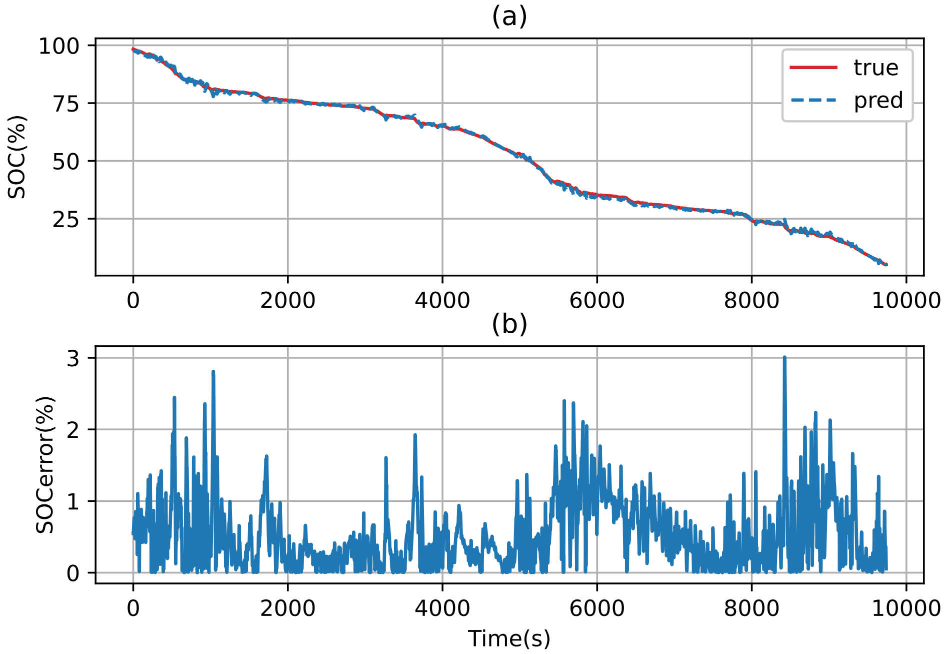

Figure 5.6: (a) SOC estimation and (b) error estimation by BiLSTM network with 512 hidden units for a drive cycle mix of US06, HWFET, USDDE and LA92 at 25°C.

Table 5.3: SOC estimation accuracy by BiLSTM methods with two hidden layers.

Number of hidden layers	Test case evaluation	Temperature (°C)	
		25	**0**
256-16	MAE(%)	0.76	1.13
	MAX(%)	3.8	4.15
	RMSE(%)	1.14	1.6
256-32	**MAE(%)**	**0.43**	**0.7**
	MAX(%)	**1.8**	**2.3**
	RMSE(%)	**0.75**	**0.92**
512-32	MAE(%)	0.83	0.92
	MAX(%)	2.06	4.3
	RMSE(%)	1.05	1.2

The network performance increases by creating a network with consecutive layers. Therefore, a network with a large number of hidden units can be replaced with a multi-layer network with fewer units per layer. According to the results in Table 5.3, it is apparent that the highest estimation performance is achieved by the two hidden layers model with 256 BiLSTM units in first layer and 32 LSTM units in second layers. The

RMSE and MAX error for the two hidden layers network is 0.75 and 1.8 at 25°C, respectively, while these values are equal to 1.02 and 3.2 for the best network with one hidden layer under the same condition.

Figures 5.7 and 5.8 demonstrate the SOC estimation result as well as the SOC error of BiLSTM with two layers at 0°C and 25°C, respectively.

The above results indicate that BiLSTM algorithm behaves well at fixed ambient temperatures. But, in reality, the ambient temperature may be changed. Hence, to assess the SOC estimation performance the algorithm (256-32) was applied to a test case dataset consisting of different ambient temperatures within 10°C to 25°C. The MAE is 0.77 and the RMSE is equal to 0.96. These results reveal that the proposed algorithm has a good ability to estimate SOC at ambient temperature. The performance of the BiLSTM model at varying ambient temperatures is depicted in figure 5.9.

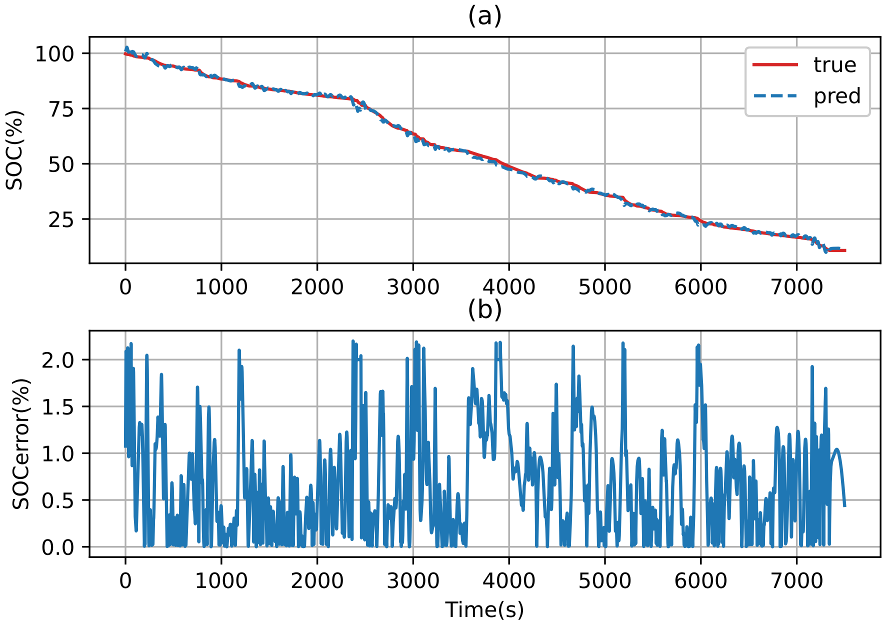

Figure 5.7: (a) SOC estimation and (b) error estimation for a drive cycle mix of US06, HWFET, USDDE and LA92 at 0°C by BiLSTM network with 2 hidden layers, the 256 BiLSTM units are in the first layer and 32 LSTM units are in the second layer.

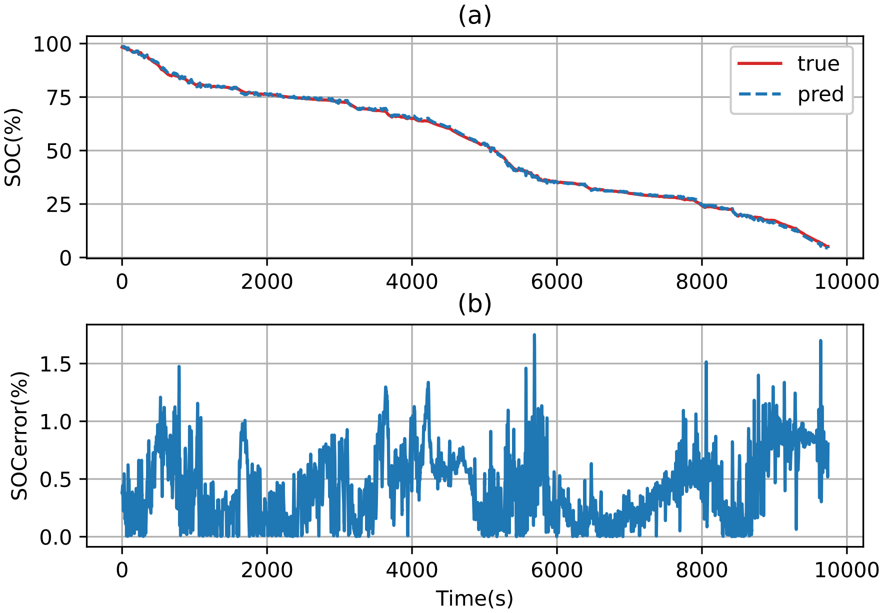

Figure 5.8: (a) SOC estimation and (b) error estimation for a drive cycle mix of US06, HWFET, USDDE and LA92 at 25°C by BiLSTM network with 2 hidden layers, the 256 BiLSTM units are in the first layer and 32 LSTM units are in the second layer.

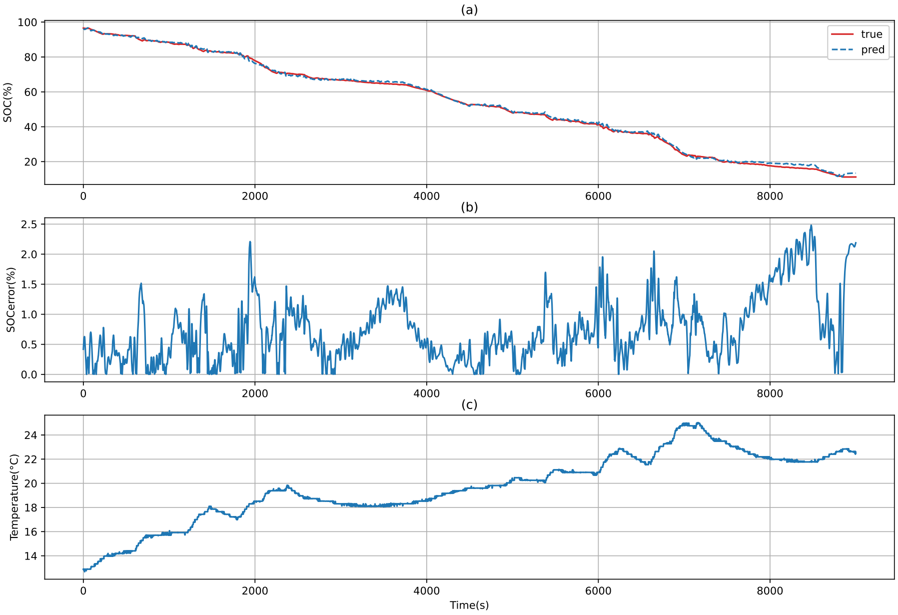

Figure 5.9: (a) SOC estimation and (b) error estimation for a drive cycle mix of US06, HWFET, USDDE and LA92 at varying temperature by BiLSTM network with 2 hidden layers, the 256 BiLSTM units are in the first layer and 32 LSTM units are in the second layer. Temperature is shown in (c).

Since one of the main challenges in estimating SOC is finding the exact initial value of SOC, the methods independent of the initial value are considered. To test the system with an incorrect initial value, h_0 is set to zero. Figure 5.10 shows the 40% error at the start of the cycle. However, this value decreases rapidly, and the SOC estimate reaches the desired value after approximately 10 seconds.

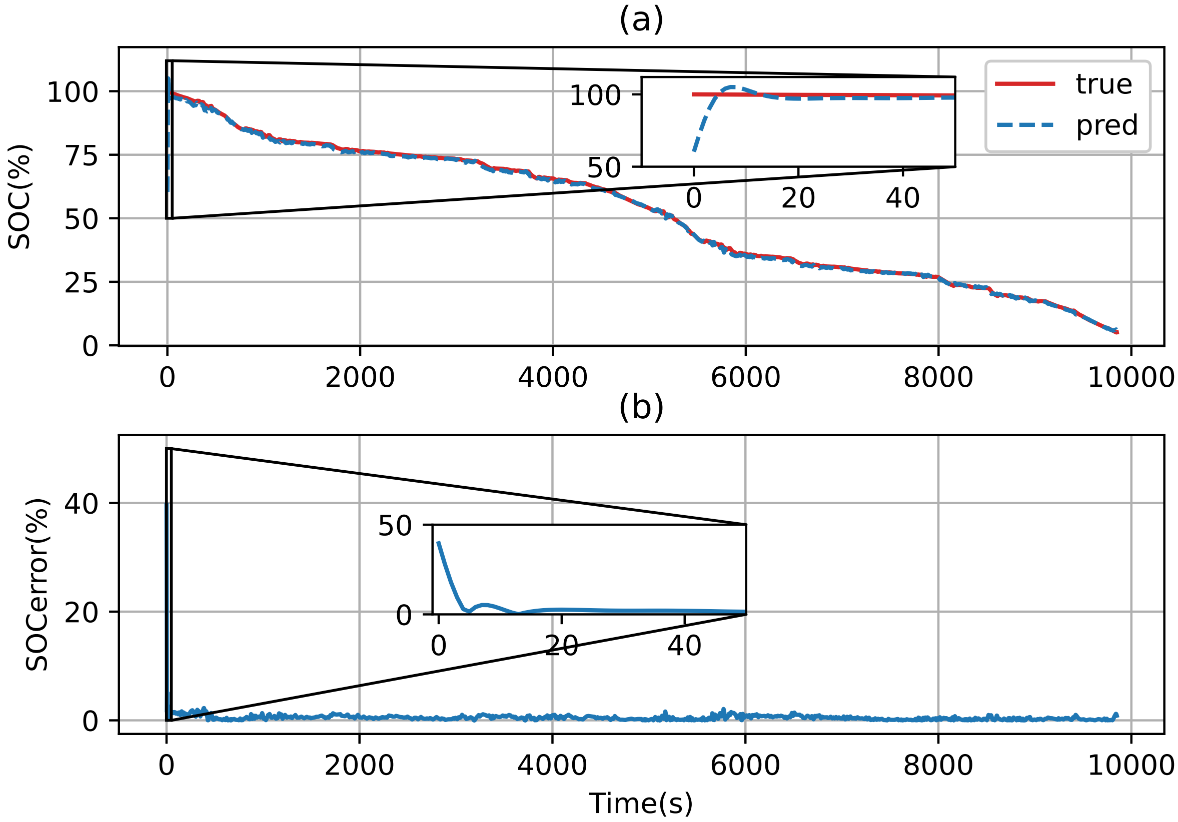

Figure 5.10: (a) SOC estimation and (b) error estimation for a drive cycle mix of US06, HWFET, USDDE and LA92 at 25°C by BiLSTM network with 2 hidden layers, the 256 BiLSTM units are in the first layer and 32 LSTM units are in the second layer and $h_0 = 0$.

5.4 Experimental result of SOC Estimation By RoLSTM Algorithm

In this section, the experimental results of SOC estimation obtained with the model explained in section 4.4. Also, the optimization algorithm used for training the system is Roadam, with an initial learning rate equal to 0.0005. The number of units and layers are chosen by trial and error. $k = 128$ and $l = 8$ are the number of units of the first layer and the second layer for each input, respectively. RoAdam can be adaptively tuned against an outlier. The weights and biases could be tuned online with a strategy of adaptive optimization to have a high-performance network. The train and test datasets are chosen as in the previous section. Here, the time-step is 1000. If raw data is used for output data, RoAdam helps us to have smoother estimation by decreasing the effect of outliers. RoAdam is a useful optimization algorithm in real time data against unwanted noise and disturbance. However, in our results, in comparison with the Adam algorithm, the performance improvement was not significant because there was no noticeable outlier in the used datasets. In RoLSTM, the $MAE = 0.54$ and the $RMSE = 0.79$ at $25°C$, whereas these values with the LSTM-Adam algorithm are 0.76 and 0.98, respectively. The results obtained from the average SOC estimation after ten times of training are summarized in Table 5.4.

Table 5.4: compare SOC estimation accuracy by RoLSTM method and LSTM-Adam algorithm .

LSTM Algorithm	Test case evaluation	Temperature (°C)	
		25	**0**
RoLSTM	**MAE(%)**	**0.54**	**0.7**
	MAX(%)	**1.9**	**2.56**
	RMSE(%)	**0.79**	**1.02**
LSTM-Adam	MAE(%)	0.76	0.98
	MAX(%)	2.98	3.6
	RMSE(%)	0.97	1.12

The SOC estimation by RoLSTM algorithm at $0°C$ and $25°C$ are illustrated in Fig. 5.11 and Fig. 5.12, respectively. As well as, like BiLSTM model, this algorithm was evaluated by a drive cycle test at varying ambient temperatures. The $MAE = 1.03$ and $RMSE = 1.78$ indicate the RoLSTM performance is good at variable temperature. Fig. 5.13 shows the performance of RoLSTM model at varying ambient temperature.

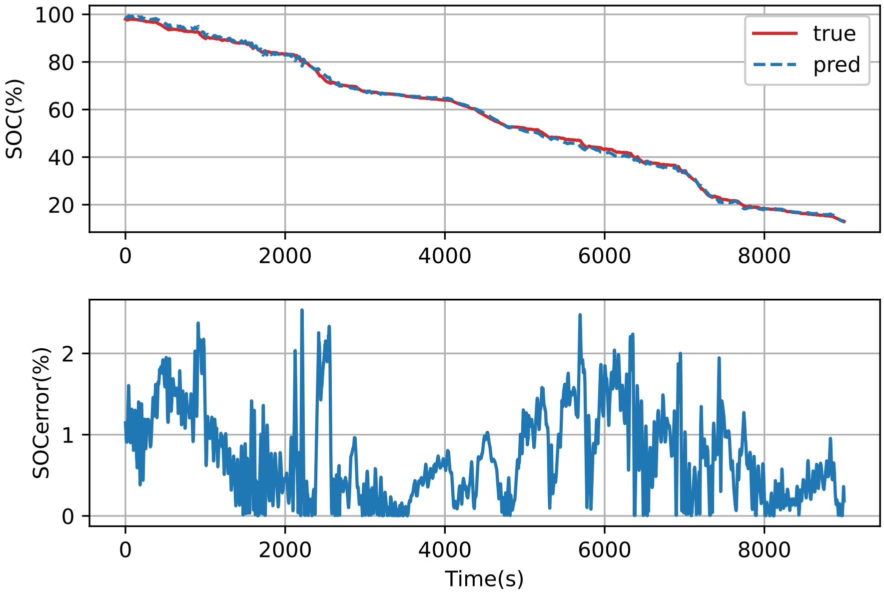

Figure 5.11: (a) SOC estimation and (b) error estimation for a drive cycle mix of US06, HWFET, USDDE and LA92 at 0°C by RoLSTM network with 2 hidden layers, the 128 LSTM units are in the first layer and 8 LSTM units are in the second layer for each input.

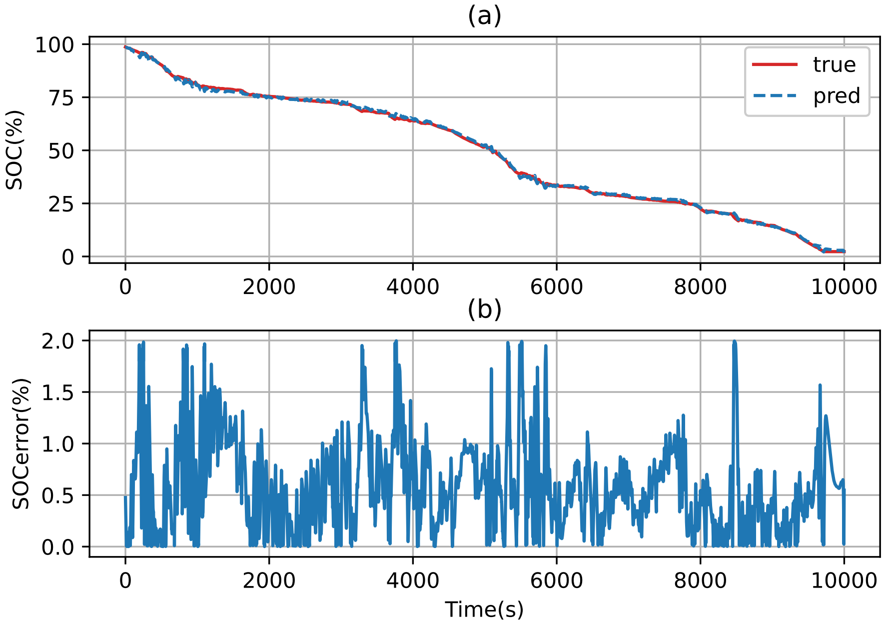

Figure 5.12: (a) SOC estimation and (b) error estimation for a drive cycle mix of US06, HWFET, USDDE and LA92 at 25°C by RoLSTM network with 2 hidden layers, the 128 LSTM units are in the first layer and 8 LSTM units are in the second layer for each input.

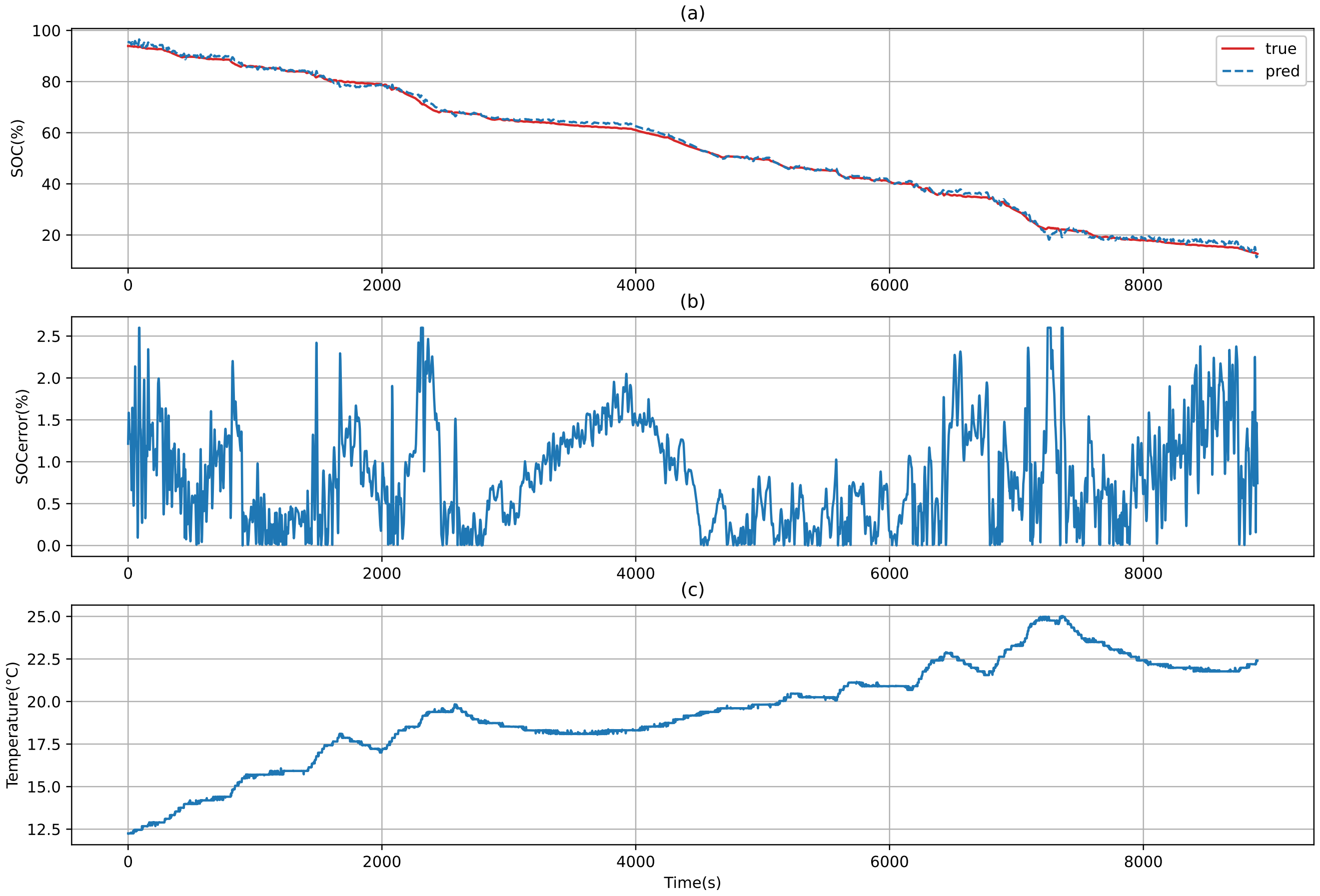

Figure 5.13: (a) SOC estimation and (b) error estimation for a drive cycle mix of US06, HWFET, USDDE and LA92 at varying temperature by RoLSTM network with 2 hidden layers, the 128 LSTM units are in the first layer and 8 LSTM units are in the second layer for each input. Temperature is shown in (c).

5.5 GRU Algorithm used for SOC Estimation

Here, the SOC estimate is achieved using the Gated Recurrent Units algorithm, as explained in section 4.5. The number of hidden layers and units discovered through trial and error is equal to two layers with 512 and 32 units respectively. The Adam optimization algorithm with a learning rate= 10^{-4} is utilized to adjust the weights and biases of the network. As described in section 5.3 all datasets are re-sampled at $1Hz$ sampling frequency. Also, the time-step is chosen as 1000. The average of ten times of training yields MAE, RMSE, and MAX errors of 0.93, 1.1, 4.4 at $0°C$, and 0.84, 1.09, 4.2 at $25°C$, respectively. Moreover, the MAE =1.2, RMSE= 2.04, and MAX= 5.01 at varying ambient temperature. The figures 5.14, 5.15, and 5.16 depict the GRU's performance at $0°C$, $25°C$ and varying ambient temperature.

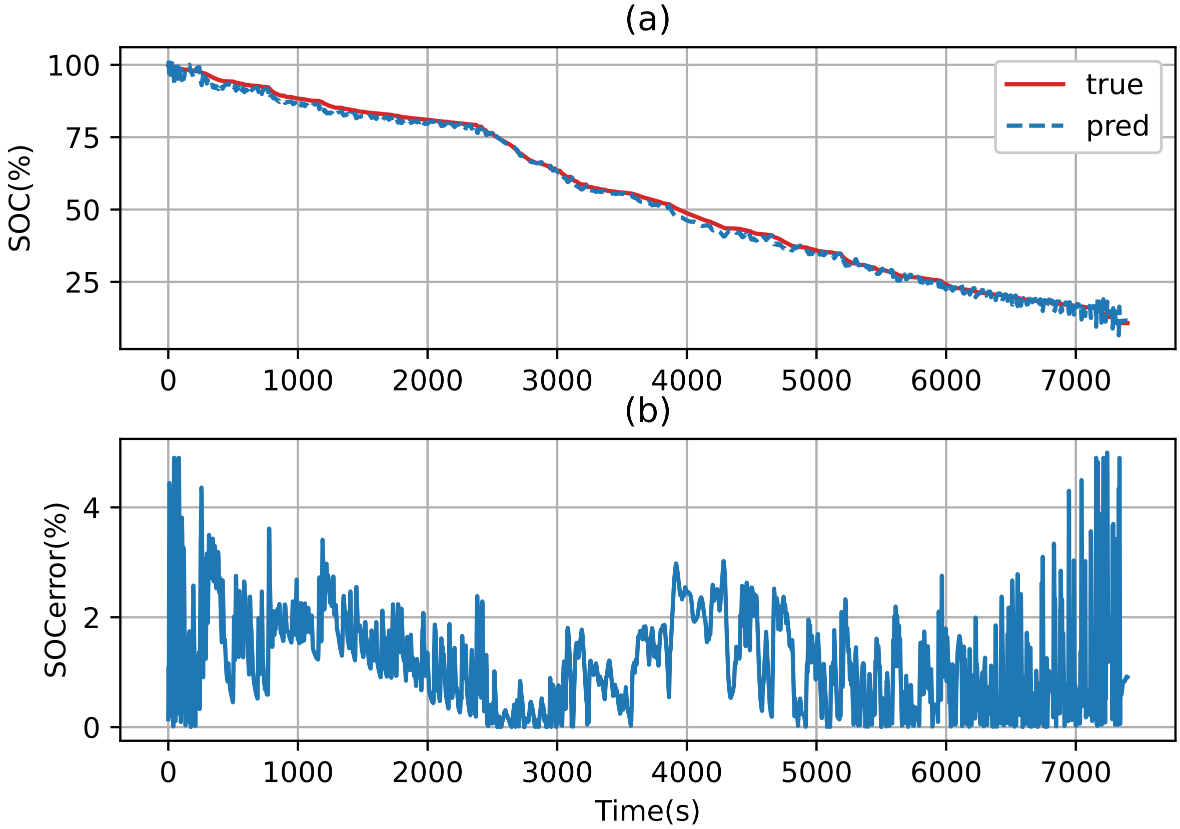

Figure 5.14: (a) SOC estimation and (b) error estimation for a drive cycle mix of US06, HWFET, USDDE and LA92 at $0°C$ by GRU network with 2 hidden layers, the 512 GRU units are in the first layer and 32 GRU units are in the second layer.

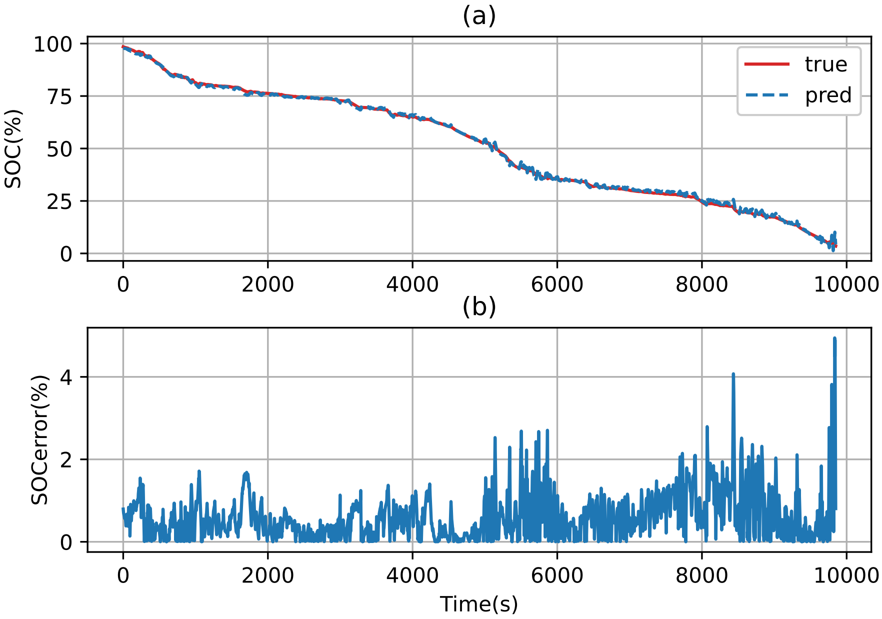

Figure 5.15: (a) SOC estimation and (b) error estimation for a drive cycle mix of US06, HWFET, USDDE and LA92 at 25°C by GRU network with 2 hidden layers, the 512 GRU units are in the first layer and 32 GRU units are in the second layer.

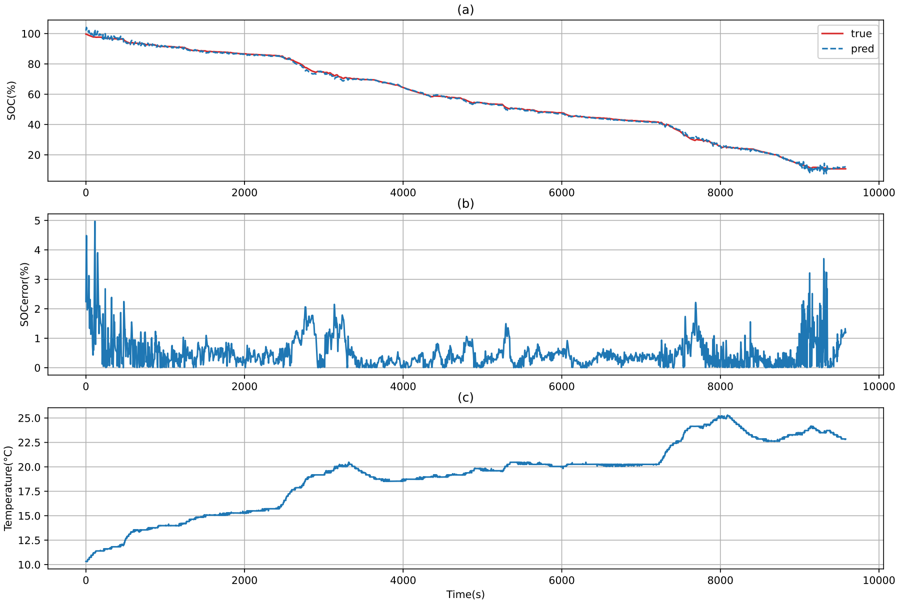

Figure 5.16: (a) SOC estimation and (b) error estimation for a drive cycle mix of US06, HWFET, USDDE and LA92 at varying temperature by GRU network with 2 hidden layers, the 512 GRU units are in the first layer and 32 GRU units are in the second layer. Temperature is shown in (c).

5.6 Discussion

In this chapter, the results of SOC estimation using three deep RNNs models in a single cell battery are investigated. In summary, a comparison of the results in this chapter with those of other studies is listed in Table 5.5.

Table 5.5: Comparison of SOC estimation accuracy in recent studies.

Methods	Error	Temperature	Li-ion Type
AUKF with LSSVM [123]	$MAE < 2\%$	$25°C \sim 42°C$	$70Ah$ Kokam
FNN [124]	$MAE < 4.04\%$	$0°C \sim 40°C$	LG18650HG2
LSTM-RNN [39]	$MAE < 1.6\%$	$0°C \sim 25°C$	Panasonic 18650PF
FO-AEKF [125]	$MAE < 1.59\%$	———	Li[NiCoAl]O2(NCA)
BiLSTM	$MAE < 0.77\%$	$0°C \sim 25°C$	Panasonic 18650PF
RoLSTM	$MAE < 1.03\%$	$0°C \sim 25°C$	Panasonic 18650PF
GRU	$MAE < 1.2\%$	$0°C \sim 25°C$	Panasonic 18650PF

As can be seen from the comparison of the results, the BiLSTM network was demonstrated greater performance than the other algorithms. With this model, it is possible to analyze longer sequences from two directions (the past and the future) without the gradient vanishing happening. In this feature, one could get more accurate estimates of discharge period duration, due to the ability to choose the length of discharge period as long as a drive cycle's time. Moreover, BiLSTM estimator performed well when presented with an incorrect SOC initial value.

6

REAL TIME STATE OF CHARGE ESTIMATION FOR ELECTRIC VEHICLE

Contents

6.1 Introduction

The battery pack, which serves as the primary source of energy in EVs, is made up of many cells that are linked in series and parallel. Since knowing the status of charge of the pack is essential for the driver, investigating the SOC estimate of the battery-pack in EVs is of great interest. A large number of published studies describe the techniques of SOC estimation for a single cell. However, in [126], Plett introduced a "Bar-Delta" filtering method based on Kalman Filter to estimate the SOC in battery-pack. Mawonou et *al.* improved the accuracy of the Bar-Delta estimator by "switched bar-delta" algorithm [127]. Additionally, in [128, 129] the authors are proposed the AEKF based approach. Machine learning methods for estimating SOC in EVs battery packs are presented in [130, 25] to reduce computational complexity.

Finding an estimator which can reduce the complexity of computing tasks while still working in real time with sufficient accuracy is a critical issue in electric vehicle development. In order to achieve the aforementioned objectives, This chapter presents a new BiLSTM method for estimating the SOC of a pack of batteries in EVs. To collect data and evaluate the model in the simulation, IPG Carmaker software was utilized.

6.2 CarMaker Environment

CarMaker is a virtual software introduced by the company IPG Automotive for simulation of real-time driving tests during the complete development process (Model-In-Loop, Software-In-Loop, Hardware-In-Loop, and Vehicle-In-Loop). Real test scenarios can be created by CarMaker in a virtual environment by simulating different types of roads, traffic, weather conditions, and maneuvering conditions. Additionally, CarMaker also includes an intelligent driver model with the ability to specify driving behaviors, as well as a comprehensive vehicle model that includes tires, chassis, powertrain, and controllers[131].

The main Graphical User Interface (GUI) of CarMaker which acts as a software's control center is shown in Figure 6.1.

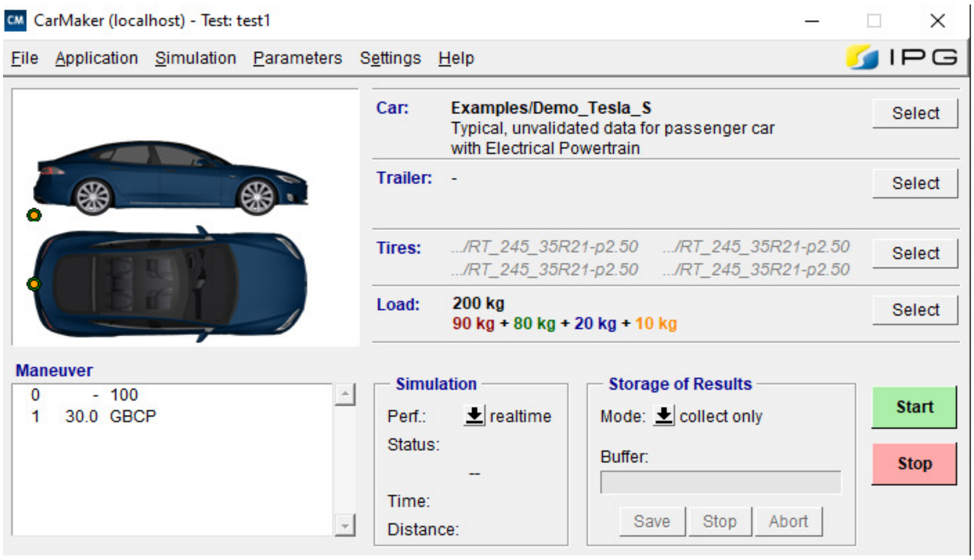

CarMaker (localhost) - Test: test1

Car: Examples/Demo_Tesla_S
Typical, unvalidated data for passenger car
with Electrical Powertrain

Trailer: -

Tires: .../RT_245_35R21-p2.50 .../RT_245_35R21-p2.50
.../RT_245_35R21-p2.50 .../RT_245_35R21-p2.50

Load: 200 kg
90 kg + 80 kg + 20 kg + 10 kg

Maneuver
0 - 100
1 30.0 GBCP

Simulation
Perf.: realtime
Status: --
Time:
Distance:

Storage of Results
Mode: collect only
Buffer:

Figure 6.1: IPG CarMaker main GUI

The essential tools in CarMakers are:

- IPGMovie: a real-time 3D animation of the vehicle that shows the desired maneuvers on the determined road (Figure 6.2).

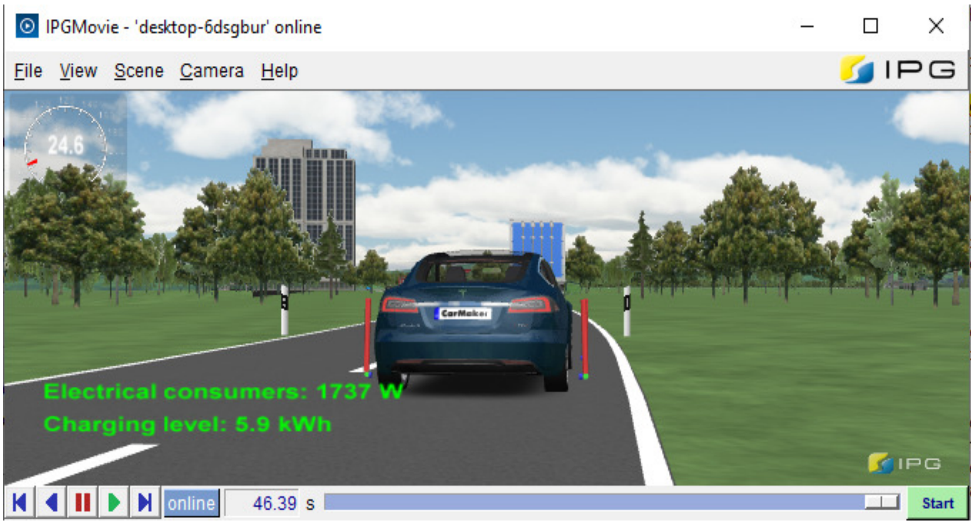

IPGMovie - 'desktop-6dsgbur' online

Electrical consumers: 1737 W
Charging level: 5.9 kWh

online 46.39 s

Figure 6.2: IPGMovie window

- Instruments: displays important instruments and driving conditions information such as the ABS warning lamp, pedal position, and so on (Figure 6.3).

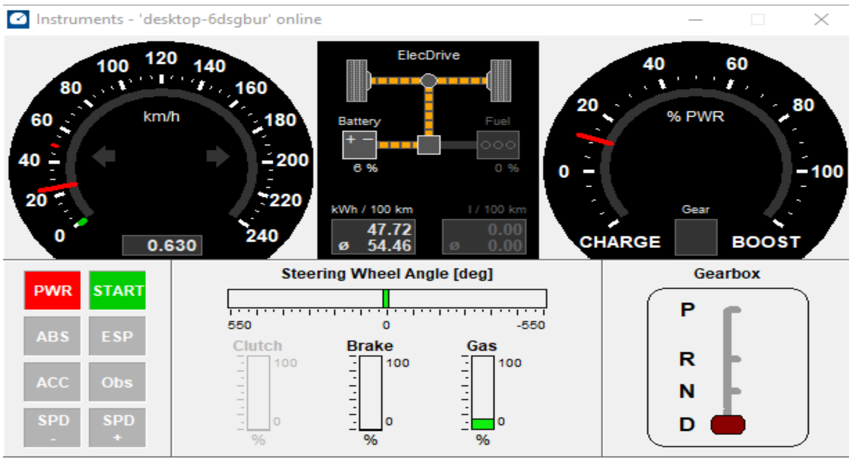

Figure 6.3: Instruments window

- IPGControl: it can manage the result in real-time by monitoring, displaying, and exporting the data (Figure 6.4)

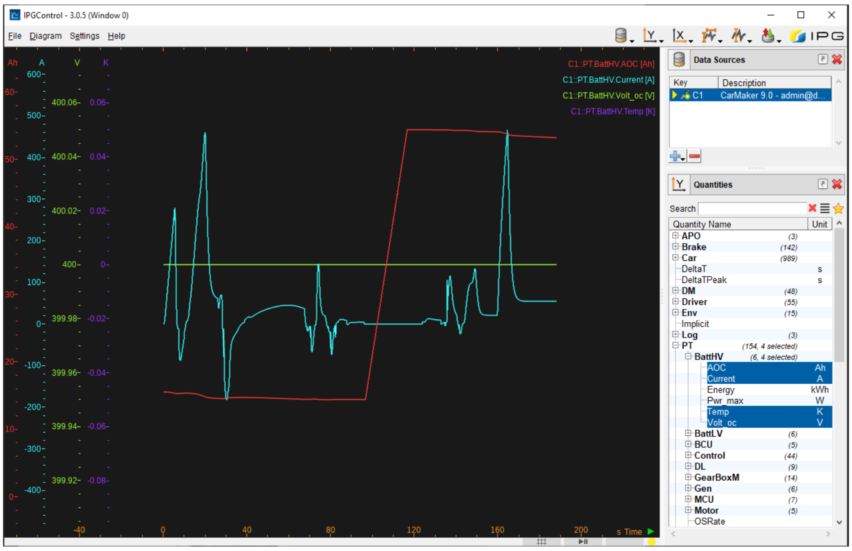

Key	Description
C1	CarMaker 9.0 - admin@d...

Quantity Name		Unit
APO	(3)	
Brake	(142)	
Car	(989)	
DeltaT		s
DeltaTPeak		s
DM	(48)	
Driver	(55)	
Env	(15)	
Implicit		
Log	(3)	
PT	(154, 4 selected)	
BattHV	(6, 4 selected)	
AOC		Ah
Current		A
Energy		kWh
Pwr_max		W
Temp		K
Volt_oc		V
BattLV	(6)	
BCU	(5)	
Control	(44)	
DL	(9)	
GearBoxM	(14)	
Gen	(6)	
MCU	(7)	
Motor	(5)	
OSRate		

Figure 6.4: IPGControl window

- Direct Variable Access: allows for the observation and modification of simulation variables throughout the simulation (Figure 6.5).

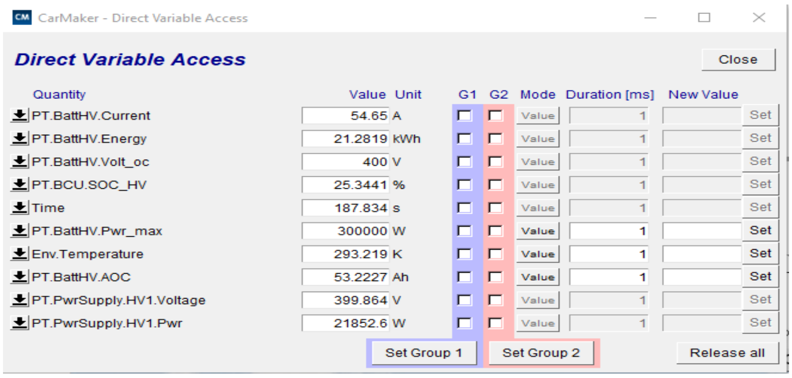

Quantity	Value	Unit	G1	G2	Mode	Duration [ms]	New Value	
PT.BattHV.Current	54.65	A	☐	☐	Value	1		Set
PT.BattHV.Energy	21.2819	kWh	☐	☐	Value	1		Set
PT.BattHV.Volt_oc	400	V	☐	☐	Value	1		Set
PT.BCU.SOC_HV	25.3441	%	☐	☐	Value	1		Set
Time	187.834	s	☐	☐	Value	1		Set
PT.BattHV.Pwr_max	300000	W	☐	☐	Value	1		Set
Env.Temperature	293.219	K	☐	☐	Value	1		Set
PT.BattHV.AOC	53.2227	Ah	☐	☐	Value	1		Set
PT.PwrSupply.HV1.Voltage	399.864	V	☐	☐	Value	1		Set
PT.PwrSupply.HV1.Pwr	21852.6	W	☐	☐	Value	1		Set

Figure 6.5: Direct Variable Access window

6.3 Creating a simulation for estimate the SOC in EVs

Having an accurate SOC estimation depends on various conditions, including road information, driver behavior, maneuver strategy, and climate conditions. Behavioral and environmental effects on energy consumption in EVs were assessed by Vincent *et al.* [132]. To create a simulation with Carmaker for collecting the train and test data for SOC estimation with considering all factors, the following steps are performed:

1. Choose the vehicle with all properties
2. The desired road
3. Select the driver behaviors
4. The maneuver status
5. Environment condition

6.3.1 Vehicle Model

In this project, the demo of `Tesla-S` vehicle model from the library of Carmaker has been chosen. In this model, the vehicle body was defined as a flexible body for simulation of the bending and torsion of the body. The specifications of the vehicle body are listed in Table 6.1. The battery system of the Tesla-S contains 16 modules. As can be seen in figure 6.6 each module includes 444 battery cells, which are wired in 74 cells in parallel and 6 groups in series. The battery cells used in the modules are Panasonic NCR18650BE models with 3200mAh and 3.6 V nominal capacity and voltage, respectively.

Table 6.1: The overall specification of the desired body vehicle.

Vehicle overall mass [kg]	2108		
Vehicle overall center of gravity x / y / z [m]	2.580	0.000	0.545
Vehicle overall inertia tensor x / y / z [kgm²]	952.229	3519.035	3954.288
Axle load front / rear [kg]	1064.646	1043.354	
Wheel base [m]	2.970		

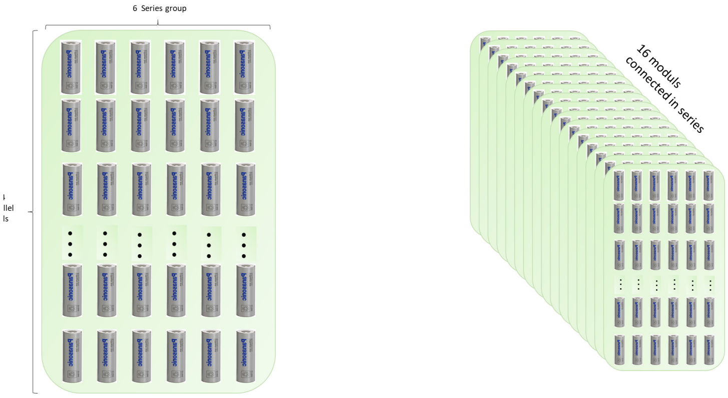

Figure 6.6: The battery system of `Tesla-S`. The right figure is a module of batteries which is contain 74P6S battery. The capacity of each module is $74 \times 3.2Ah = 23.7Ah$ and the voltage is $6 \times 3.6V = 21.6V$. The left figure is the `Tesla-S` powertrain system containing 6 modules wiring in series.

Figures 6.7 and 6.8 display a 3D view of the powertrain system and basic information regarding the powertrain of the demo `Tesla-S`, respectively. The rear drive is selected as the drive-line in the powertrain dataset. In the rear-drive model, the differential output shafts are connected to the rear wheels. The power supply is defined by two levels of voltage: high voltage (HV) and low voltage (LV). The idle voltage of HV is 400v. The capacity and power of the battery are 210 Ah and 85Kw, respectively. Figure 6.9 represents the specification of HV Battery. In This thesis the data are collected with different initial state of Charge.

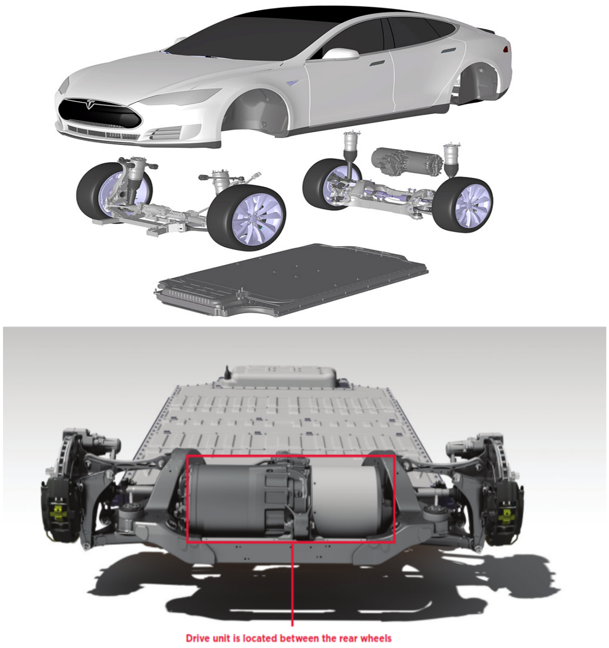

Figure 6.7: 3D view of powertrian system in `Tesla-S`. The drive units is located between the rear wheel [5, 6]

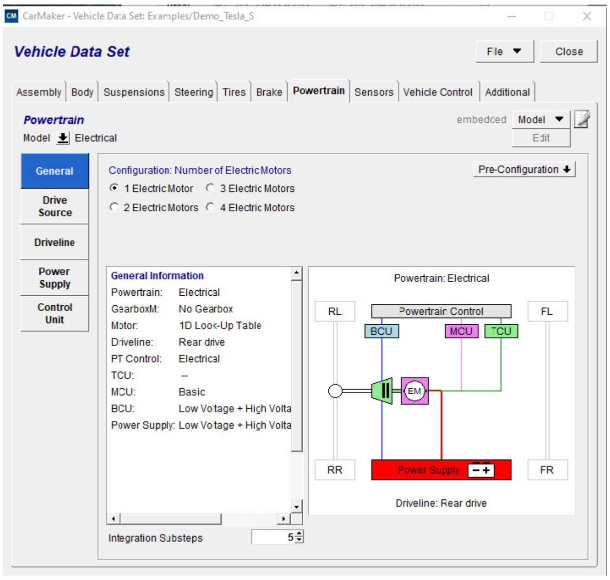
CarMaker - Vehicle Data Set: Examples/Demo_Tesla_S

Vehicle Data Set

Powertrain

Model Electrical

Configuration: Number of Electric Motors

● 1 Electric Motor ○ 3 Electric Motors
○ 2 Electric Motors ○ 4 Electric Motors

General Information

Powertrain: Electrical
GearboxM: No Gearbox
Motor: 1D Look-Up Table
Driveline: Rear drive
PT Control: Electrical
TCU: --
MCU: Basic
BCU: Low Voltage + High Volta
Power Supply: Low Voltage + High Volta

Integration Substeps 5

Figure 6.8: Powertrain configuration of `Tesla-S`

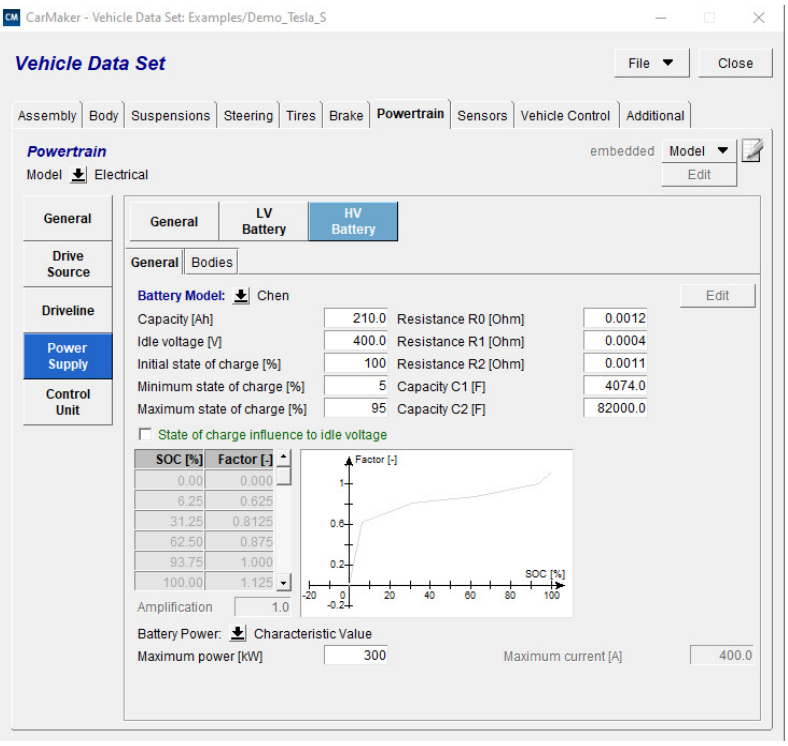

Model: Electrical

Battery Model: Chen

Capacity [Ah]: 210.0

Idle voltage [V]: 400.0

Initial state of charge [%]: 100

Minimum state of charge [%]: 5

Maximum state of charge [%]: 95

Resistance R0 [Ohm]: 0.0012

Resistance R1 [Ohm]: 0.0004

Resistance R2 [Ohm]: 0.0011

Capacity C1 [F]: 4074.0

Capacity C2 [F]: 82000.0

☐ State of charge influence to idle voltage

SOC [%]	Factor [-]
0.00	0.000
6.25	0.625
31.25	0.8125
62.50	0.875
93.75	1.000
100.00	1.125

Amplification: 1.0

Battery Power: Characteristic Value

Maximum power [kW]: 300

Maximum current [A]: 400.0

Figure 6.9: Specification of HV Battery

6.3.2 3D Road Profile Generation

The next step in simulation with Carmaker is creating the road. In powertrain tests, the road plays an important role, in fact, the use of real routes provides more traceability of the system via real conditions.

The important parameters in the road model to produce optimal conditions in the Carmaker are as follows:

- X and Y direction coordinates: like straight sections and road curvature.
- Gradient: the road slope is an essential parameter in changing the influential forces on vehicles.
- Speed limits: defined as the maximum speed allowed for the driver according to legal standards.
- Road characteristic: such as track width, traffic light, speed bump et *etc.*

Two ways to generate the 3D road profile are described below:

6.3.2.1 Using Google Maps

Google Maps is a free internet-based software applied for navigation. The data collected by Google Maps can be saved in a file including just X-Y coordinates. Since the altitude of the road plays an important role in EV's energy consumption, the data generated from Google Maps is not enough efficient for real-time testing. To overcome this problem, an online service named GPSVisualizer is applied. GPSVisualizer refines GPS coordinates taken from Google Maps by adding altitude parameters. The GPSVisulizer output file can be exported directly to IPGCarmaker Figure 6.10 shows the sample route in Google Maps.

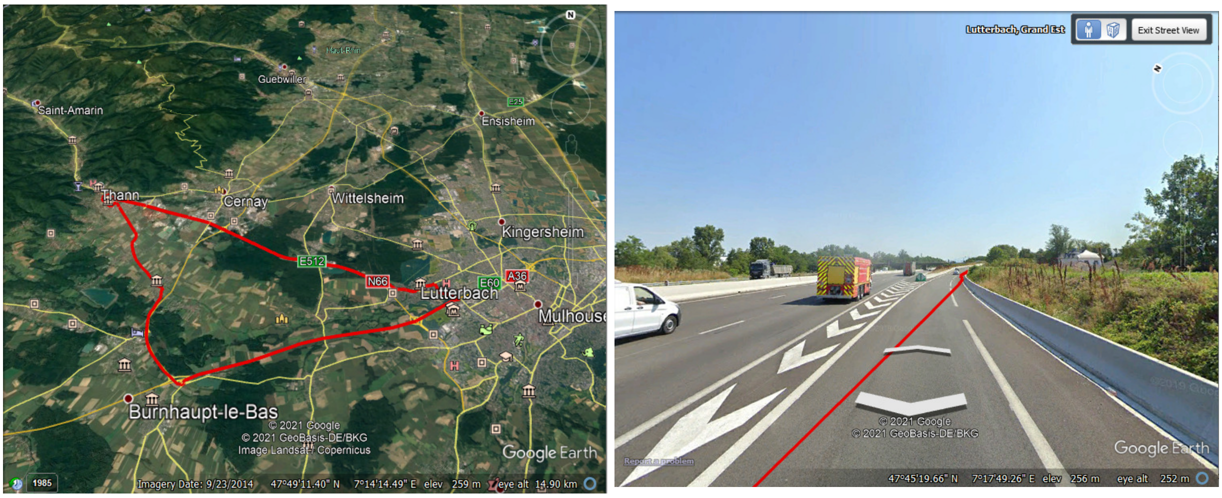

(a) (b)

Figure 6.10: Sample route in Google Earth

6.3.2.2 RoutConverter Software

RouteConverter is a free open source software applied for display and edit GPS data. Moreover, this software is able to convert tracks, routes, and way-points to each others. Figure 6.11 shows the software environment. In Figure 6.11 part (A) illustrates the Google traffic online Maps, part (B) describes the Position list, and part (C) depicts the rout elevation. Since the generated 3D route and way-points can be edited by RoutConverter, the output file is more suitable for using in IPGCarmaker. In this thesis, Routconverter software was used for generate the 3D road.

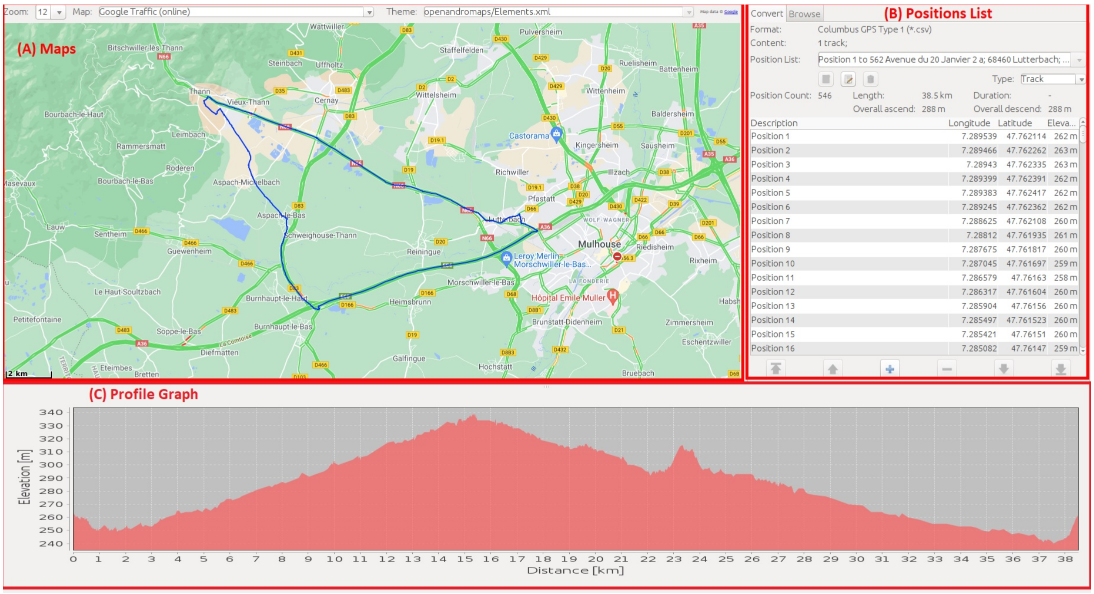

Zoom: 12
Map: Google Traffic (online)
Theme: openandromaps/Elements.xml

Format: Columbus GPS Type 1 (*.csv)
Content: 1 track;
Position List: Position 1 to 562 Avenue du 20 Janvier 2 a; 68460 Lutterbach; ...
Type: Track
Position Count: 546
Length: 38.5 km
Duration: -
Overall ascend: 288 m
Overall descend: 288 m

Description	Longitude	Latitude	Eleva...
Position 1	7.289539	47.762114	262 m
Position 2	7.289466	47.762262	263 m
Position 3	7.28943	47.762335	263 m
Position 4	7.289399	47.762391	262 m
Position 5	7.289383	47.762417	262 m
Position 6	7.289245	47.762362	262 m
Position 7	7.288625	47.762108	260 m
Position 8	7.28812	47.761935	261 m
Position 9	7.287675	47.761817	260 m
Position 10	7.287045	47.761697	259 m
Position 11	7.286579	47.76163	258 m
Position 12	7.286317	47.761604	260 m
Position 13	7.285904	47.76156	260 m
Position 14	7.285497	47.761523	260 m
Position 15	7.285421	47.76151	260 m
Position 16	7.285082	47.76147	259 m

Figure 6.11: The environment of RoutConverter software. Part (A) shows the Maps from Google traffic online model, Part (B) indicates the Position list of desired track, and Part (C) shows the rout elevation.

6.3.3 Driver Model

The driver behavior is a essential factor in modeling vehicle tensions during driving. Considering that each person performs a specific driving action, different models of driver aggressiveness are necessary for the development process. CarMaker allows us to simulate a model for controlling driver actions. The driver model utilized in this project is a model based on Proportional-integral-derivative (PID) controllers predefined in CarMaker. The acceleration diagrams for three types of drivers are illustrated in Figure 6.12. All longitudinal and lateral acceleration combinations are defined for the driver-friendly area within the red lines.

6.3.4 scenario Maneuver

applying Carmaker, a test scenario can be described for the driver. For example , increase the acceleration, driving at constant speed over a period of time or reduce speed and stop. Additionally, Carmaker allows us to definition a traffic scenario as in reality.

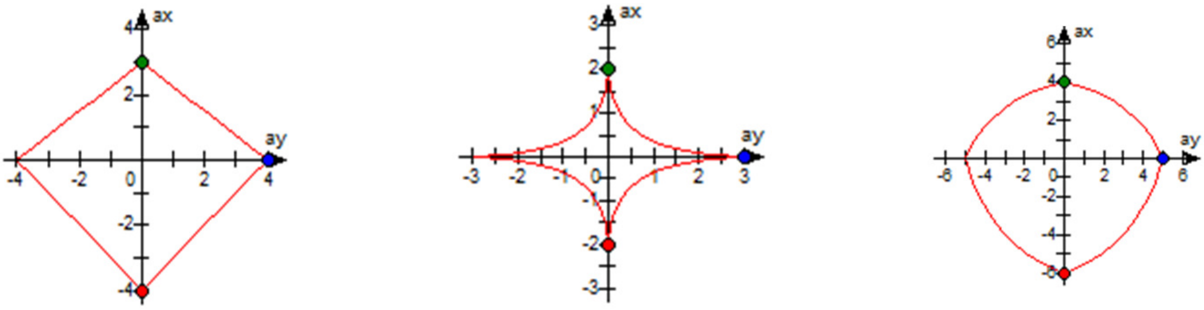

(a) (b) (c)

Figure 6.12: Acceleration diagram for three driver behavior. Diagram (a) shows the Normal driver, diagram (b) is for defensive driver and diagram (C) illustrates the aggressive driver

6.3.5 Environment Conditions

As said before, the environmental conditions play an important role to Evs energy consumption. Defining environmental factors like the temperature, and the daytime are possible with the environment module in IPGCarmaker. In this research, the effect of temperature variations on the state of charge of the battery is considered by performing simulations at different ambient temperature.

6.4 Developed State of Charge Estimation Method

In this section, the developed SOC estimation method in the EVs is described. The steps of this method are summarized in Figure 6.13.

The structure of the proposed BiLSTM model for SOC estimation in Evs explained in section 4.3. Like BiLSTM algorithm for estimate the SOC in one cell, the number of hidden layers and the units chosen by trial and error. The best results were obtained by two hidden layers with 256 BiLSTM units in the first layer and 64 LSTM units in the second layer. Furthermore, the Adam optimization algorithm with the initial learning rate $lr = 0.001$, and the MAE as loss functions is utilized for training the system.

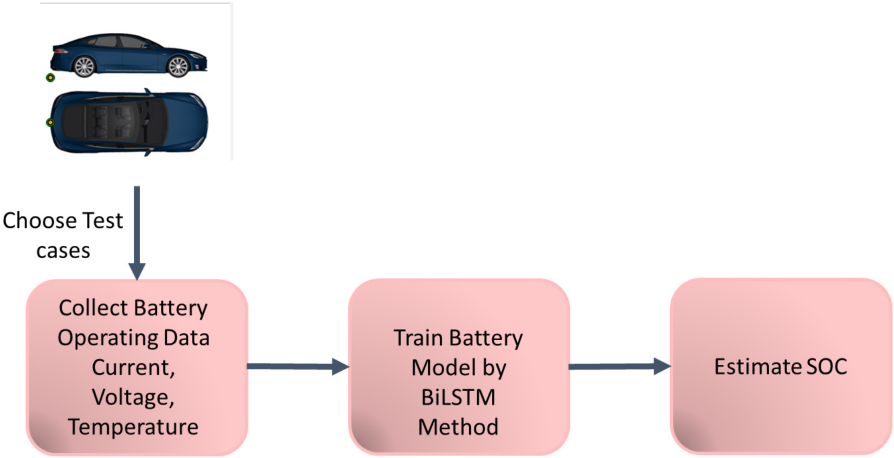

Figure 6.13: Implementation steps of BiLSTM algorithms for SOC estimation in the EV

The input vector is identified as $\mathbf{x}_t = \{V(t), I(t), T(t)\}$, where $V(t), I(t), T(t)$ are the battery pack voltage, the current of battery pack and the ambient temperature at time t, respectively. Here, the raw data with a sampling frequency of $1Hz$ is used as a input of the system. Furthermore, the time-step is set to 9000.

6.4.1 Drive Cycles Test Cases

Difference drive cycles test at varying ambient temperature are considered for collecting the Training and validation datasets. Five datasets developed by combination of the standard drive cycles test in United State such as: Federal Test Procedure 72/75 (FTP-72, FTP-75), US06, and HWFET. Additionally, the Artemis standard, which is a group of the drive cycles for powertrain test in Europe, is used to create three drive cycle test in this thesis. Moreover, four test cases as follows are defined to evaluated train and validation dataset:

6.4.1.1 Case 1

To create this case a route around Mulhouse with the 240 to 340 meter Elevation range was chosen. The Maximum speed defined $120km/h$ as a standard European for Highway. The details of the route and the speed curve are shown in Figure 6.11 and Figure 6.14, respectively.

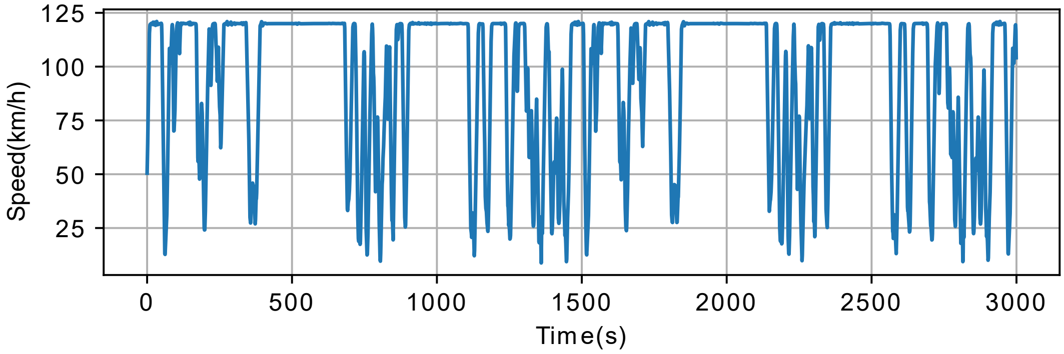

Figure 6.14: The speed profile of case 1. In this Case the maximum speed is $120km/h$.

6.4.1.2 Case 2

Case 2 is defined at the speed profile depicted in Figure 6.15 in the same route profile as the Case 1. The maximum speed in this case is $100km/h$.

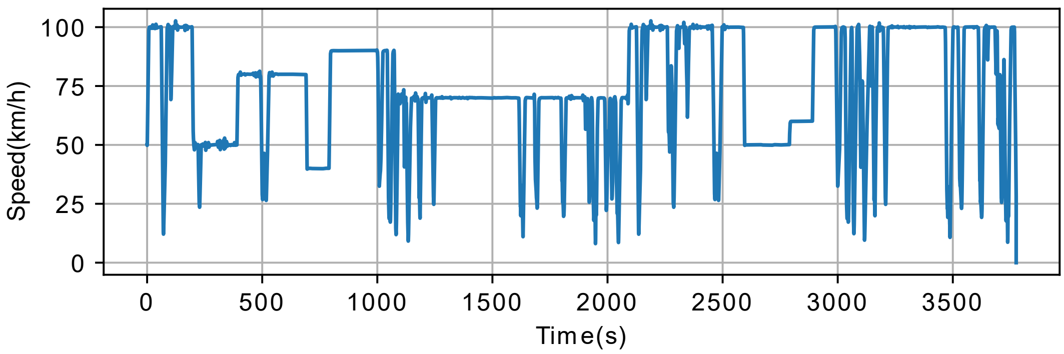

Figure 6.15: The speed profile with $100km/h$ maximum speed for case 2.

6.4.1.3 Case 3

For Case 3 a stochastic traffic with 10% density at the first 1000 second of driving is added to Case 1. Figure 6.16 illustrated the speed profile of this case.

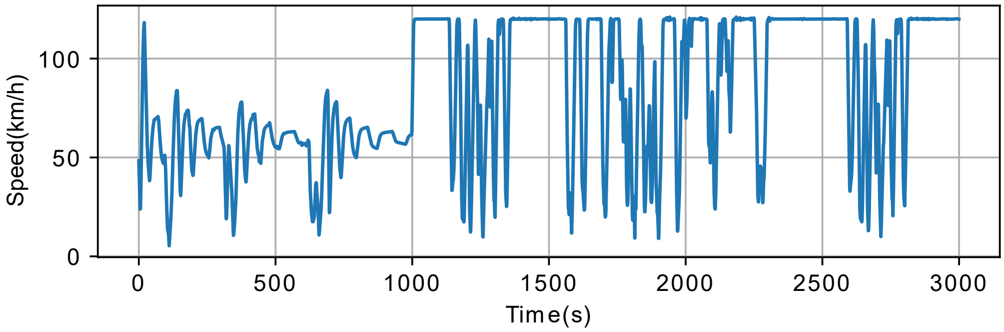

Figure 6.16: The speed profile of case 3. In this Case the maximum speed is $120km/h$, and at the first thousand seconds, the traffic density with ten percent variation is considered.

6.4.1.4 Case 4

A trip from Mulhouse to Metz is chosen for test case 4. The elevation in this route varies between $187m$ and $950m$. Additionally, a stochastic traffic with 10% density is evaluated to scenario maneuver with maximum speed $100Km/h$. Figure 6.17 and figure 6.18 show the route profile and the speed profile of this case, respectively.

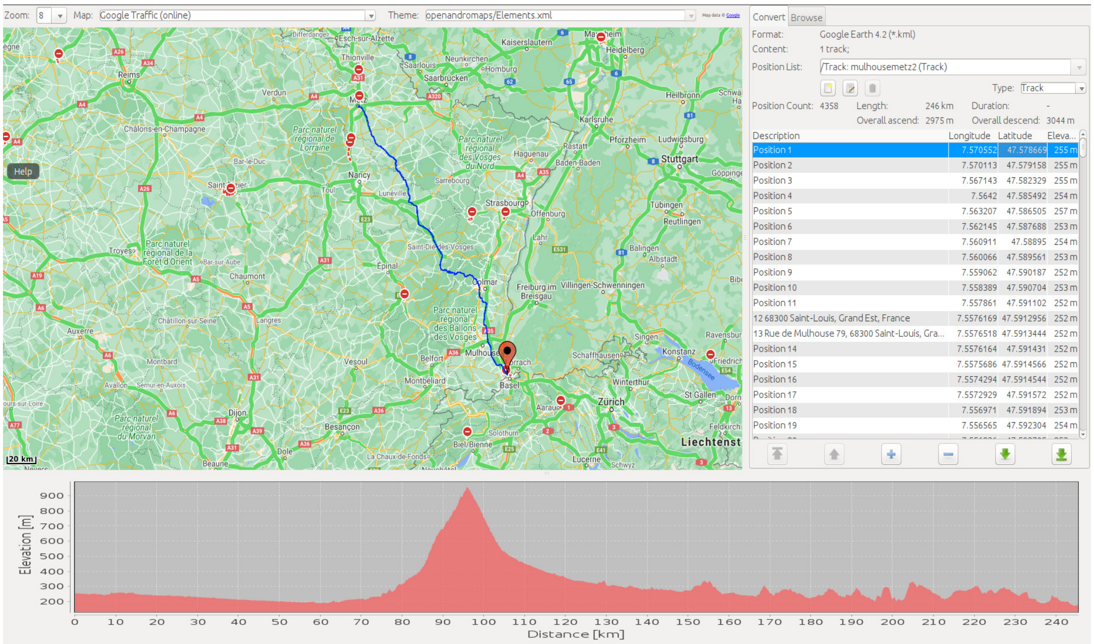

Format: Google Earth 4.2 (*.kml)
Content: 1 track;
Position List: /Track: mulhousemetz2 (Track)
Type: Track
Position Count: 4358
Length: 246 km
Duration: -
Overall ascend: 2975 m
Overall descend: 3044 m

Description	Longitude	Latitude	Eleva...
Position 1	7.570552	47.578669	255 m
Position 2	7.570113	47.579158	255 m
Position 3	7.567143	47.582329	255 m
Position 4	7.5642	47.585492	254 m
Position 5	7.563207	47.586505	257 m
Position 6	7.562145	47.587688	253 m
Position 7	7.560911	47.58895	254 m
Position 8	7.560066	47.589561	253 m
Position 9	7.559062	47.590187	252 m
Position 10	7.558389	47.590704	253 m
Position 11	7.557861	47.591102	252 m
12 68300 Saint-Louis, Grand Est, France	7.5576169	47.5912956	252 m
13 Rue de Mulhouse 79, 68300 Saint-Louis, Gra...	7.5576518	47.5913444	252 m
Position 14	7.5576164	47.591431	252 m
Position 15	7.5575686	47.5914566	252 m
Position 16	7.5574294	47.5914544	252 m
Position 17	7.5572929	47.591572	252 m
Position 18	7.556971	47.591894	253 m
Position 19	7.556565	47.592304	254 m

Figure 6.17: The rout profile of case 4.

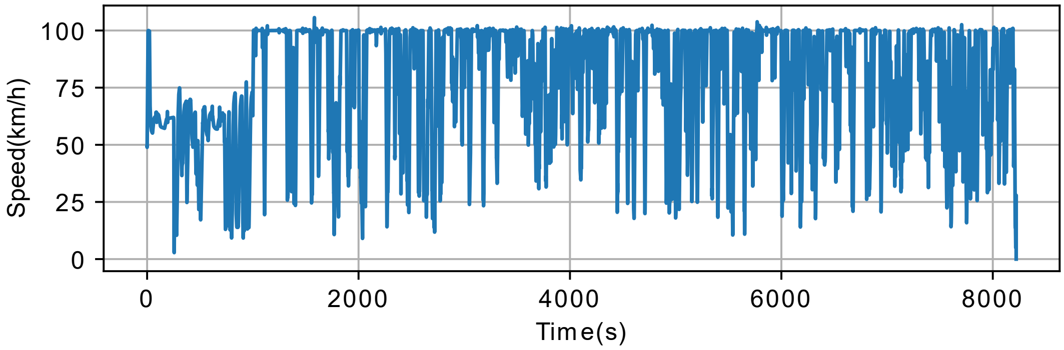

Figure 6.18: Case 4 assumes a speed profile with a maximum speed of $100km/h$ and a dynamic traffic with 10% density for the first 1000 seconds.

6.4.2 SOC Estimation Results in Offline Mode

In this section, the accuracy of SOC estimation by BiLSTM algorithms are described. The results are obtained by training the system with 22 random datasets from existing drive cycles test at varying ambient temperature. The MAE, MAX, and RMSE are derived from the average performances of different validation dataset. The MAE, RMSE, and MAX error achieved at $0°C$ are 0.74%, 0.92%, and 2.56%, respectively. These values of SOC estimation at $20°C$ are equal to $MAE = 0.7\%$, $RMSE = 1.04\%$, and $MAX = 3.7\%$. The performance of BiLSTM algorithm at $0°C$ and $20°C$ are illustrated in Figure 6.19 and Figure 6.20, respectively. SOC estimation accuracy by BiLSTM algorithm at different ambient temperature are listed in Table 6.2.

Table 6.2: The accuracy of SOC estimation by BiLSTM algorithm at different ambient temperature.

Temperature (°C)	MAE(%)	RMSE(%)	MAX(%)
0	0.74	0.92	2.56
10	0.57	0.81	3.5
20	0.7	1.04	3.7

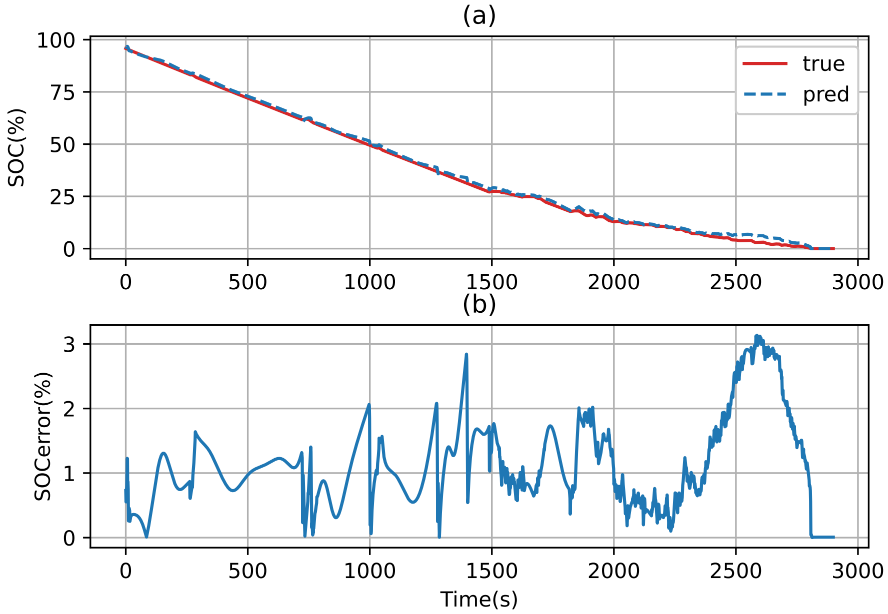

Figure 6.19: (a) SOC estimation and (b) error estimation of battery pack in EV at 0°C by BiLSTM network with 2 hidden layers, the 256 BiLSTM units are in the first layer and 64 LSTM units are in the second layer.

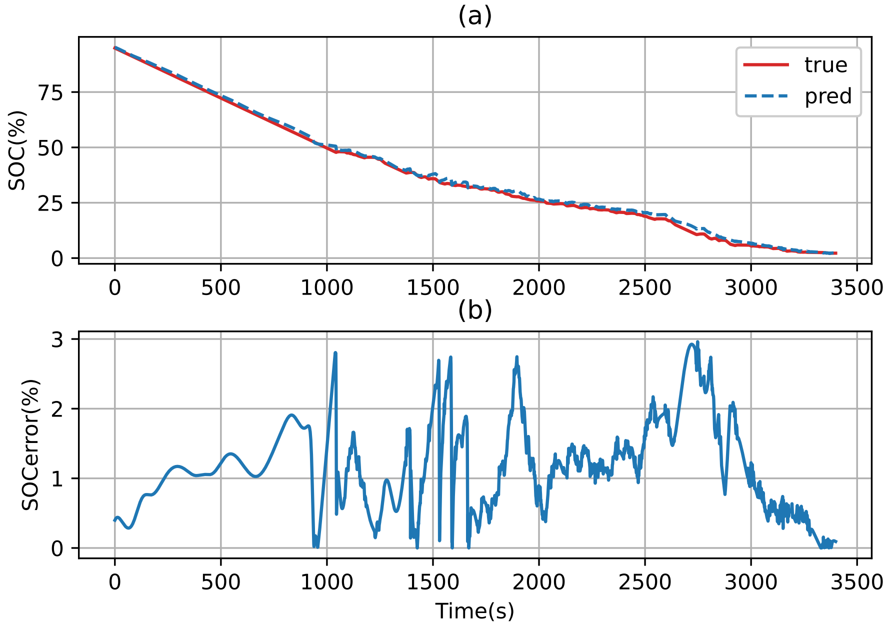

Figure 6.20: (a) SOC estimation and (b) error estimation of battery pack in EV at 20°C by BiLSTM network with 2 hidden layers, the 256 BiLSTM units are in the first layer and 64 LSTM units are in the second layer.

Additionally, to evaluate the system performance the algorithm were applied to a drive cycle at varying ambient temperature within 10°C to 30°C. Figure 6.21 shows the SOC estimation of battery pack over a driving cycle while the ambient temperature increasing. The $MAE = 0.8$ and $RMSE = 1.3$ shows the BiLSTM can achieved a good estimate at varied environment temperature.

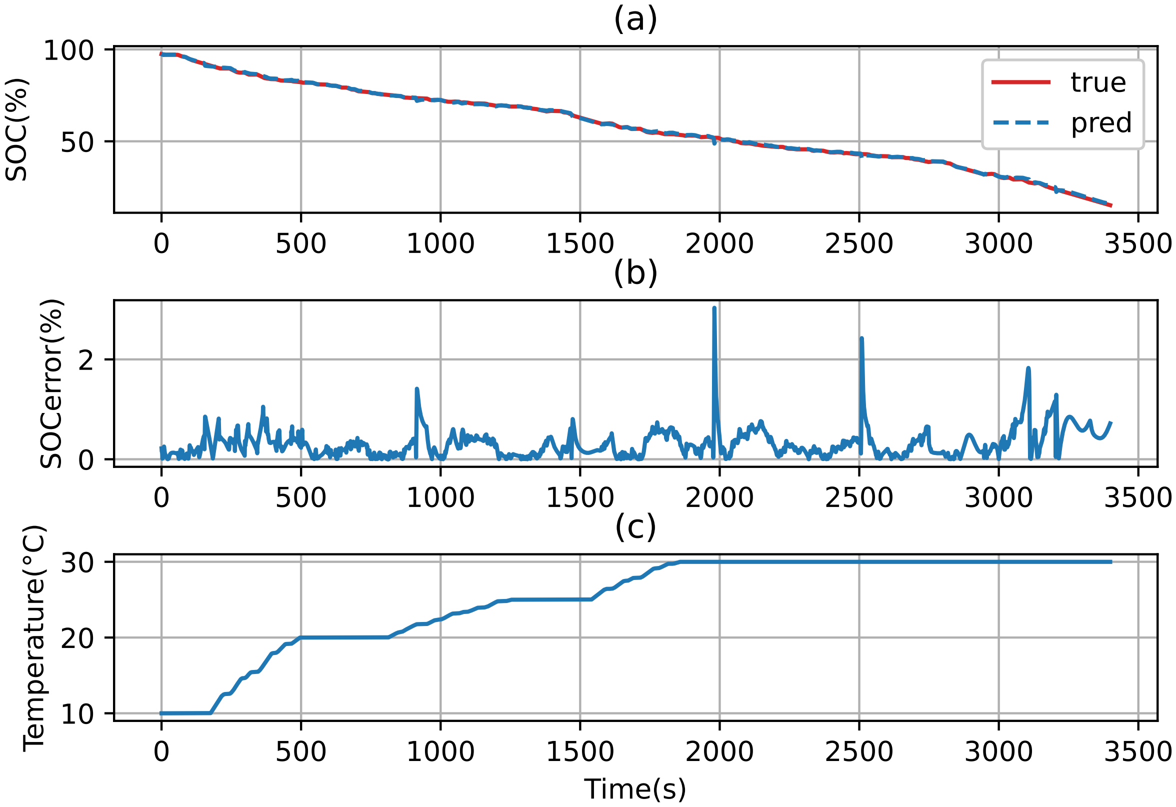

Figure 6.21: (a) SOC estimation and (b) error estimation of battery pack in EV at varying ambient temperature by BiLSTM network with 2 hidden layers, the 256 BiLSTM units are in the first layer and 64 LSTM units are in the second layer.

To examine the effect of the incorrect initial value of SOC, h_0 is considered zero. The SOC error is equal to 50% at the start of cycle, and converge to a desired SOC estimate quickly. The result in Figure 6.22 indicate that the convergence time is about 20 second.

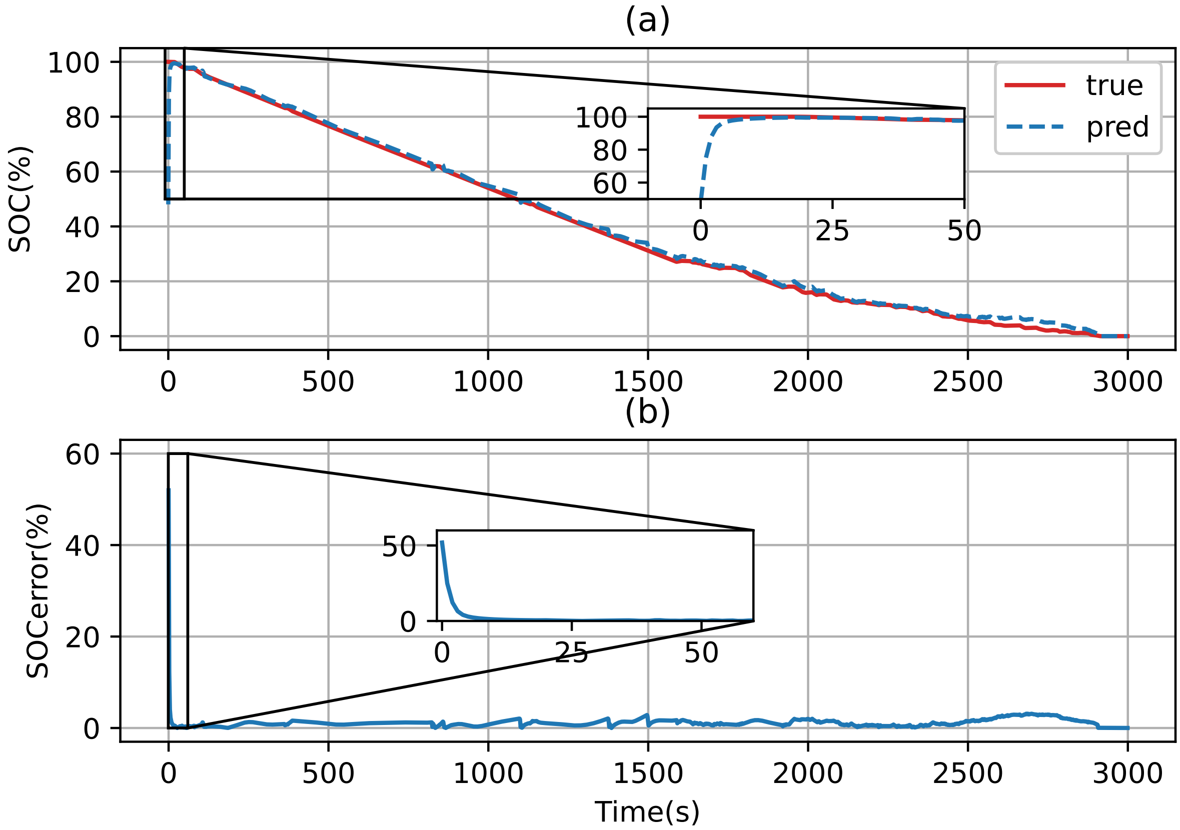

Figure 6.22: (a) SOC estimation and (b) error estimation of battery pack in EV at varying ambient temperature by BiLSTM network with 2 hidden layers, the 256 BiLSTM units are in the first layer and 64 LSTM units are in the second layer and $h_0 = 0$.

6.4.3 SOC Estimation Results in Real Time Mode

The performance of BiLSTM algorithm in real time simulation are investigated in this section. Pycarmaker library in python is used to connect python with IPGCarmaker to read/write data real time [133].

The best weights of BiLSTM model obtained by learned the system with Offline train datasets, are loaded in python to used as a model for prediction. Since the sampling frequency of training dataset was $1Hz$, the battery current, the battery voltage and the temperature must be read from Carmaker each one second and used as a input data in system to predict the SOC at time t. The environment of simulation the system in real time is depicted in Figure 6.23.

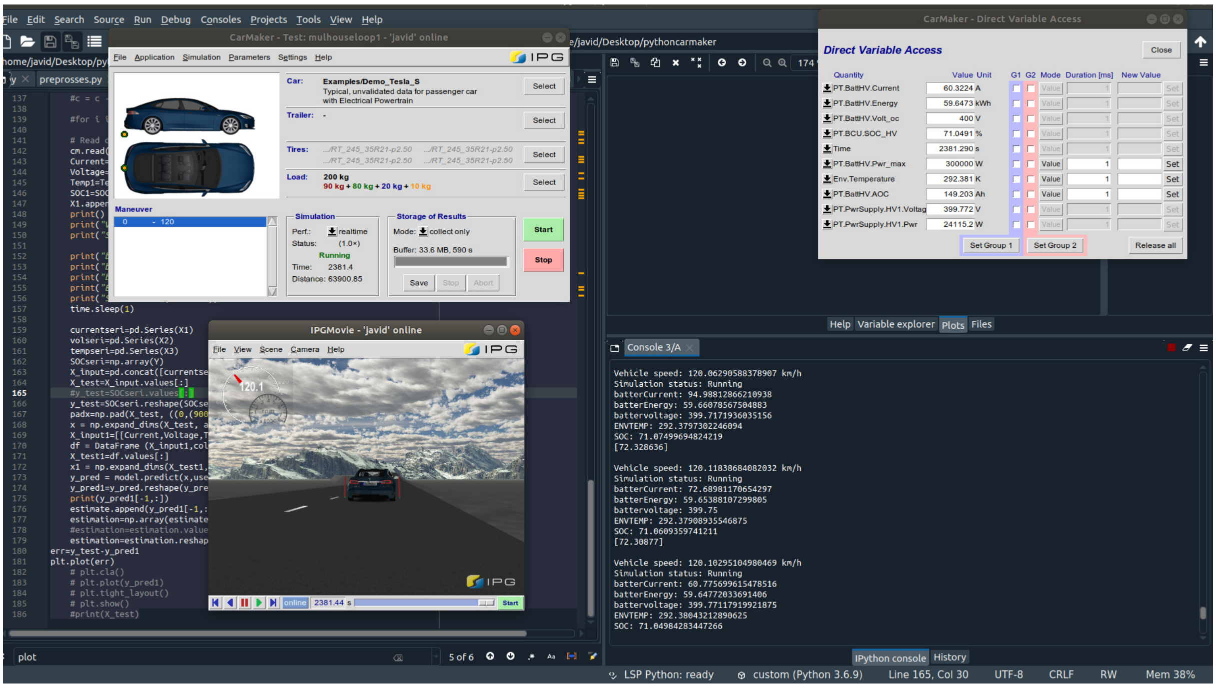

```
    #c = c -
    
    #for i i
    
    # Read d
    cm.read(
    Current=
    Voltage=
    Temp1=Te
    SOC1=SOC
    X1.appen
    print()
    print("V
    print("S
    
    print("b
    print("b
    print("b
    print("E
    print("S
    time.sleep(1)
    
    currentseri=pd.Series(X1)
    volseri=pd.Series(X2)
    tempseri=pd.Series(X3)
    SOCseri=np.array(Y)
    X_input=pd.concat([currentse
    X_test=X_input.values[:]
    #y_test=SOCseri.values[:]
    y_test=SOCseri.reshape(SOCse
    padx=np.pad(X_test, ((0,(900
    x = np.expand_dims(X_test, a
    X_input1=[[Current,Voltage,T
    df = DataFrame (X_input1,col
    X_test1=df.values[:]
    x1 = np.expand_dims(X_test1,
    y_pred = model.predict(x,use
    y_pred1=y_pred.reshape(y_pre
    print(y_pred1[-1,:])
    estimate.append(y_pred1[-1,:
    estimation=np.array(estimate
    #estimation=estimation.value
    estimation=estimation.reshap
err=y_test-y_pred1
plt.plot(err)
    # plt.cla()
    # plt.plot(y_pred1)
    # plt.tight_layout()
    # plt.show()
    #print(X_test)
```

Car: Examples/Demo_Tesla_S
Typical, unvalidated data for passenger car with Electrical Powertrain
Trailer: -
Tires: .../RT_245_35R21-p2.50 .../RT_245_35R21-p2.50 .../RT_245_35R21-p2.50 .../RT_245_35R21-p2.50
Load: 200 kg
90 kg + 80 kg + 20 kg + 10 kg

Simulation
Perf.: realtime
Status: (1.0×) Running
Time: 2381.4
Distance: 63900.85

Storage of Results
Mode: collect only
Buffer: 33.6 MB, 590 s

Direct Variable Access

Quantity	Value	Unit	G1	G2	Mode	Duration [ms]	New Value	
PT.BattHV.Current	60.3224	A	☐	☐	Value	1		Set
PT.BattHV.Energy	59.6473	kWh	☐	☐	Value	1		Set
PT.BattHV.Volt_oc	400	V	☐	☐	Value	1		Set
PT.BCU.SOC_HV	71.0491	%	☐	☐	Value	1		Set
Time	2381.290	s	☐	☐	Value	1		Set
PT.BattHV.Pwr_max	300000	W	☐	☐	Value	1		Set
Env.Temperature	292.381	K	☐	☐	Value	1		Set
PT.BattHV.AOC	149.203	Ah	☐	☐	Value	1		Set
PT.PwrSupply.HV1.Voltag	399.772	V	☐	☐	Value	1		Set
PT.PwrSupply.HV1.Pwr	24115.2	W	☐	☐	Value	1		Set

```
Vehicle speed: 120.06290588378907 km/h
Simulation status: Running
batterCurrent: 94.98812866210938
batterEnergy: 59.66078567504883
battervoltage: 399.7171936035156
ENVTEMP: 292.3797302246094
SOC: 71.07499694824219
[72.328636]

Vehicle speed: 120.11838684082032 km/h
Simulation status: Running
batterCurrent: 72.68981170654297
batterEnergy: 59.65388107299805
battervoltage: 399.75
ENVTEMP: 292.37908935546875
SOC: 71.0609359741211
[72.30877]

Vehicle speed: 120.10295104980469 km/h
Simulation status: Running
batterCurrent: 60.775699615478516
batterEnergy: 59.64772033691406
battervoltage: 399.77117919921875
ENVTEMP: 292.38043212890625
SOC: 71.04984283447266
```

Figure 6.23: The environment of simulation BiLSTM Model to estimate the SOC in real time.

The proposed system is tested on a sample validation case. Figure 6.24 shows the SOC estimation and the Soc error during a drive cycle. The performance of system are evaluated by calculated the MAE and RMSE at the end of cycle. The MAE, RMSE, and MAX error achieved 0.79%, 1.2%, and 2.69%, respectively. These values indicate the BiLSTM model can work with high accuracy in real time. Additionally, the converge time of BiLSTM algorithm at incorrect initial values ($h_0 = 0$) is illustrated in Figure 6.25.

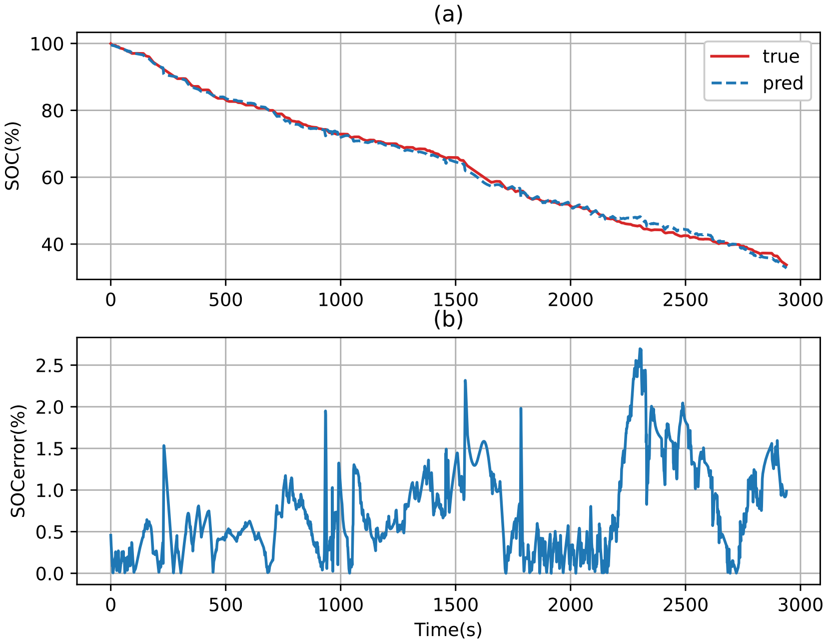

Figure 6.24: (a) SOC estimation and (b) error estimation of battery pack in EV in real time test by BiLSTM network with 2 hidden layers, the 256 BiLSTM units are in the first layer and 64 LSTM units are in the second layer.

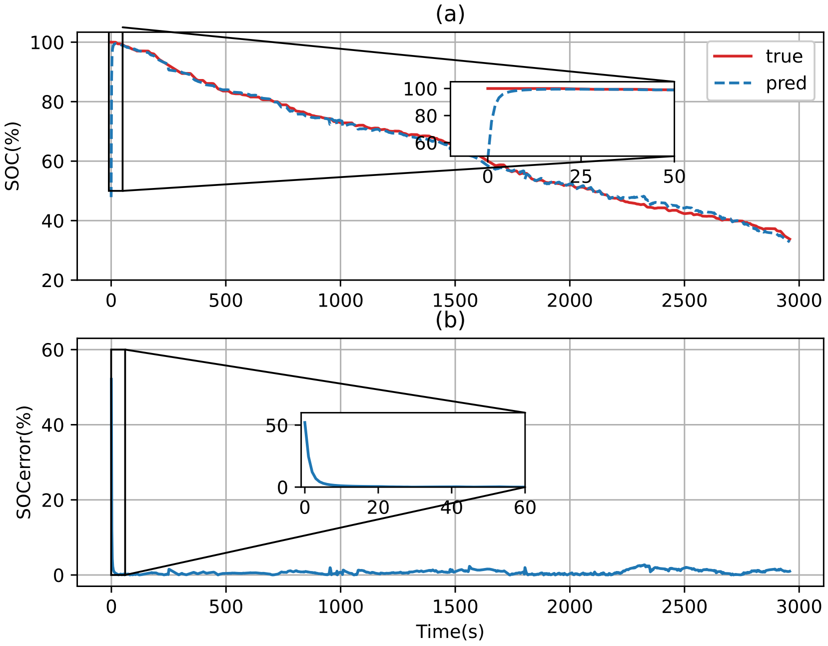

Figure 6.25: (a) SOC estimation and (b) error estimation of battery pack in EV in real time test by BiLSTM network with 2 hidden layers, the 256 BiLSTM units are in the first layer and 64 LSTM units are in the second layer and $h_0 = 0$.

6.5 Discussion

In this chapter, the BiLSTM algorithm for SOC estimation in EVs in offline and real time mode have been investigated. The IPGcarmaker software, and also the Tensorflow and keras Python libraries, were employed to create the proposed model. The learning processes were done on the server of Strasbourg University Computing Center.

The raw data without any normalization is used as a trained and validation data in the BiLSTM estimator to decrease the computation complexity. The results here are confirmed the ability of the BiLSTM algorithm to perform estimate the SOC of the battery-pack in both Offline and real time mode, as well as in varying ambient temperature.

7

CONCLUSIONS AND PERSPECTIVES

Contents

7.1 Conclusions

This thesis was undertaken to design and evaluate the SOC estimation of Li-ion batteries by using deep learning methods. In the face of humanity's pressing demand for clean energy, Li-ion batteries have steadily shown to be valuable because of their special features such as high energy density, self-discharge, fast charging time, easy operation, and extended life cycle. Accurate SOC estimation is essential for monitoring battery balance and safety mechanisms as well as measuring the amount of residual driving range. To accurately measure SOC in conventional estimation methods, battery modeling tools are essential. Deep learning algorithms have a great deal of representational capacity and expressible, which means that SOC estimates and battery modeling may be accomplished via learning about them through experience. One of the biggest advantages of this approach is that it streamlines the battery model creation and state estimate processes, allowing both to be done in a single step instead of requiring separate processes. This may be done without losing accuracy in estimating. Using deep learning approaches, a competitor's accuracy has been increased and information has been found in previously confusing situations. In many scenarios, it has been proven that deep learning approaches yield surprising results, such as their ability to both accurately resist random noise, offsets, and gains, thereby achieving greater estimation accuracy.

This research offers three novel techniques for estimating SOC sequences based on DRNNs. The results demonstrated that all of proposed methods can provide reliable estimate of SOC at varying ambient temperature. These methods and their advantages are listed below:

1. BiLSTM estimator that takes into account the sequential and bidirectional of Li-ion measurement sequences to describe the battery dynamics for estimating SOC at various ambient temperatures. Unlike previous unidirectional models, the built bidirectional model can incorporate long-term dependencies from both past and future directions, allowing it to acquire more temporal information from Li-ion batteries and therefore improve estimate accuracy. Additionally, The predicted sequence of successive SOC readings may intuitively represent the trend of the battery's resid-

ual capacity over a certain time period. This model introduces a novel approach to processing battery data sequences for SOC estimation.

2. RoLSTM algorithm suggested for SOC estimation are used three LSTM networks with fewer units are processed in parallel. As a result, the number of LSTM units can be reduced in the whole model. The method is a self-learning algorithm that can learn all the network parameters. The proposed algorithm is suitable for SOC estimation in different ambient temperatures. Moreover, the RoAdam optimizer gives a smoother estimate in comparison with other optimizer of LSTM network.
3. GRUs-based State Of Charge (SOC) estimation introduced as another data-driven estimator. A GRUs network has fewer parameters and a simpler structure, in comparison to the LSTM network.

This thesis is completed by implementing a BiLSTM algorithm to evaluate the SOC on EVs battery-pack in offline and real time mode. The IPGcarmaker was used to implement the model in issue. For the drivers, only the SOC of the pack are relevant, then defining a algorithm for estimating the battery pack's state is essential. Since the battery-pack has a complex and nonlinear model, the traditional algorithms have a complicated mathematical calculation. Moreover, by using the raw data of battery variable as a input this method did not need any prepossessing on the real data and consequently, BiLSTM model helps to reduce the computational load on the BMS.

7.2 Future Work

As Deep Recurrent Neural Networks techniques were suggested to SOC estimation of Li-ion battery, this study can be expanded to evaluate the State Of Health (SOH) for single and pack of Li-ion. Since, the Li-ion battery plays an important role in determining the driving range in autonomous car, assessment of SOC and SOH of the battery, can be incorporated into route optimization algorithms. Thus, doing longer tests on a real vehicle and obtain more experimental data in different landscapes and environmental challenges, is significant for the improvement the learning process of deep learning algorithms. For the last recommendation, the accurate SOC estimate will be used to charge the EV with solar energy at the time of its production, in order to improve the self-consumption of green energy. This estimation will help to better re-inject into the electrical grid the energy stored in the batteries by the Vehicle to Grid (V2G) principle during consumption peaks. The EV will play the role of a mobile battery that will increase the storage capacity of the electrical supply network for demand response application.

A

STANDARD DRIVE CYCLE TEST IN UNITED STATE

Contents

A.1 Federal Test Procedure (FTP)

A.1.1 FTP-72

FTP-72 also known as Urban Dynamometer Driving Schedule (UDDS), simulated a 12.07 km urban route at 1369 seconds with frequent pauses and a maximum speed of 91.25 km/h. In this cycle the average speed is equal to 31.5 km/h.

The Cycle is divided into two parts:

- Cold start phase: 505 seconds, containing 5.78 km at 41.2 km/h.
- Transient phase : 864 seconds.

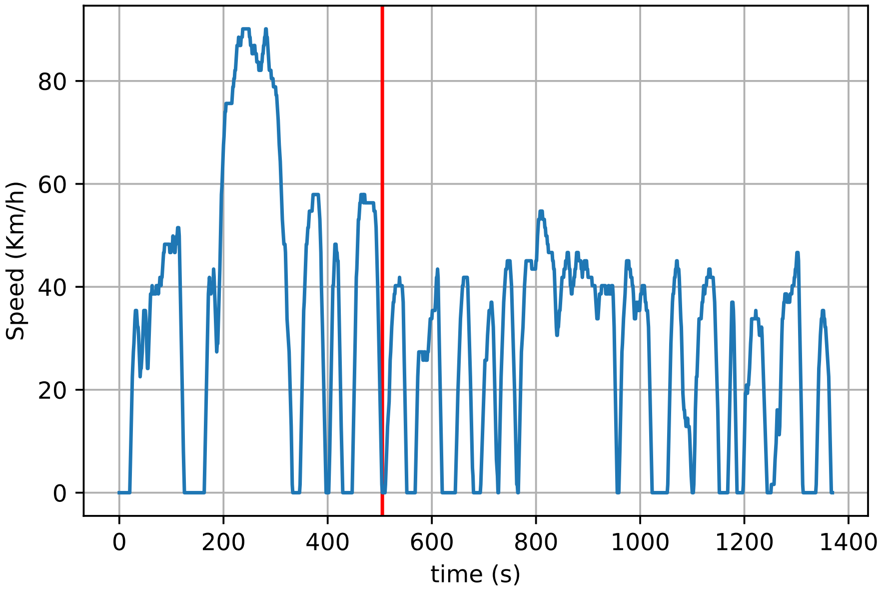

Figure A.1: The EPA Urban Dynamometer Driving Schedule (FTP-72)

A.1.2 FTP-75

The FTP-75 is generated by appending a third phase of 505 s to FTP-72 cycle. This phase is the same as the first phase of FTP-72, but with a hot beginning. The third period starts after the engine has been stopped for ten minutes. As a result, the whole FTP-75 cycle is made up of the following segments:

- Cold start transient phase (ambient temperature 20-30°C), 0-505 s.

- Stabilized phase 506-1372 s.
- Hot soak (min 540 s, max 660 s).
- Hot start transient phase, 0-505 s.

Each phase's emissions are collected in a separate teflon bag, tested, and stated in grams per mile (g/km). The cold start phase has a weighting value of 0.43, the 'stabilized' phase has a weighting factor of 1.0, and the hot start phase has a weighting factor of 0.57.

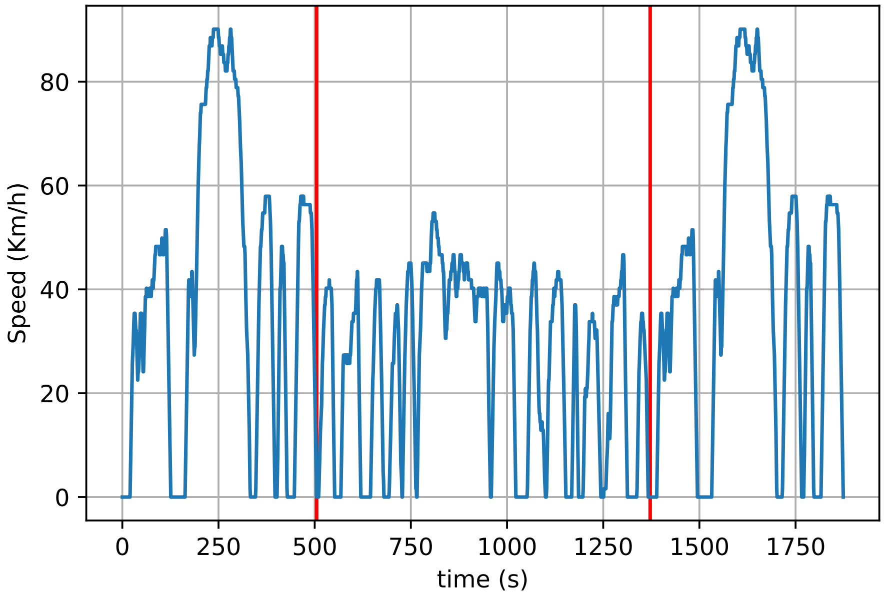

Figure A.2: The EPA Urban Dynamometer Driving Schedule (FTP-75)

A.2 Supplemental Federal Test Procedure Driving Schedule (US06)

To solve deficiencies, the FTP-75 test cycle in the aggressive speed and/or high speed driving behaviors, speed variations, and driving behavior after starting, the supplementary Supplemental Federal Test Procedure Driving Schedule (US06) has been created. This cycle is around 12.8 km with 77.9 km/h maximum speed and a length of 596 seconds, with an average speed of 129.2 km/h.

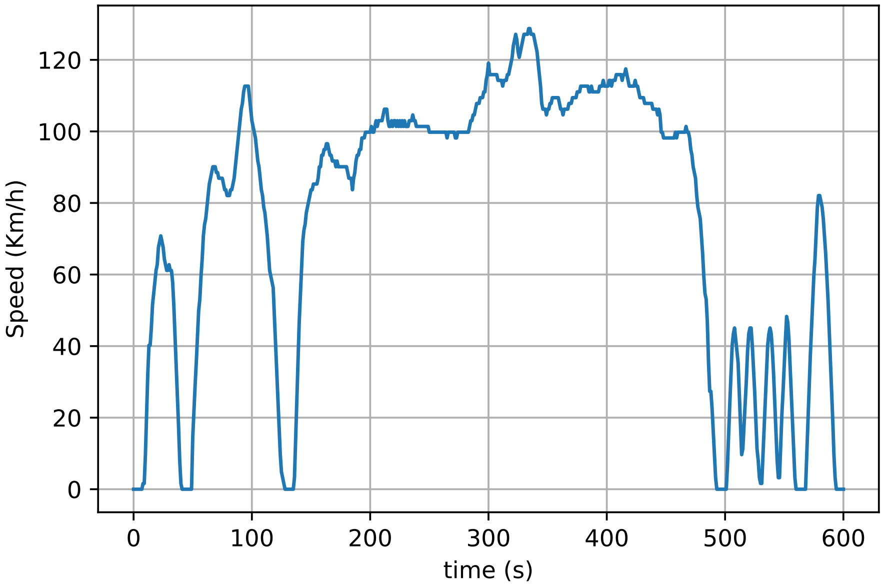

Figure A.3: The Supplemental Federal Test Procedure Driving Schedule cycle

A.3 Highway Fuel Economy Test (HWFET)

This cycle is a chassis dynamometer driving schedule established by the US EPA to determine the fuel efficiency of light duty cars. The HWFET calculates the fuel efficiency of highway transport, whereas the city rate is determined on the FTP-75 test.

The test takes place two times, with a pause between runs of maximum 17 s. The first is a preconditioning process for a vehicle, the second is the real emissions test.

Some typical parameters of the cycle are as follows:

- 765 seconds duration
- 16.45 km length
- 77.7 km/h average speed

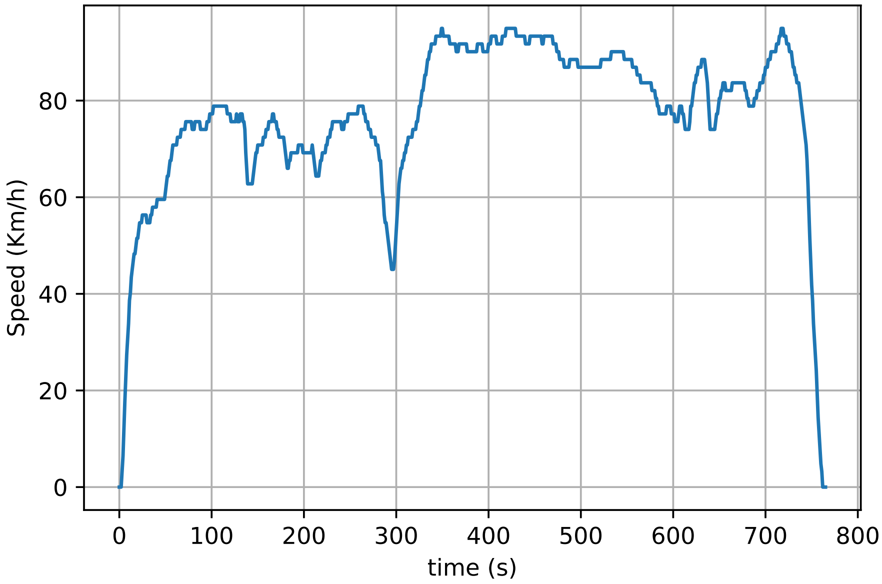

Figure A.4: The Highway Fuel Economy Test cycle

B

STANDARD DRIVE CYCLE TEST IN EUROPE

Contents

B.1 Artemis

In the European Assessment and Reliability of Transport Emission Models and Inventory Systems (Artemis) project, a European database of real-world driving behaviors was used to create Common Artemis Driving Cycles (CADC), which is a system for simulation of energy consumption that includes chassis dynamometer procedures. The three driving schedules are Urban, Rural, and Motorway, which are in turn designed for various driving conditions. Two versions of the Motorway cycle are now available; one has a top speed of 130 km/h, while the other one has a top speed of 150 km/h.

Table B.1 is a summary of some of the features of Artemis driving cycles. Figures B.1, B.2, and B.3 indicate the vehicle's speed in Artemis cycles. In addition to gear-changing techniques, Artemis cycle definitions contain several definitions.

Table B.1: The specification of Artemis Driving cycle

Characteristic	Urban	Rural Road	Motorway130	Motorway150
Distance (km)	4.47	17.27	28.74	29.55
Duration(s)	920	1081	1067	1067
Average speed(km/h)	17.5	57.5	97	99.7
Maximum speed(km/h)	58	112	132	150

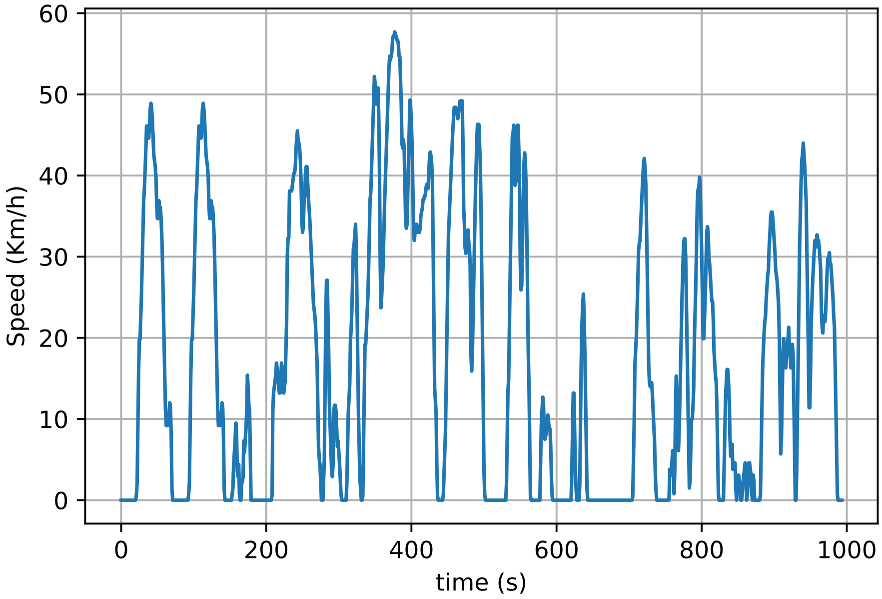

Figure B.1: The Artemis urban cycle

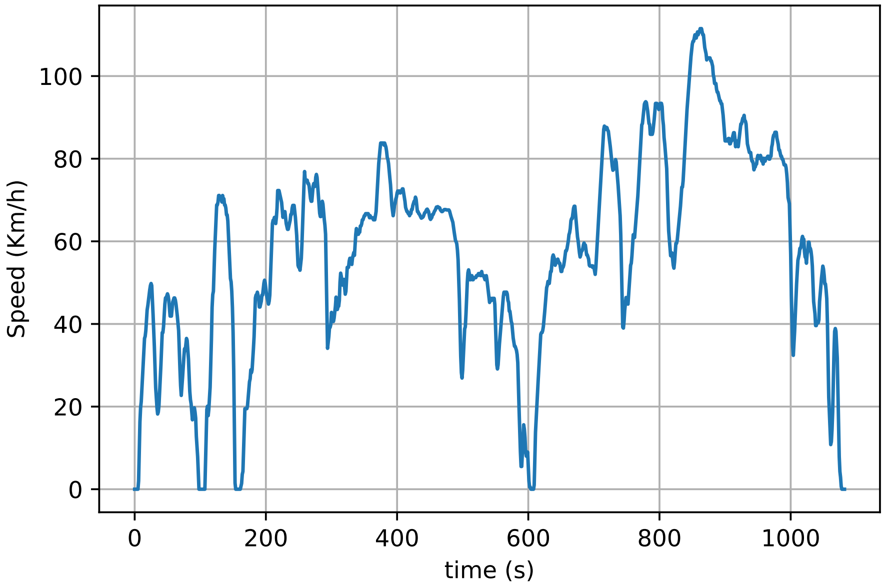

Figure B.2: The Artemis cycle for rural road

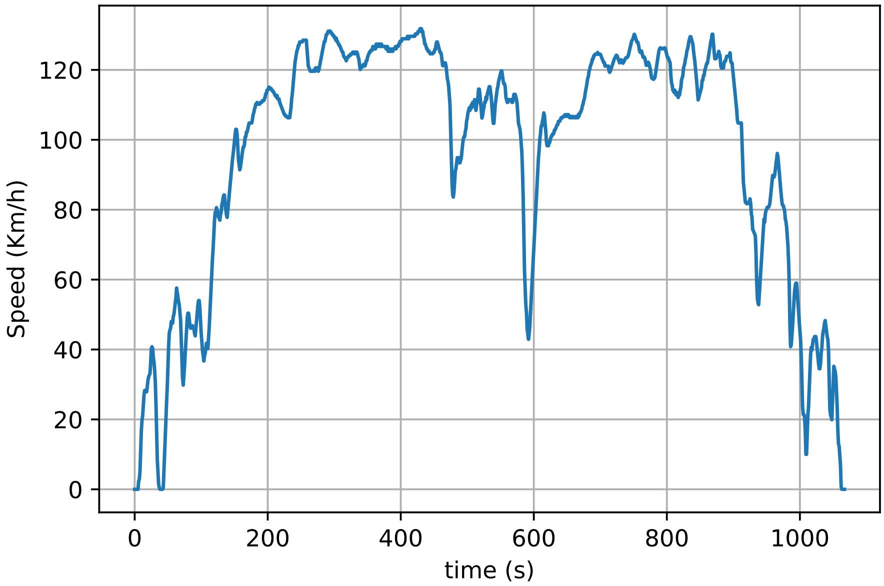

Figure B.3: The Artemis motorway cycle

BIBLIOGRAPHY

[1] https://historycollection.com/thomas-parker-invented-first-electric-car-1884/.

[2] Chaofeng Liu, Zachary G. Neale, and Guozhong Cao. Understanding electrochemical potentials of cathode materials in rechargeable batteries. *Materials Today*, 19(2):109 – 123, 2016.

[3] Wladislaw Waag, Stefan Käbitz, and Dirk Uwe Sauer. Experimental investigation of the lithium-ion battery impedance characteristic at various conditions and aging states and its influence on the application. *Applied Energy*, 102:885–897, 2013. Special Issue on Advances in sustainable biofuel production and use - XIX International Symposium on Alcohol Fuels - ISAF.

[4] Johannes Schmalstieg and Dirk Uwe Sauer. Full cell parameterization of a high-power lithium-ion battery for a physico-chemical model: Part II. thermal parameters and validation. *Journal of The Electrochemical Society*, 165(16):A3811–A3819, 2018.

[5] https://teslapower2020.blogspot.com/1979/09/tesla-engine-diagram.html.

[6] chrome-extension://oemmndcbldboiebfnladdacbdfmadadm/https://www.tesla.com/sites/default/files/downloads/2014_Model_S_Emergency_Response_Guide_en.pdf.

[7] Fangdan Zheng, Yinjiao Xing, Jiuchun Jiang, Bingxiang Sun, Jonghoon Kim, and

Michael Pecht. Influence of different open circuit voltage tests on state of charge online estimation for lithium-ion batteries. *Applied Energy*, 2016.

[8] World Health Organization. Regional Office for Europe. Air quality guidelines global update 2005 : particulate matter, ozone, nitrogen dioxide and sulfur dioxide, 2006.

[9] Hossein Farzin, Mahmud Fotuhi-Firuzabad, and Moein Moeini-Aghtaie. A Practical Scheme to Involve Degradation Cost of Lithium-Ion Batteries in Vehicle-to-Grid Applications. *IEEE Transactions on Sustainable Energy*, 7(4):1730–1738, oct 2016.

[10] Habiballah Rahimi-Eichi, Unnati Ojha, Federico Baronti, and Mo Yuen Chow. Battery management system: An overview of its application in the smart grid and electric vehicles. *IEEE Industrial Electronics Magazine*, 7(2):4–16, 2013.

[11] K. W.E. Cheng, B. P. Divakar, Hongjie Wu, Kai Ding, and Ho Fai Ho. Battery-management system (BMS) and SOC development for electrical vehicles. *IEEE Transactions on Vehicular Technology*, 60(1):76–88, jan 2011.

[12] R. Xiong, J. Cao, Q. Yu, H. He, and F. Sun. Critical review on the battery state of charge estimation methods for electric vehicles. *IEEE Access*, 6:1832–1843, 2018.

[13] Juan Rivera-Barrera, Nicolás Muñoz-Galeano, and Henry Sarmiento-Maldonado. SoC Estimation for Lithium-ion Batteries: Review and Future Challenges. *Electronics*, 2017.

[14] Ruifeng Zhang, Bizhong Xia, Baohua Li, Libo Cao, Yongzhi Lai, Weiwei Zheng, Huawen Wang, and Wei Wang. State of the art of lithium-ion battery soc estimation for electrical vehicles. *Energies*, 11(7), 2018.

[15] Christopher R. Lashway and Osama A. Mohammed. Adaptive battery management and parameter estimation through physics-based modeling and experimental verification. *IEEE Transactions on Transportation Electrification*, 2(4):454–464, dec 2016.

[16] Yinjiao Xing, Wei He, Michael Pecht, and Kwok Leung Tsui. State of charge estimation of lithium-ion batteries using the open-circuit voltage at various ambient temperatures. *Applied Energy*, 113:106–115, 2014.

[17] U. Westerhoff, T. Kroker, K. Kurbach, and M. Kurrat. Electrochemical impedance spectroscopy based estimation of the state of charge of lithium-ion batteries. *Journal of Energy Storage*, 8:244–256, nov 2016.

[18] Qianqian Wang, Jiao Wang, Pengju Zhao, Jianqiang Kang, Few Yan, and Changqing Du. Correlation between the model accuracy and model-based SOC estimation. *Electrochimica Acta*, 2017.

[19] Dave Andre, Christian Appel, Thomas Soczka-Guth, and Dirk Uwe Sauer. Advanced mathematical methods of SOC and SOH estimation for lithium-ion batteries. *Journal of Power Sources*, 2013.

[20] F. Claude, M. Becherif, and H. S. Ramadan. Experimental validation for Li-ion battery modeling using Extended Kalman Filters. *International Journal of Hydrogen Energy*, 42(40):25509–25517, oct 2017.

[21] Chuan-Xiang Yu, Yan-Min Xie, Zhao-Yu Sang, Shi-Ya Yang, and Rui Huang. State-of-charge estimation for lithium-ion battery using improved dukf based on state-parameter separation. *Energies*, 12(21), 2019.

[22] Mohammad Charkhgard and Mohammad Haddad Zarif. Design of adaptive H ∞ filter for implementing on state-of-charge estimation based on battery state-of-charge-varying modelling. *IET Power Electronics*, 2015.

[23] Quanqing Yu, Rui Xiong, Cheng Lin, Weixiang Shen, and Junjun Deng. Lithium-Ion Battery Parameters and State-of-Charge Joint Estimation Based on H-Infinity and Unscented Kalman Filters. *IEEE Transactions on Vehicular Technology*, 2017.

[24] Shuxiang Song, Zhenhan Wei, Haiying Xia, Mingcan Cen, and Chaobo Cai. State-of-charge (SOC) estimation using T-S fuzzy neural network for lithium iron phosphate

battery. In *26th International Conference on Systems Engineering, ICSEng 2018 - Proceedings*, 2019.

[25] Hanmin Sheng and Jian Xiao. Electric vehicle state of charge estimation: Nonlinear correlation and fuzzy support vector machine. *Journal of Power Sources*, 2015.

[26] Saeed Sepasi, Leon R. Roose, and Marc M. Matsuura. Extended kalman filter with a fuzzy method for accurate battery pack state of charge estimation. *Energies*, 8(6):5217–5233, 2015.

[27] Bizhong Xia, Deyu Cui, Zhen Sun, Zizhou Lao, Ruifeng Zhang, Wei Wang, Wei Sun, Yongzhi Lai, and Mingwang Wang. State of charge estimation of lithium-ion batteries using optimized Levenberg-Marquardt wavelet neural network. *Energy*, 2018.

[28] Xuanju Dang, Li Yan, Kai Xu, Xiru Wu, Hui Jiang, and Hanxu Sun. Open-Circuit Voltage-Based State of Charge Estimation of Lithium-ion Battery Using Dual Neural Network Fusion Battery Model. *Electrochimica Acta*, 2016.

[29] Wei He, Nicholas Williard, Chaochao Chen, and Michael Pecht. State of charge estimation for Li-ion batteries using neural network modeling and unscented Kalman filter-based error cancellation. *International Journal of Electrical Power and Energy Systems*, 2014.

[30] Mahammad A. Hannan, Molla S.Hossain Lipu, Aini Hussain, Mohamad H. Saad, and Afida Ayob. Neural network approach for estimating state of charge of lithium-ion battery using backtracking search algorithm. *IEEE Access*, 6:10069–10079, jan 2018.

[31] David Jiménez-Bermejo, Jesús Fraile-Ardanuy, Sandra Castaño-Solis, Julia Merino, and Roberto Álvaro-Hermana. Using Dynamic Neural Networks for Battery State of Charge Estimation in Electric Vehicles. In *Procedia Computer Science*, 2018.

[32] Juan Carlos Álvarez Antón, Paulino José García Nieto, Cecilio Blanco Viejo, and

José Antonio Vilán Vilán. Support vector machines used to estimate the battery state of charge. *IEEE Transactions on Power Electronics*, 28(12):5919–5926, 2013.

[33] Jiabo Li, Min Ye, Wei Meng, Xinxin Xu, and Shengjie Jiao. A novel state of charge approach of lithium ion battery using least squares support vector machine. *IEEE Access*, 8:195398–195410, 2020.

[34] Charu C. Aggarwal. *Neural Networks and Deep Learning*. 2018.

[35] Ian Goodfellow, Yoshua Bengio, and Aaron Courville. *Deep Learning*. MIT Press, 2016. http://www.deeplearningbook.org.

[36] Ghulam Abbas, Menaa Nawaz, and Farrukh Kamran. Performance comparison of narx amp; rnn-lstm neural networks for lifepo4 battery state of charge estimation. In *2019 16th International Bhurban Conference on Applied Sciences and Technology (IBCAST)*, pages 463–468, 2019.

[37] Gelareh Javid, Djaffar Ould Abdeslam, and Michel Basset. Adaptive online state of charge estimation of evs lithium-ion batteries with deep recurrent neural networks. *Energies*, 14(3), 2021.

[38] Ephrem Chemali, Phillip J. Kollmeyer, Matthias Preindl, and Ali Emadi. State-of-charge estimation of Li-ion batteries using deep neural networks: A machine learning approach. *Journal of Power Sources*, 2018.

[39] Ephrem Chemali, Phillip J. Kollmeyer, Matthias Preindl, Ryan Ahmed, and Ali Emadi. Long Short-Term Memory Networks for Accurate State-of-Charge Estimation of Li-ion Batteries. *IEEE Transactions on Industrial Electronics*, 2018.

[40] Ruxiu Zhao, Phillip J. Kollmeyer, Robert D. Lorenz, and Thomas M. Jahns. A compact methodology via a recurrent neural network for accurate equivalent circuit type modeling of lithium-ion batteries. *IEEE Transactions on Industry Applications*, 55(2):1922–1931, 2019.

[41] G. Javid, M. Basset, and D. O. Abdeslam. Adaptive online gated recurrent unit for lithium-ion battery soc estimation. In *IECON 2020 The 46th Annual Conference of the IEEE Industrial Electronics Society*, pages 3583–3587, Oct 2020.

[42] Haimin Yang, Zhisong Pan, and Qing Tao. Robust and adaptive online time series prediction with long short-term memory. *Computational Intelligence and Neuroscience*, 2017.

[43] THE HISTORY OF THE FIRST ELECTRIC CARS. https://easyelectriclife.groupe.renault.com/en/outlook/lifestyle-en/the-history-of-the-first-electric-cars/.

[44] Keith McClellan. The Morrison Electric: Iowa's First Automobile. *The Annals of Iowa*, 36(8), 1963.

[45] Masayuki Morimoto. Which is the first electric vehicle? *Electrical Engineering in Japan (English translation of Denki Gakkai Ronbunshi)*, 192(2), 2015.

[46] IEA Paris IEA (2020), Electric Vehicles, 2020. https://www.iea.org/reports/electric-vehicles.

[47] IEA Paris IEA (2019), Electric Vehicles, 2019. https://www.iea.org/reports/global-ev-outlook-2019.

[48] ALESSANDRO VOLTA, 1745–1827. In *Late Eighteenth Century European Scientists*, pages 127–142. Elsevier, jan 1966.

[49] Christopher L Heth. Energy on demand: A brief history of the development of the battery. *Substantia*, 3(2):77 – 86, Nov. 2019.

[50] M. Stanley Whittingham. History, evolution, and future status of energy storage. *Proceedings of the IEEE*, 100(Special Centennial Issue):1518–1534, 2012.

[51] P. Kurzweil. Gaston Planté and his invention of the lead-acid battery-The genesis of the first practical rechargeable battery. *Journal of Power Sources*, 195(14):4424–4434, jul 2010.

[52] David A.J. Rand and Patrick T. Moseley. Energy Storage with Lead-Acid Batteries. In *Electrochemical Energy Storage for Renewable Sources and Grid Balancing*, pages 201–222. Elsevier Inc., jan 2015.

[53] P. Kurzweil and J. Garche. Overview of batteries for future automobiles. In *Lead-Acid Batteries for Future Automobiles*, pages 27–96. Elsevier Inc., mar 2017.

[54] Balasubramanian Viswanathan. Batteries. In *Energy Sources*, pages 263–313. Elsevier, jan 2017.

[55] Patrick Bernard and Michael Lippert. Nickel-Cadmium and Nickel-Metal Hydride Battery Energy Storage. In *Electrochemical Energy Storage for Renewable Sources and Grid Balancing*, pages 223–251. Elsevier Inc., jan 2015.

[56] Florian Schipper and Doron Aurbach. A brief review: Past, present and future of lithium ion batteries. *Russian Journal of Electrochemistry*, 52(12):1095–1121, dec 2016.

[57] Tobias Placke, Richard Kloepsch, Simon Dühnen, and Martin Winter. Lithium ion, lithium metal, and alternative rechargeable battery technologies: the odyssey for high energy density. *Journal of Solid State Electrochemistry*, 21(7), 2017.

[58] M. Wakihara. Recent developments in lithium ion batteries. *Materials Science & Engineering R-reports*, 33:109–134, 2001.

[59] *Batteries for Sustainability.* 2013.

[60] M. A. Hannan, M. S.H. Lipu, A. Hussain, and A. Mohamed. A review of lithium-ion battery state of charge estimation and management system in electric vehicle applications: Challenges and recommendations, 2017.

[61] Yu Miao, Patrick Hynan, Annette von Jouanne, and Alexandre Yokochi. Current li-ion battery technologies in electric vehicles and opportunities for advancements. *Energies*, 12(6), 2019.

[62] Hee-Je Kim, TNV Krishna, Kamran Zeb, Vinodh Rajangam, Chandu V. V. Muralee Gopi, Sangaraju Sambasivam, Kummara Venkata Guru Raghavendra, and Ihab M. Obaidat. A comprehensive review of li-ion battery materials and their recycling techniques. *Electronics*, 9(7), 2020.

[63] Chen Zhao, He Yin, and Chengbin Ma. Quantitative evaluation of lifepo$_4$ battery cycle life improvement using ultracapacitors. *IEEE Transactions on Power Electronics*, 31(6):3989–3993, 2016.

[64] Kai Sun and Qifang Shu. Overview of the types of battery models. In *Proceedings of the 30th Chinese Control Conference*, pages 3644–3648, 2011.

[65] Marian Tomasov, Martina Kajanova, Peter Bracinik, and David Motyka. Overview of battery models for sustainable power and transport applications. In *Transportation Research Procedia*, volume 40, pages 548–555. Elsevier B.V., jan 2019.

[66] Ming Shen and Qing Gao. A review on battery management system from the modeling efforts to its multiapplication and integration, 2019.

[67] Laifa Tao, Jian Ma, Yujie Cheng, Azadeh Noktehdan, Jin Chong, and Chen Lu. A review of stochastic battery models and health management. *Renewable and Sustainable Energy Reviews*, 80:716–732, 2017.

[68] Jinhao Meng, Guangzhao Luo, Mattia Ricco, Maciej Swierczynski, Daniel-Ioan Stroe, and Remus Teodorescu. Overview of lithium-ion battery modeling methods for state-of-charge estimation in electrical vehicles. *Applied Sciences*, 8(5), 2018.

[69] Joel C. Forman, Saeid Bashash, Jeffrey L. Stein, and Hosam K. Fathy. Reduction of an electrochemistry-based li-ion battery model via quasi-linearization and padé approximation. *Journal of The Electrochemical Society*, 158(2):A93, 2011.

[70] Cheng Lin and Aihua Tang. Simplification and efficient simulation of electrochemical model for li-ion battery in evs. *Energy Procedia*, 104:68–73, 2016. Clean Energy for Clean City: CUE 2016–Applied Energy Symposium and Forum: Low-Carbon Cities and Urban Energy Systems.

[71] Hongwen He, Rui Xiong, and Jinxin Fan. Evaluation of lithium-ion battery equivalent circuit models for state of charge estimation by an experimental approach. *Energies*, 4(4):582–598, 2011.

[72] Abbas Fotouhi, Daniel J. Auger, Karsten Propp, Stefano Longo, and Mark Wild. A review on electric vehicle battery modelling: From Lithium-ion toward Lithium-Sulphur, 2016.

[73] Davide Andrea. *Battery Management Systems for Large Lithium-ion Battery Packs*. 2010.

[74] M. A. Hannan, M. M. Hoque, A. Hussain, Y. Yusof, and P. J. Ker. State-of-the-art and energy management system of lithium-ion batteries in electric vehicle applications: Issues and recommendations. *IEEE Access*, 6:19362–19378, 2018.

[75] M. M. Hoque, M. A. Hannan, and A. Mohamed. Voltage equalization control algorithm for monitoring and balancing of series connected lithium-ion battery. *Journal of Renewable and Sustainable Energy*, 8(2), 2016.

[76] Huaqiang Liu, Zhongbao Wei, Weidong He, and Jiyun Zhao. Thermal issues about Li-ion batteries and recent progress in battery thermal management systems: A review, 2017.

[77] Andrea Vezzini. 15 - lithium-ion battery management. In Gianfranco Pistoia, editor, *Lithium-Ion Batteries*, pages 345–360. Elsevier, Amsterdam, 2014.

[78] Languang Lu, Xuebing Han, Jianqiu Li, Jianfeng Hua, and Minggao Ouyang. A review on the key issues for lithium-ion battery management in electric vehicles. *Journal of Power Sources*, 226:272–288, 2013.

[79] Utpal Kumar Das, Kok Soon Tey, Mehdi Seyedmahmoudian, Saad Mekhilef, Moh Yamani Idna Idris, Willem Van Deventer, Bend Horan, and Alex Stojcevski. Forecasting of photovoltaic power generation and model optimization: A review. *Renewable and Sustainable Energy Reviews*, 81:912–928, jan 2018.

[80] Gelareh Javid, Djaffar Ould Abdeslam, and Dirk Benyoucef. Maximum power point tracking of photovoltaic power system with adaptive fuzzy terminal sliding mode controller. In *2018 IEEE International Conference on Environment and Electrical Engineering and 2018 IEEE Industrial and Commercial Power Systems Europe (EEEIC / I CPS Europe)*, pages 1–6, 2018.

[81] Bengt Sundén. Thermal management of batteries. In *Hydrogen, Batteries and Fuel Cells*, pages 93–110. Elsevier, jan 2019.

[82] Wladislaw Waag, Christian Fleischer, and Dirk Uwe Sauer. Critical review of the methods for monitoring of lithium-ion batteries in electric and hybrid vehicles. *Journal of Power Sources*, 258:321–339, 2014.

[83] M.A. Hannan, M.S.H. Lipu, A. Hussain, and A. Mohamed. A review of lithium-ion battery state of charge estimation and management system in electric vehicle applications: Challenges and recommendations. *Renewable and Sustainable Energy Reviews*, 78:834–854, 2017.

[84] Yuan Zou, Xiaosong Hu, Hongmin Ma, and Shengbo Eben Li. Combined state of charge and state of health estimation over lithium-ion battery cell cycle lifespan for electric vehicles. *Journal of Power Sources*, 273:793–803, 2015.

[85] Rui Xiong. *Battery SOC and SOH Estimation*, pages 107–165. Springer Singapore, Singapore, 2020.

[86] Yuejiu Zheng, Minggao Ouyang, Xuebing Han, Languang Lu, and Jianqiu Li. Investigating the error sources of the online state of charge estimation methods for lithium-ion batteries in electric vehicles, 2018.

[87] Ephrem Chemali, Matthias Preindl, Pawel Malysz, and Ali Emadi. Electrochemical and electrostatic energy storage and management systems for electric drive vehicles: State-of-the-art review and future trends. *IEEE Journal of Emerging and Selected Topics in Power Electronics*, 4(3):1117–1134, 2016.

[88] Jun Xu, Chunting Chris Mi, Binggang Cao, and Junyi Cao. A new method to estimate the state of charge of lithium-ion batteries based on the battery impedance model. *Journal of Power Sources*, 233:277–284, 2013.

[89] Nina Meddings, Marco Heinrich, Frédéric Overney, Jong-Sook Lee, Vanesa Ruiz, Emilio Napolitano, Steffen Seitz, Gareth Hinds, Rinaldo Raccichini, Miran Gaberšček, and Juyeon Park. Application of electrochemical impedance spectroscopy to commercial li-ion cells: A review. *Journal of Power Sources*, 480:228742, 2020.

[90] Y. Ma, X. Zhou, B. Li, and H. Chen. Fractional modeling and soc estimation of lithium-ion battery. *IEEE/CAA Journal of Automatica Sinica*, 3(3):281–287, 2016.

[91] H. He, R. Xiong, X. Zhang, F. Sun, and J. Fan. State-of-charge estimation of the lithium-ion battery using an adaptive extended kalman filter based on an improved thevenin model. *IEEE Transactions on Vehicular Technology*, 60(4):1461–1469, 2011.

[92] Yidan Xu, Minghui Hu, Anjian Zhou, Yunxiao Li, Shuxian Li, Chunyun Fu, and Changchao Gong. State of charge estimation for lithium-ion batteries based on adaptive dual kalman filter. *Applied Mathematical Modelling*, 77:1255–1272, 2020.

[93] Prashant Shrivastava, Tey Kok Soon, Mohd Yamani Idna Bin Idris, and Saad Mekhilef. Overview of model-based online state-of-charge estimation using Kalman filter family for lithium-ion batteries, oct 2019.

[94] Charles K. Chui and Guanrong Chen. *Kalman Filtering*. Springer International Publishing, 2017.

[95] J. Chiasson and B. Vairamohan. Estimating the state of charge of a battery. In *Proceedings of the 2003 American Control Conference, 2003.*, volume 4, pages 2863–2868 vol.4, 2003.

[96] Z. Luo, Y. Li, and Y. Lou. An adaptive kalman filter to estimate state-of-charge of

lithium-ion batteries. In *2015 IEEE International Conference on Information and Automation*, pages 1227–1232, 2015.

[97] J. R. Choudhury, T. P. Banerjee, H. Gurung, A. K. Bhattacharjee, and S. Das. Real time state of charge prediction using kalman filter. In *2009 World Congress on Nature Biologically Inspired Computing (NaBIC)*, pages 1190–1194, 2009.

[98] Gregory L. Plett. Extended kalman filtering for battery management systems of lipb-based hev battery packs: Part 3. state and parameter estimation. *Journal of Power Sources*, 134(2):277–292, 2004.

[99] C. Huang, Z. Wang, Z. Zhao, L. Wang, C. S. Lai, and D. Wang. Robustness evaluation of extended and unscented kalman filter for battery state of charge estimation. *IEEE Access*, 6:27617–27628, 2018.

[100] Xin Lai, Yuejiu Zheng, and Tao Sun. A comparative study of different equivalent circuit models for estimating state-of-charge of lithium-ion batteries. *Electrochimica Acta*, 259:566–577, 2018.

[101] Gregory L. Plett. Extended kalman filtering for battery management systems of lipb-based hev battery packs: Part 1. background. *Journal of Power Sources*, 134(2):252–261, 2004.

[102] Shijie Tong, Joseph H. Lacap, and Jae Wan Park. Battery state of charge estimation using a load-classifying neural network. *Journal of Energy Storage*, 7:236–243, aug 2016.

[103] J. N. Hu, J. J. Hu, H. B. Lin, X. P. Li, C. L. Jiang, X. H. Qiu, and W. S. Li. State-of-charge estimation for battery management system using optimized support vector machine for regression. *Journal of Power Sources*, 269:682–693, dec 2014.

[104] L.A. Zadeh. Fuzzy sets. *Information and Control*, 8(3):338–353, 1965.

[105] Pritpal Singh. A fuzzy system methodology to determine state-of-charge in primary u/so2 and other batteries pritpal singh ece department villanova university. *38th Power Sources Conference*, page 295, 1998.

[106] Alvin J Salkind, Craig Fennie, Pritpal Singh, Terrill Atwater, and David E Reisner. Determination of state-of-charge and state-of-health of batteries by fuzzy logic methodology. *Journal of Power Sources*, 80(1):293–300, 1999.

[107] Pritpal Singh, Ramana Vinjamuri, Xiquan Wang, and David Reisner. Design and implementation of a fuzzy logic-based state-of-charge meter for Li-ion batteries used in portable defibrillators. *Journal of Power Sources*, 162(2 SPEC. ISS.):829–836, nov 2006.

[108] A. A. Hussein. Capacity fade estimation in electric vehicle li-ion batteries using artificial neural networks. *IEEE Transactions on Industry Applications*, 51(3):2321–2330, 2015.

[109] M. A. Hannan, M. S. H. Lipu, A. Hussain, M. H. Saad, and A. Ayob. Neural network approach for estimating state of charge of lithium-ion battery using backtracking search algorithm. *IEEE Access*, 6:10069–10079, 2018.

[110] Jinquan Guo, Hongwen He, and Jiankun Peng. Real-time energy management for plug-in hybrid electric vehicle based on economy driving pro system. In *Energy Procedia*, 2019.

[111] P. Jansen, T. Gebel, D. Renner, D. Vergossen, W. John, and J. Götze. An approach to determine the state of charge of a lithium iron phosphate cell using classification methods based on frequency domain data. In *8th IET International Conference on Power Electronics, Machines and Drives (PEMD 2016)*, pages 1–6, 2016.

[112] Yifeng Guo, Zeshuang Zhao, and Limin Huang. SoC Estimation of Lithium Battery Based on Improved BP Neural Network. In *Energy Procedia*, volume 105, pages 4153–4158. Elsevier Ltd, may 2017.

[113] Wenhui Zheng, Bizhong Xia, Wei Wang, Yongzhi Lai, Mingwang Wang, and Huawen Wang. State of charge estimation for power lithium-ion battery using a fuzzy logic sliding mode observer. *Energies*, 12(13), 2019.

[114] Z. He, M. Gao, and J. Xu. Ekf-ah based state of charge online estimation for lithium-ion power battery. In *2009 International Conference on Computational Intelligence and Security*, volume 1, pages 142–145, 2009.

[115] Haifeng Dai, Pingjing Guo, Xuezhe Wei, Zechang Sun, and Jiayuan Wang. ANFIS (adaptive neuro-fuzzy inference system) based online SOC (State of Charge) correction considering cell divergence for the EV (electric vehicle) traction batteries. *Energy*, 80:350–360, feb 2015.

[116] A. Fotouhi, K. Propp, and D. J. Auger. Electric vehicle battery model identification and state of charge estimation in real world driving cycles. In *2015 7th Computer Science and Electronic Engineering Conference (CEEC)*, pages 243–248, 2015.

[117] David E. Rumelhart, Geoffrey E. Hinton, and Ronald J. Williams. Learning representations by back-propagating errors. *Nature*, 323(6088):533–536, October 1986.

[118] Sandro Skansi. *Introduction to Deep Learning*. 2018.

[119] Junyoung Chung, Çaglar Gülçehre, KyungHyun Cho, and Yoshua Bengio. Empirical evaluation of gated recurrent neural networks on sequence modeling. *CoRR*, abs/1412.3555, 2014.

[120] Sepp Hochreiter and Jürgen Schmidhuber. Long Short-Term Memory. *Neural Computation*, 9(8):1735–1780, nov 1997.

[121] Klaus Greff, Rupesh K. Srivastava, Jan Koutnik, Bas R. Steunebrink, and Jurgen Schmidhuber. LSTM: A Search Space Odyssey. *IEEE Transactions on Neural Networks and Learning Systems*, 28(10):2222–2232, oct 2017.

[122] Phillip Kollmeyer. Panasonic 18650pf li-ion battery data. *Mendeley Data*, 2018.

[123] Jinhao Meng, Guangzhao Luo, and Fei Gao. Lithium polymer battery state-of-charge estimation based on adaptive unscented kalman filter and support vector machine. *IEEE Transactions on Power Electronics*, 31(3):2226–2238, 2016.

[124] Wenxian Duan, Chuanxue Song, Silun Peng, Feng Xiao, Yulong Shao, and Shixin Song. An improved gated recurrent unit network model for state-of-charge estimation of lithium-ion battery. *Energies*, 13(23), 2020.

[125] Qiao Zhu, Mengen Xu, Weiqun Liu, and Mengqian Zheng. A state of charge estimation method for lithium-ion batteries based on fractional order adaptive extended kalman filter. *Energy*, 187:115880, 2019.

[126] G. Plett. Efficient battery pack state estimation using bar-delta filtering. 2009.

[127] Kodjo Senou Rodolphe Mawonou, Akram Eddahech, Didier Dumur, Emmanuel Godoy, Dominique Beauvois, and Michel Mensler. Li-ion battery pack soc estimation for electric vehicles. In *IECON 2018 - 44th Annual Conference of the IEEE Industrial Electronics Society*, pages 4968–4973, 2018.

[128] Rui Xiong, Fengchun Sun, Xianzhi Gong, and Hongwen He. Adaptive state of charge estimator for lithium-ion cells series battery pack in electric vehicles. *Journal of Power Sources*, 242:699–713, nov 2013.

[129] Rui Xiong, Hongwen He, Fengchun Sun, and Kai Zhao. Online estimation of peak power capability of Li-Ion batteries in electric vehicles by a hardware-in-loop approach. *Energies*, 5(5):1455–1469, 2012.

[130] Long Xu, Junping Wang, and Quanshi Chen. Kalman filtering state of charge estimation for battery management system based on a stochastic fuzzy neural network battery model. *Energy Conversion and Management*, 53(1):33–39, jan 2012.

[131] IPG Automotive Group. User's Guide Version 9.0 CarMaker. 2020.

[132] Vincent R. Tannahill, Kashem M. Muttaqi, and Danny Sutanto. Driver alerting system using range estimation of electric vehicles in real time under dynamically varying environmental conditions. *IET Electrical Systems in Transportation*, 6(2):107–116, 2016.

[133] pycarmaker. https://github.com/gmnvh/pycarmaker#readme.